Title	MAGNETOACOUSTIC RESONANCE STUDY OF ACCEPTOR GROUND-STATE IN GERMANIUM
Author(s)	Tokumoto, Hiroshi
Citation	大阪大学, 1977, 博士論文
Version Type	VoR
URL	https://hdl.handle.net/11094/27714
rights	
Note	

MAGNETOACOUSTIC RESONANCE STUDY OF ACCEPTOR GROUND-STATE
IN
GERMANIUM

by

Hiroshi TOKUMOTO

Submitted in Partial Fulfillment of the Requirements for
the Degree of Doctor of Philosophy
at the
OSAKA UNIVERSITY

Signature of Author ______________________________

Electrotechnical Laboratory, Agency of Industrial Science
and Technology, November, 1976.

Certified by ______________________________

Thesis Supervisor

Accepted by ______________________________

Chairman, Committee of Graduate School of Science

MAGNETOACOUSTIC RESONANCE STUDY OF ACCEPTOR GROUND-STATE

IN

GERMANIUM

by

Hiroshi TOKUMOTO

ABSTRACT

The acceptor ground-state in germanium was studied by means of the ultrasonic attenuation measurement. The attenuation was measured in Ga-doped Ge with concentrations ranging from 3.5×10^{15} to 2.5×10^{16} cm^{-3} and with dislocation densities of the order of 10^{3} cm^{-2}.

The temperature dependence of the attenuation in the absence of the magnetic field was measured in the temperature range 1.3 to 45 K at several acoustic power levels. The attenuation increases with decreasing the temperature below 15 K. This increase is ascribed to the resonance absorption of the ultrasonic waves caused by the hole transitions between the split levels due to the internal stresses. The attenuation at low temperatures decreases with increasing the acoustic power: the saturation effect in the ultrasonic attenuation appears.

The magnetoacoustic resonance attenuation (MARA) was observed under strong magnetic fields. The attenuation was studied in detail by varying the acoustic frequency, the temperature, the magnetic field direction, the acceptor concentration, the acoustic power, the acoustic mode, the propagation direction, and the uniaxial stress. The experimental results are explained semi-quantitatively in terms of the acceptor-hole-lattice interaction in the effective mass approximation by taking account of the presence of the distributed local splittings and the quadratic Zeeman effect in addition to the linear Zeeman effect. Consequently, the Zeeman-splitting parameters of the ground state in Ga-doped Ge are obtained. The g-values are $g_{1/2}' = -0.14 \pm 0.07$ and $g_{3/2}' = 0.02 \pm 0.03$ for $\vec{H}$ // [001]. The discrepancy between the present results and the results derived from the magnetooptical absorption by Soepangkat and Fisher is resolved by proposing a new assignment of their magnetooptical spectra. The coefficients of the quadratic Zeeman effect are $q_2 = (0.5 \pm 0.2) \times 10^{-4}$ $\mathrm{K/kG^2}$ and $q_3 = -(0.6 \pm 0.2) \times 10^{-5}$ $\mathrm{K/kG^2}$. The present g-values, which are very small compared with the effective mass calculations, seem to be

consistent with the measured magnetothermal conductivity and the present status of the ESR study. From the line shape of the MARA, we evaluated the initial splittings of the acceptor ground-state. When we assume that their distribution is represented by the Gaussian form, the average splitting Δ_0 and the variance σ are obtained as -0.02 ± 0.006 K and $0.03 - 0.05$ K, respectively.

ZUSAMMENFASSUNG

Es wurde der Akzeptorgrundzustand im Germanium mit die Ultraschalldämpfung untersucht. Die Dämpfung wurde in Ga-gedopt Ge mit Konzentrationen zwischen $3{,}5 \times 10^{15}$ und $2{,}5 \times 10^{16}$ cm^{-3} und mit Dislokationdensitäten ($\sim 10^{3}$ cm^{-2}) gemessen.

Ohne magnetisches Feld wurde die Temperaturabhängigkeit der Schalldämpfung für Temperaturen zwischen 1,3 und 45 unter einigen Akustikintensitäten gemessen. Unterhalb 15 K wächst die Dämpfung mit abnehmender Temperatur an. Diese Anwächse werden der Resonanzwechselwirkung des Schalls von den inneren Drücken verursachten Aufspaltungen des Akzeptorgrundzustandes zugeschrieben. Außerdem wurde die Intensitätsabhängigkeit der Schalldämpfung beobachtet.

Die magnetoakustische Resonanzdämpfung (MARD) wurde in starkem Magnetfeld beobachtet. MARD wurde genau gemessen, dabei wurde die akustische Frequenz, die Temperatur, die Richtung des Magnetfeldes, die Akzeptorkonzentration, die Akustikintensität, die Akustikmode, die Richtung der Verbreitung und das uniaxiale Druck verwandelt. Die experimentellen Ergebnisse werden halbqualitativ durch die Akzeptor-Löcher-Gitter-Wechselwirkung erklärt, die unter einer Effektivmasseannäherung mit Rücksicht auf verteilte Aufspaltungen und den quadratischen Zeeman-Effekt sowie auf den linearen Zeeman-Effekt berechnet wird. Daraus werden die Parameter für den Zeeman-Spalten des Akzeptorgrundzustandes in Ga-gedopt Ge bekommen. Die g-Werte sind $g_{1/2}' = -0{,}14 \pm 0{,}07$ und $g_{3/2}' = 0{,}02 \pm 0{,}03$ für $\vec{H}$ // [001]. Die Unterschiede zwischen diesen g-Werten und denen von Soepangkat und Fisher werden durch neuen Vorschlag der Zuteilung für ihr Magnetooptik-Spektrum gelöst. Die Koeffizienten für den quadratischen Zeeman-Effekt sind $q_2 = (0.5 \pm 0.2) \times 10^{-4}$ K/kG^{2} und $q_3 = -(0.6 \pm 0.2) \times 10^{-5}$ K/kG^{2}. Die obengenannten g-Werte, die sehr kleiner als die von Effektivmasseberechnungen sind, können sich mit der beobachteten Magnetothermal-Leitfähigkeit und dem heutigen Zustand der ESR-Untersuchung

vertragen. Mit dem Liniegestalt von MARD schätzt man die anfängliche Aufspaltung des Akzeptorgrundzustandes. Die durchschnittliche Aufspaltung Δ_0 und die Abweichung σ betragen -0,02 ± 0,006 K und 0,03 - 0,05 K, wenn man die Aufspaltungsverteilung als eine Gaußische voraussetzt.

CONTENTS

I. INTRODUCTION

The electronic states of shallow impurities in semiconductors are represented by the hydrogenic states. When the average distance among the impurity atoms is larger than their effective Bohr radius, we can neglect the interaction among them in the first-order approximation. The localized shallow impurities interact with acoustic phonons strongly. This has been seen as a remarkable increase at low temperatures in either the thermal resistance[1-10] or the ultrasonic attenuation.[11-19]

The thermal resistance and the ultrasonic attenuation in lightly doped *n*-type Ge and *n*-type Si at low temperatures have been understood rather well: They are explained by the interaction of the acoustic phonons with the localized donors whose electronic states are represented by the effective mass approximation.[1-4,11-16] However, the problem on the interaction with the localized acceptors has remain unsettled.

The strong increase of the ultrasonic attenuation in *p*-Si as decreasing the temperature below 20 K was first ascribed to the effect of free holes.[17] Pomerantz,[18] however, pointed out that the holes are frozen into the acceptor ground-state in adopted experimental conditions. Suzuki and Mikoshiba (SM)[19] proposed a model to explain the ultrasonic attenuation in lightly doped *p*-Si at low temperatures: (a) They calculated the coupling of the ultrasonic waves with the acceptors in the regime of the effective mass approximation.[20,21] (b) They assumed the presence of the randomly distributed internal stresses, which split the fourfold-degenerate acceptor-ground-state into two Kramer's doublets.[22] The observed ultrasonic attenuation in lightly doped *p*-Si at low temperatures as functions of the temperature,[17,23,24] the uniaxial stress,[25] the magnetic field,[24,26] the dislocation density,[24] and the acceptor concentration[24] are consistent with the SM-model. This model is also consistent with the thermal conductivity[27] and the heat-pulse propagation[28] in *p*-Si. In *p*-Ge, this model is useful to explain the temperature dependence of the thermal conductivity[27] and the heat-pulse propagation.[28] Cahllis and Halbo,[29] however, have reported that this model is inadequate for the analysis of the magnetic field dependence of the thermal conductivity in *p*-Ge. They proposed that the existence of the low-lying states due to the dynamic Jahn-Teller effect[30] should be taken into account.

In order to clarify the anomalous magnetothermal conductivity in *p*-Ge,[29,31] we measured the magnetic field dependence of the ultrasonic attenuation in Ga-doped Ge. Then, we found a resonance attenuation under strong magnetic field,[32] which was observed in neither B-doped Si nor Zn-doped GaP.[33] The resonance attenuation seemed to be explained by an extension of the SM-model; we had taken the quadratic Zeeman effect of the acceptor ground-state into account[32,33] in addition to the linear Zeeman effect whose parameters are reported by Soepangkat and Fisher (SF).[34]

We have extended the experiments of the magnetoacoustic resonance attenuation (MARA) by varying the acoustic frequency, the temperature, the magnetic field direction, the acceptor concentration, the acoustic power, and the acoustic mode, and also by applying the uniaxial stress. It turned out, then, that the Zeeman-splitting parameters adopted previously[32,33] were not adequate to explain all of the observed results consistently. We found that the *g*-values of the acceptor ground-state, which are derived by SF,[34] could not be consistent with our experimental results at all. In this article, we propose new *g*-values which are useful to explain our observations and also are consistent with the experimental results by SF:[34] An alternative assignment of the observed magnetooptical spectra is consistent with the new *g*-values.

The purpose of this article is to show the detailed description on the MARA as functions of the temperature and so on, and to present a successful interpretation of them. We will show that the experimental results are explained by the extension of the SM-model by taking account of the quadratic Zeeman effect. From the comparison of the resonance fields with the calculated energy-level shifts of the acceptor-ground-state quartet, we have determined the Zeeman-splitting parameters. The consistency of these values with other experimental results, the magnetooptical spectra[34] and the magnetothermal conductivity,[29,31] are discussed.

The techniques for the attenuation measurement are described in Sec. II. The sample characteristics and the experimental procedure are also discussed in this section. In Sec. III, a theoretical description for the interaction of the ultrasonic waves with the acceptor holes at low temperatures are presented. Section IV contains the experimental results of the MARA under various experimental conditions. Analyses of these results with the theoretical predictions are presented in Sec. V. In this section, various aspects of the experimental results and the theoretical interpretation are also discussed. In Sec. VI, we discuss the results of the present investigation and the consistency with the other experimental results. Summary and concluding remarks of the present study are given in Sec. VII.

II. EXPERIMENTAL TECHNIQUE AND PROCEDURE

A. Ultrasonic equipments and attenuation measurement

The ultrasonic attenuation was measured by standard pulse-echo technique. In the present experiment, the amplitude of an ultrasonic echo was measured as a function of magnetic field or temperature under a fixed acoustic frequency and a fixed acoustic power level.

Electrical rf pulses with frequencies below 800 MHz were generated and received by Matec Model 6000 rf Ultrasonic Generator and Receiver with either Plug-in Model 960 (10 to 310 MHz) or Plug-in Model 970 (300 to 800 MHz). The rf pulses tuned to the desired frequency were introduced to an ultrasonic transducer through a matching network (Nihon Koshuha, Stub Tuner) and converted to ultrasonic pulses. Then, a series of the ultrasonic echos was set up within a sample. These in turn generated small electrical signals in the transducer, which were coupled to a high gain receiver. The video envelopes of the amplified signals were displayed on an oscilloscope (Sony Tektronix 465), which was triggered by the pulses from the pulse generator. The video signals was still amplified by a Box Car Integrator (PAR Model 160). Since the gate of the Integrator was synchronized with the rf pulse generator, we could select one of the ultrasonic echos. The dc signals from the Integrator were led to a Logarithmic Converter (HP 7560 AM) and then were recorded with an X-Y recorder (YEW Type 3072) as a function of either the magnetic field or the temperature. The magnetic field was monitored with the calibrated magnetoresistance of the copper wire connected to a digital voltmeter (YEW Type 2501). The block diagram of this system is shown in Fig. 2-1.

The block diagram for the ultrasonic measurement with frequencies between 1 and 2 GHz is shown in Fig. 2-2. An rf oscillator (Nihon Koshuha) of 1 to 2 GHz was triggered by the pulses from a pulse generator (HP Model 214A) and generated the electrical rf pulses. The pulses were passed through a circulator

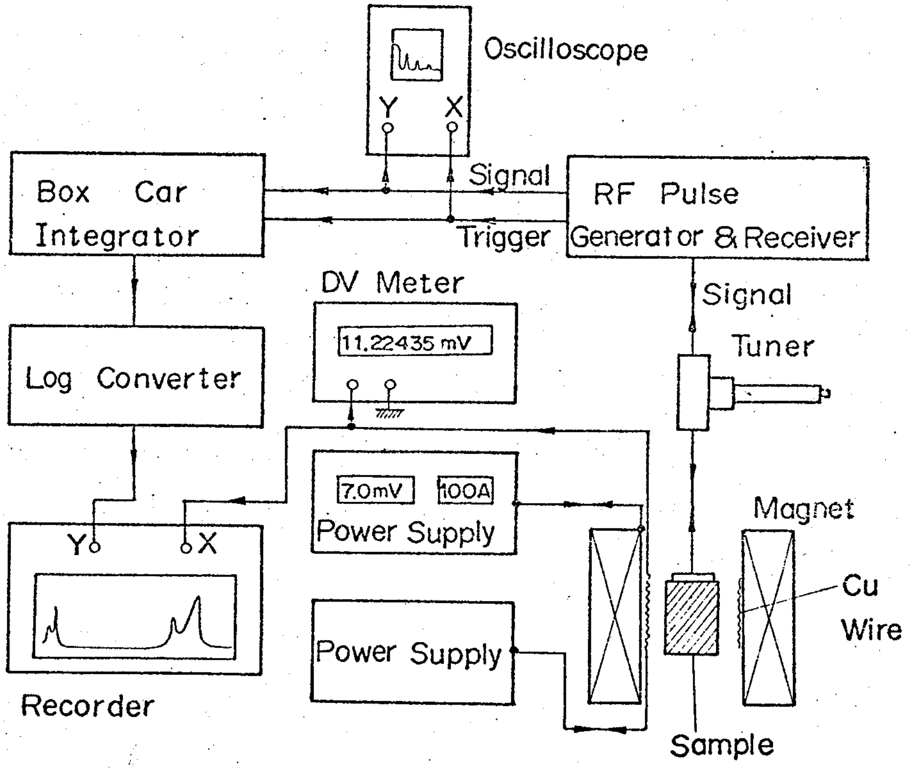

FIG. 2-1. Block diagram of the ultrasonic measurement in the frequency range 10 to 800 MHz.

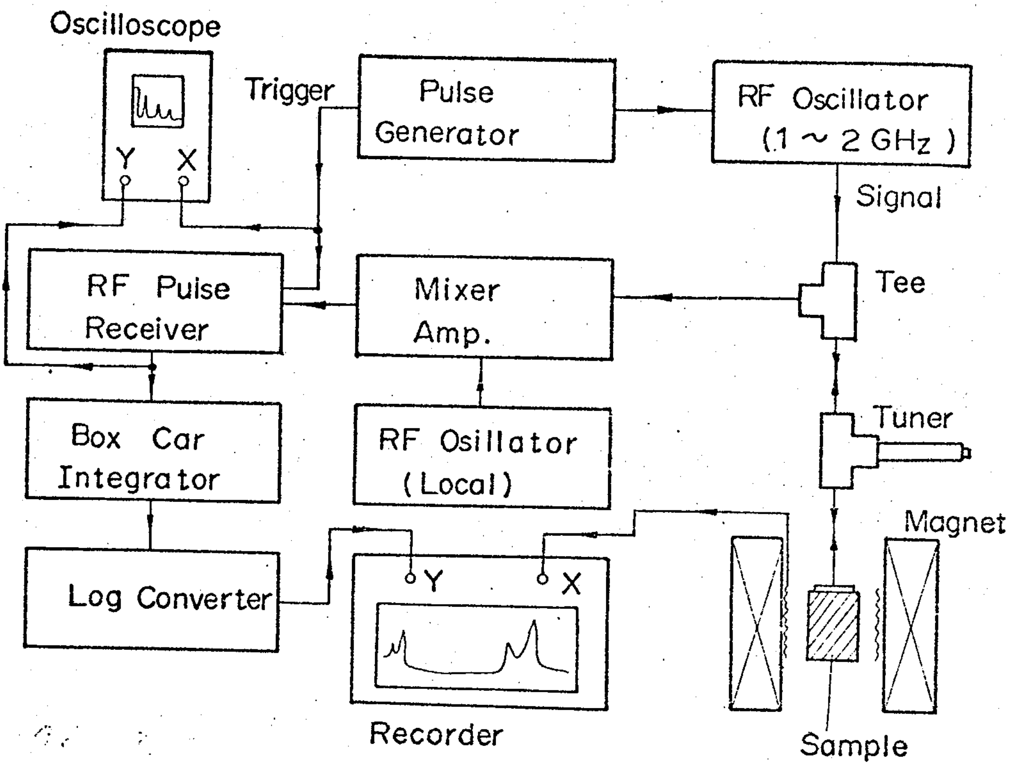

FIG. 2-2. Block diagram of the ultrasonic measurement in the frequency range 1 to 2 GHz. The magnetic field system is the same in Fig. 2-1.

(Western Microwave, Model 3A-1020) and were introduced to the sample through the matching network. After the reflected signals from the sample were passed through the circulator, they were mixed with reference signals from an rf oscillator (HP 8614A) and amplified by a mixed amplifier (Shimada Rika Kogyo). The signals were amplified by Matec Model 6000 rf Receiver with Plug-in Model 960. The video envelopes of the amplified signals were treated as before and recorded on the chart.

In the present experiment, pulse repition-rate of 50 - 100 Hz and pulse duration of 0.5 - 1.0 μsec were used. The overall nonlinearity of the apparatus was less than 5 %.

B. Ultrasonic transducer

We used a ZnO-piezoelectric film transducer[35] in order to avoid giving stresses to the sample. This transducer was not affected by the magnetic field up to 120 kG.

We fabricated the ZnO-piezoelectric film transducer on one of the parallel faces by an rf sputtering technique as follows. Aluminum film with thickness of 500 - 1000 Å was evaporated onto one face of the polished surfaces under pressure of 10^{-6} Torr. Prior to the evaporation, the surface was moderately baked at the temperature of 70 - 100 C in order to degas from the surface. Gold wires with diameter of 50 μm were ultrasonically bonded at a corner of the aluminum film. The film and the wires act as a ground electrode and leads of the ZnO film, respectively. The sample with the film was set on a sample holder of the sputtering apparatus so that ZnO was sputtered on the aluminum film. We set the sample surface parallel to a face of a ZnO target to prepare the transducer for the longitudinal waves as shown in Fig. 2-3(a). To prepare the transducer for the transverse waves, the sample was set inclined against the ZnO-target face by an angle of about 30° as shown in Fig. 2-3(b). The sputtering was carried out by rf field of

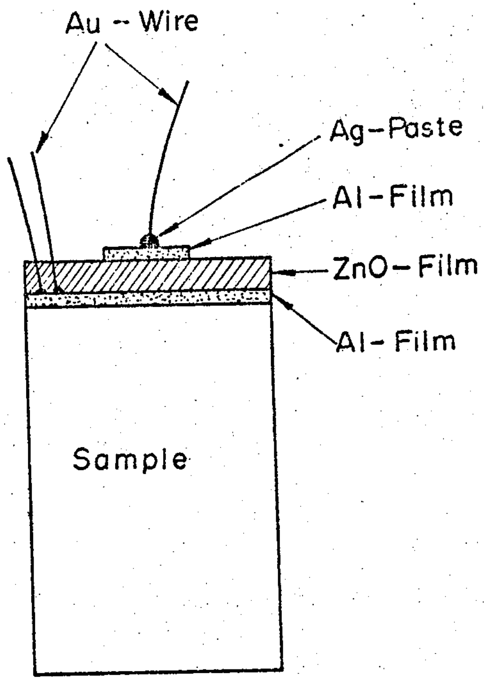

FIG. 2-4. Schematic structure of the ZnO-piezoelectric film transducer.

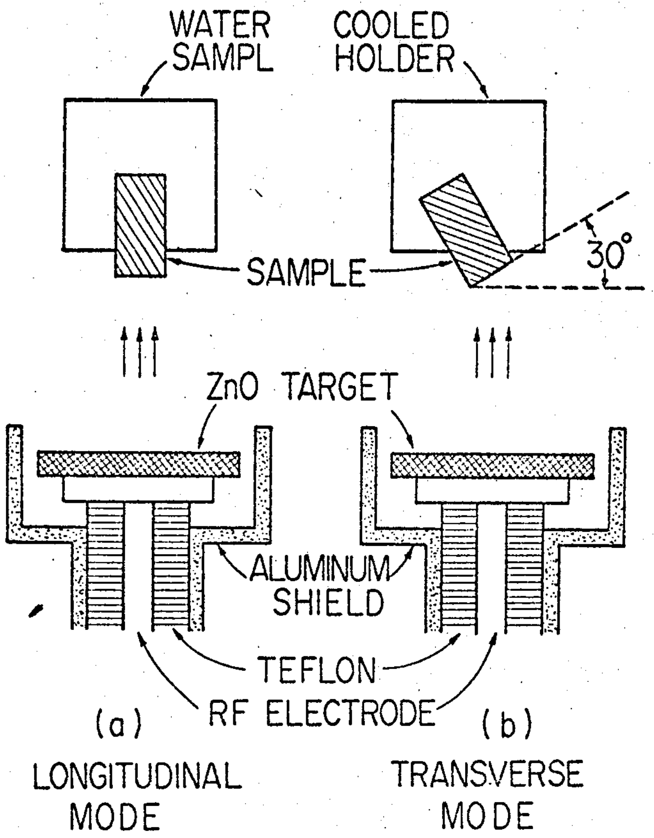

FIG. 2-3. Schematic representation of the sample setting in the sputtering apparatus.

13.6 MHz in the atomosphere of argon gas with pressure of about 10^{-2} Torr. The sputtering rate was about 30 Å/min and the film thickness was 3000 - 5000 Å. The sample was cooled during the sputtering by passing water through the sample holder. After the sputtering, another aluminum film was evaporated on the center of the ZnO film in the shape of a circular plate with diameter of about 4 mm. Finally, gold wire (50 μmϕ) was cemented by a conducting silver paste (EPO-TEK 417) on the aluminum film with area of 150 - 200 μm^2. The ZnO-piezoelectric film transducer prepared by the above procedure is shown schematically in Fig. 2-4. We could generate and detect either the longitudinal or the transverse waves in the frequency range 0.3 to 2 GHz by one transducer in the untuned condition. The conversion loss was estimated to be below 50 dB including losses due to impedance mismatch of the circuit.

C. Samples and sample preparation

Five different samples of Ga-doped Ge were used. The concentrations N were estimated by the resistivities.[36] The sample characteristics are listed in Table 2-1..

The crystals were oriented within 1° of the desired direction by X-ray method. We cut them in a shape of rectangular parallelepipeds. The end faces normal to the propagation direction of the ultrasonic waves were lapped by successive using of either carborundum or alumina powders of mesh size Nos. 1000, 1200, 2000, and 4000. Finally, we polished with 0.05 micron alumina powder. Parallelism of the faces was 10 - 20 seconds of arc. In the sample #15LC, which was used for the measurement of the uniaxial stress dependence, the end faces perpendicular to the uniaxial stress direction were also lapped and polished by the same procedure to within parallelism of 1 minute of arc. Before preparing the ZnO-piezoelectric film transducer, we washed out the samples with chemicals, e.g., the mixture of ethyl ether and methyl alcohol, aceton, etc.

Table 2-1. Characteristics of the samples.

Sample	Resistivity (ohm-cm)	EPD[a] (cm^{-2})	Ga-concentration[b] N (cm^{-3})	Propagation direction	Dimensions[c] (cm^{-3})	R[d] (Å)
#15LA	1.1-1.2	∿700	$(3.5\pm0.7)\times10^{15}$	[001]	1.02×0.61×0.59	408
#15LB	1.1-1.2	∿700	$(3.5\pm0.7)\times10^{15}$	[110]	0.71×0.59×0.63	408
#15LC	1.1-1.2	∿700	$(3.5\pm0.7)\times10^{15}$	[110]	0.62×0.63×1.67[e]	408
#15H	0.50-0.55	∿900	$(7.0\pm0.6)\times10^{15}$	[001]	1.04×0.55×0.61	324
#16L	0.19-0.20	∿400	$(2.5\pm0.5)\times10^{16}$	[001]	1.08×0.61×0.62	212

[a] EPD denotes the etch pit density.

[b] N is estimated from the resistivity after Ref. 36.

[c] The dimension in the propagation direction is given first.

[d] $R = (3/4\pi N)^{1/3}$ denotes the average distance among gallium acceptors.

[e] The dimension in the uniaxial stress direction ([001]) is given third.

The average distances $R = (3/4\pi N)^{1/3}$ are 408, 324, and 212 Å in #15L, #15H, and #16L, respectively. The effective Bohr radius a^*, which indicates an extent of the acceptor-ground-state wave-function, is estimated to be 37.8 Å in the effective mass theory.[21] Since $R \geq 6a^*$ is satisfied in our samples, we may regard the acceptors isolated in the first-order approximation.

The samples were set to the sample holder of the cryostat with great care in order to avoid giving stresses except for the case measuring the stress dependence.

D. Magnetic field apparatus[37]

Static magnetic fields up to 120 kG were supplied by using a Nb_3Sn superconducting magnet (IGC) and a dc current power supply (IGC Model 150S). Figure 2-5 shows the schematic diagram of the superconducting magnet (H) mounted in liquid helium and nitrogen dewars (E) which were made of stainless-steel (S.S.) (Janis Research Co. Inc., innermost diameter of 8 inch, length of 44 inch). On a dewar cap (B), we attached the following materials; two terminals for current supply to the magnet, two guide-tubes for liquid helium transfer and for return of vaporized helium gas, a guide-tube for the insertion of the liquid-helium level-indicater, several terminals for monitoring magnetic field and coil voltage, etc. Three S.S. tubes (C) (10 mm o.d., 9.4 mm i.d.) were attached to the lower face of the cap (B) for supporting the magnet. Four aluminum shield plates (S1)-(S4) were fixed to the tubes (C) in order to reduce the vaporization of liquid helium by thermal radiation. Cables (J) for introduction of the magnet current to the magnet consisted of three parts: 1200 wires (0.1 mm-diameter polyester-coated copper wire) from (B) to (S1), 600 wires from (S1) to the sipport ring (N), 350 wires from (N) to the terminal of the magnet. These cables were passed through the guide-tubes for return of the vaporized helium gas and hence were cooled by the helium gas.

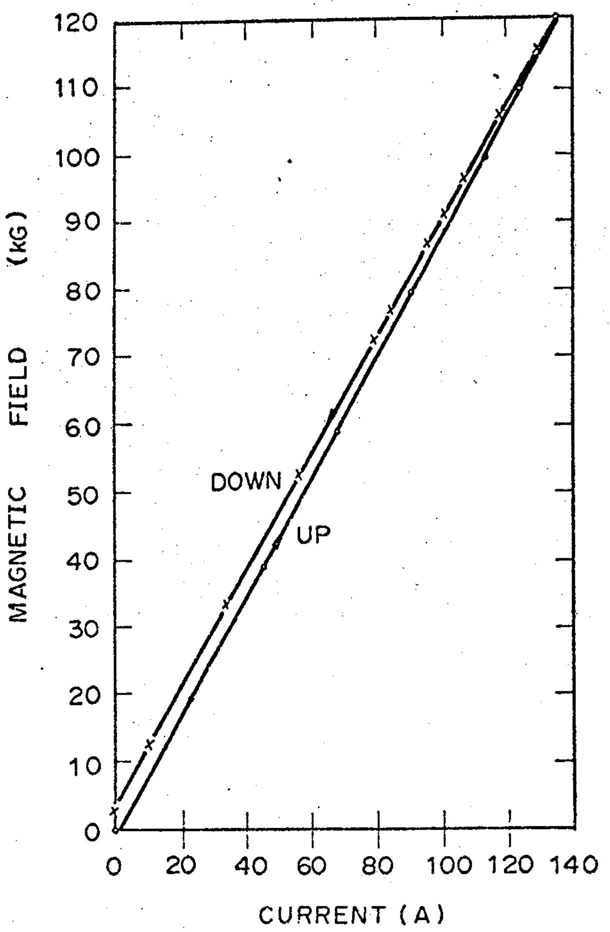

FIG. 2-6. Magnetic field as a function of the magnet current.

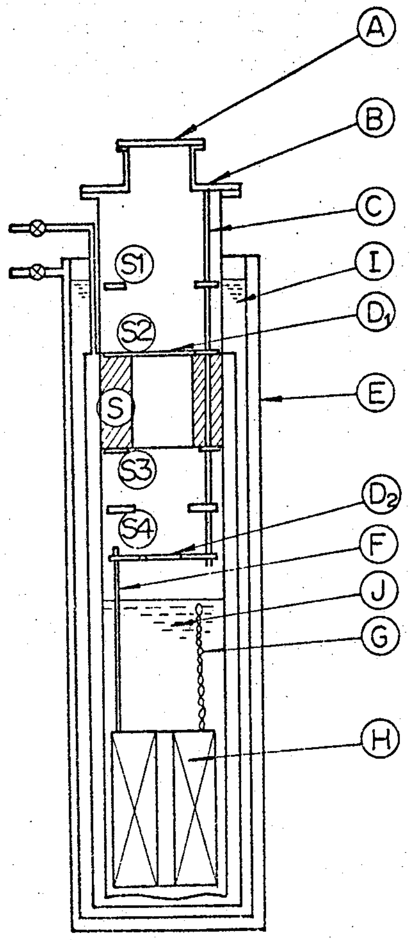

FIG. 2-5. Schematic representation of the superconducting magnet system.

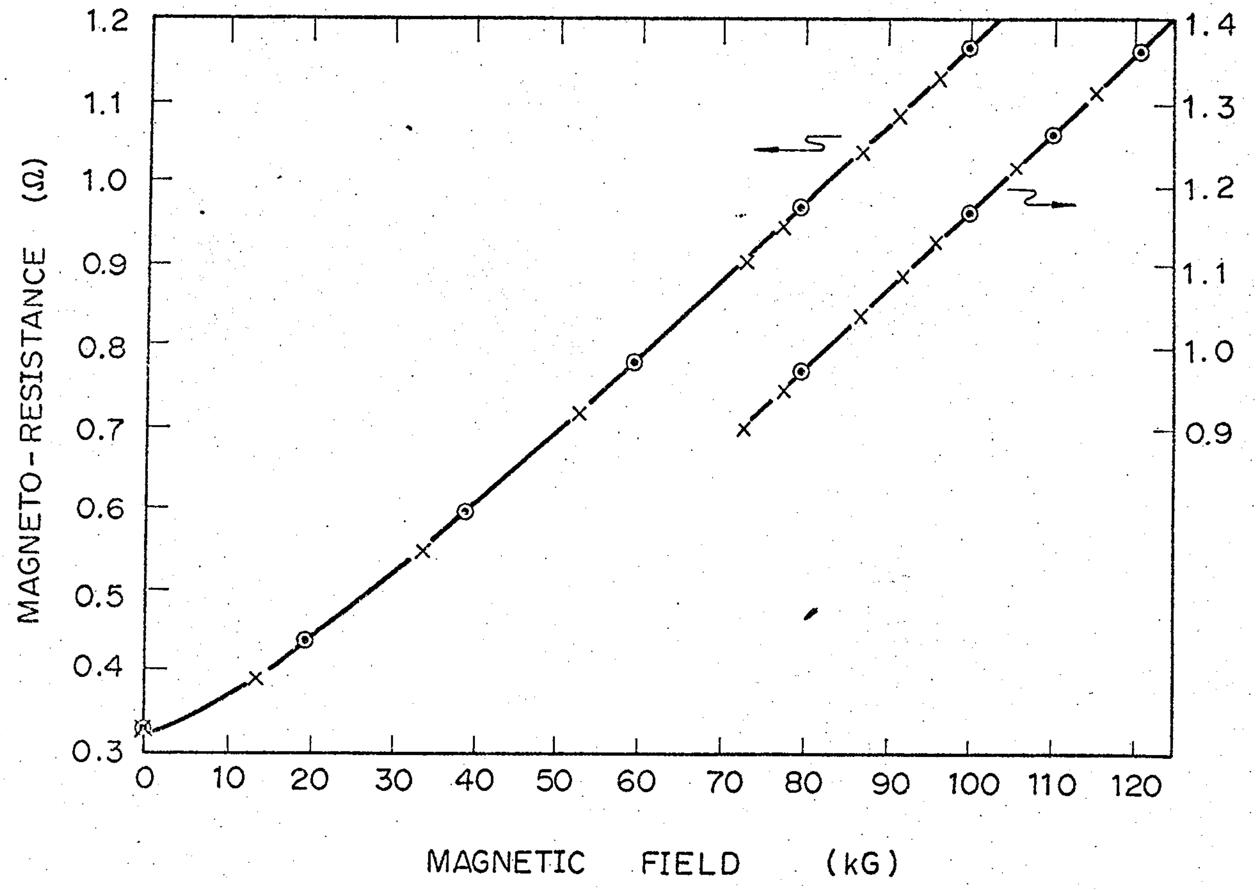

FIG. 2-7. Resistance of the copper wire as a function of the magnetic field.

The hysterisis was observed in the relation between the magnet current and the magnetic field strength as shown in Fig. 2-6. On the other hand, the hysterisis did not exist in the magnetoresistance of the copper wire which was wound in the magnet as shown in Fig. 2-7. Therefore, we monitored the field strength by the latter device. The magnetic field strength in these figures was measured by integrating the induced voltage on a search coil during 180°-rotation.[37]

E. Cryogenic equipments

Although the superconducting magnet itself was fully submerged in 4.2 K liquid helium, the temperature of the sample was changed in the range 1.3 to 4.2 K during the experiment in the magnetic field. Figure 2-8 shows one of the cryostats, which was designed and assembled by K. Kajimura. This cryostat consisted of two S.S. tubes (outer tube (F) was 32 mm o.d. and 31 mm i.d., inner tube (D) 26 mm o.d. and 25 mm i.d.). A valve (A) and a S.S. tube (E) (7 mm o.d., 6.4 mm i.d.) were used to evacuate a vacuum jaket up to 10^{-6} Torr. (G) was a teflon spacer in order to avoid contact of the two tubes (D) and (F). Liquid helium was transfered into a sample room by turning a fine-threaded S.S. screw-tip (C) through a handle (B). The precise description of this system has been given by White.[38]

Temperatures above 4.2 K were controlled by joule heat of a Cu-Ni wire-heater (Cu 30 %, 0.2 mm diameter, 19 ohm/cm at room temperature) which was wound on a sample holder. The temperature was monitored by a calibrated germanium thermometer (CryoCal Inc., CryoResistor). Temperatures below 4.2 K were obtained by forced vaporization of the liquid helium in the sample room by using an oil-sealed rotary pump whose pumping rate was 900 liter/min. The temperature was measured by the observation of the helium gas pressure near the sample using either a calibrated absolute pressure gauge (Naganokeiki) or a McLeod gauge (Shimazu).

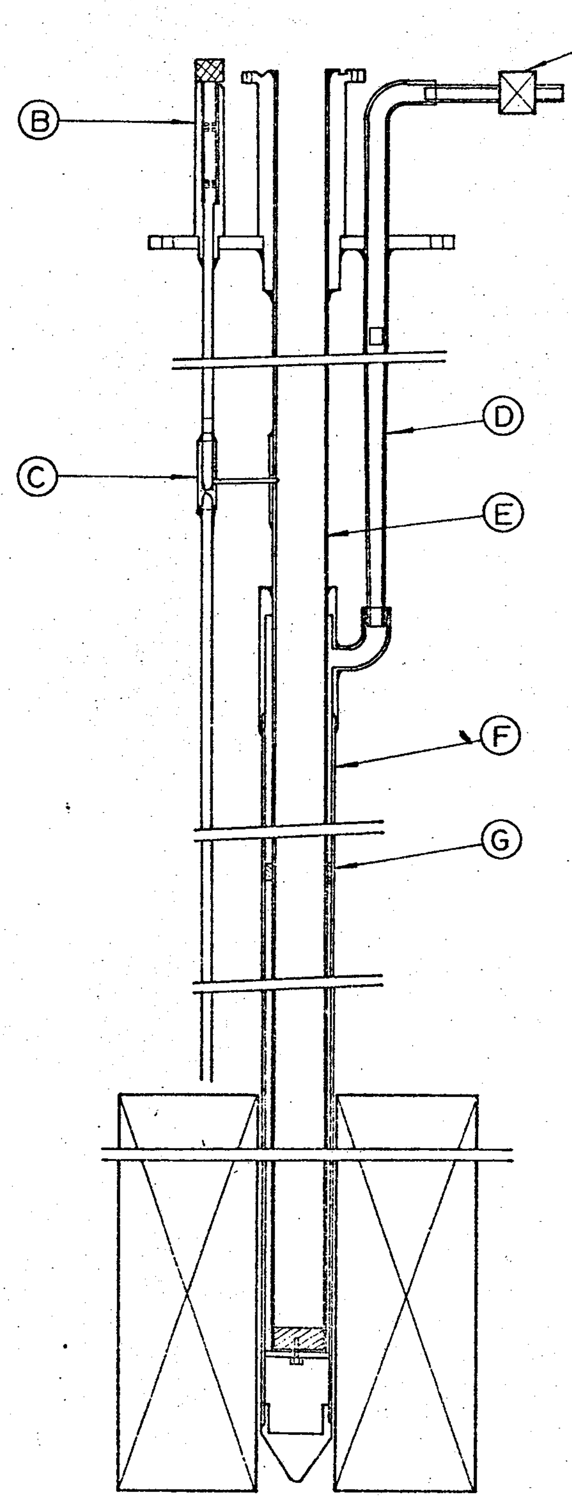

FIG. 2-8. Schematic representation of one of the cryostats used in the measurement of the temperature dependence of the ultrasonic attenuation.

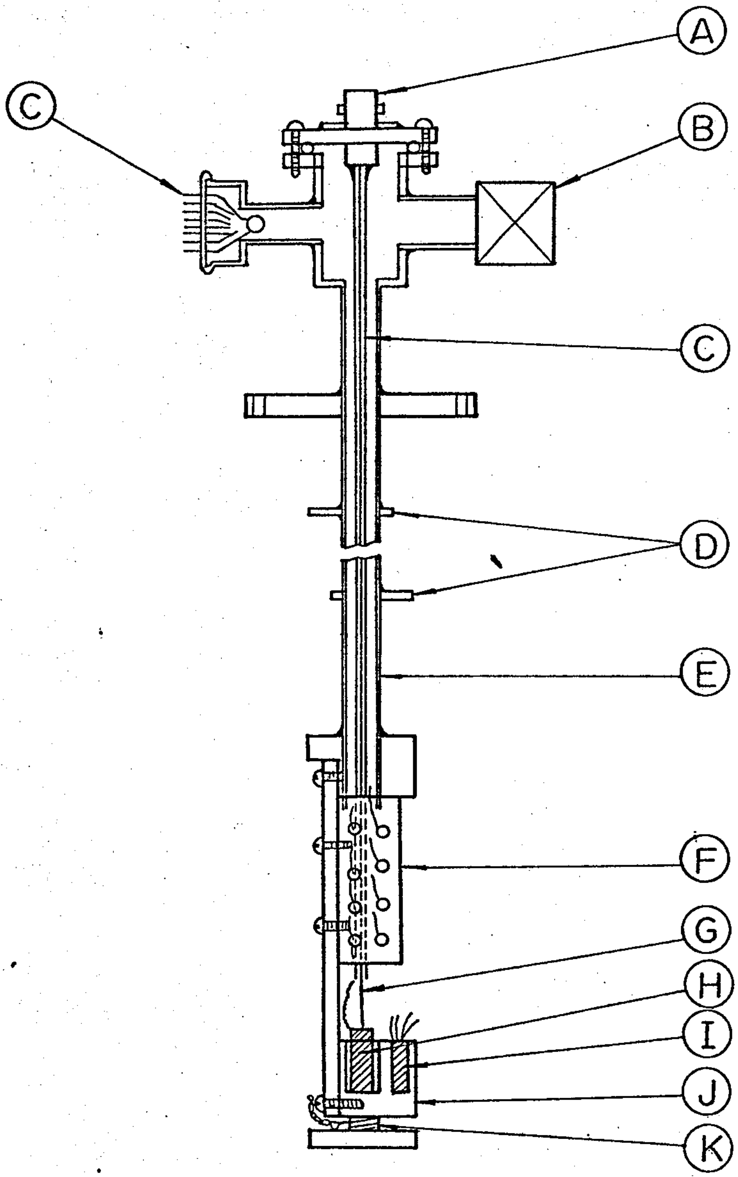

FIG. 2-9. Schematic representation of one of the cryostats used in the ultrasonic measurement. This was set in the cryostat of Fig. 2-8.

One of the cryostats for the ultrasonic measurement is shown in Fig. 2-9. The electrical rf pulses were guided from a BNC connector (A) to the sample (H) through a coaxial cable (C). The cable (C) consisted of a 0.5 mm-diameter S.S. wire, a teflon tube (3 mm o.d., 0.5 mm i.d.), and a S.S. tube (4 mm o.d., 3 mm i.d.). Two 50 µmϕ gold wires (G) connected the coaxial cable end to the electrode leads of the transducer. A 1/2 inch brass-valve (B) was used to measure the helium gas pressure through a S.S. support (E) (7 mm o.d., 6.4 mm i.d.). Two polished copper radiation shields (D) were attached to (E). Terminals (C) were connected to the terminals on the plate (F) by the enamel-coated 0.16 mm-diameter copper wires. The copper wires were used as the lead wires to monitor the temperature and to supply the current to the heater (K).

The sample (H) was fully submerged in the liquid helium during the experiment at temperatures below 4.2 K. It should be noted that the transmission of the ultrasonic waves to the liquid helium can be neglected: The ratio of the acoustic impedance of the liquid helium ($\sim 3 \times 10^3$ g/cm^3·sec) to the germanium crystal ($\sim 3 \times 10^6$ g/cm^3·sec) is estimated to be 10^{-3}. The transmission of the ultrasonic waves to the liquid helium is less than 0.1 %.

F. Uniaxial stress apparatus

The apparatus for applying uniaxial compressional stress at low temperatures was designed to minimize non-uniformity of the stress in the sample. Figure 2-10 shows the stress apparatus schematically.

The stress frame (N)-(T) was fully submerged in the liquid helium during the experiment, and was firmly fixed to the end of a outer S.S. tube (L) (32 mm o.d., 31 mm i.d.). The stress frame consisted of two parallel 98 mm-long brass rods (P) (4 mm diameter) and two brass rods (Q) (32 mm long, 10 mm diameter) and (R) (35 mm long, 10 mm diameter). Top ends of (P) were screwed to a sliding brass bar (N) (28 mm long, 10 mm wide, 8 mm thick) and bottom ends were also screwed to a brass base-plate (T) (same size of (N)).

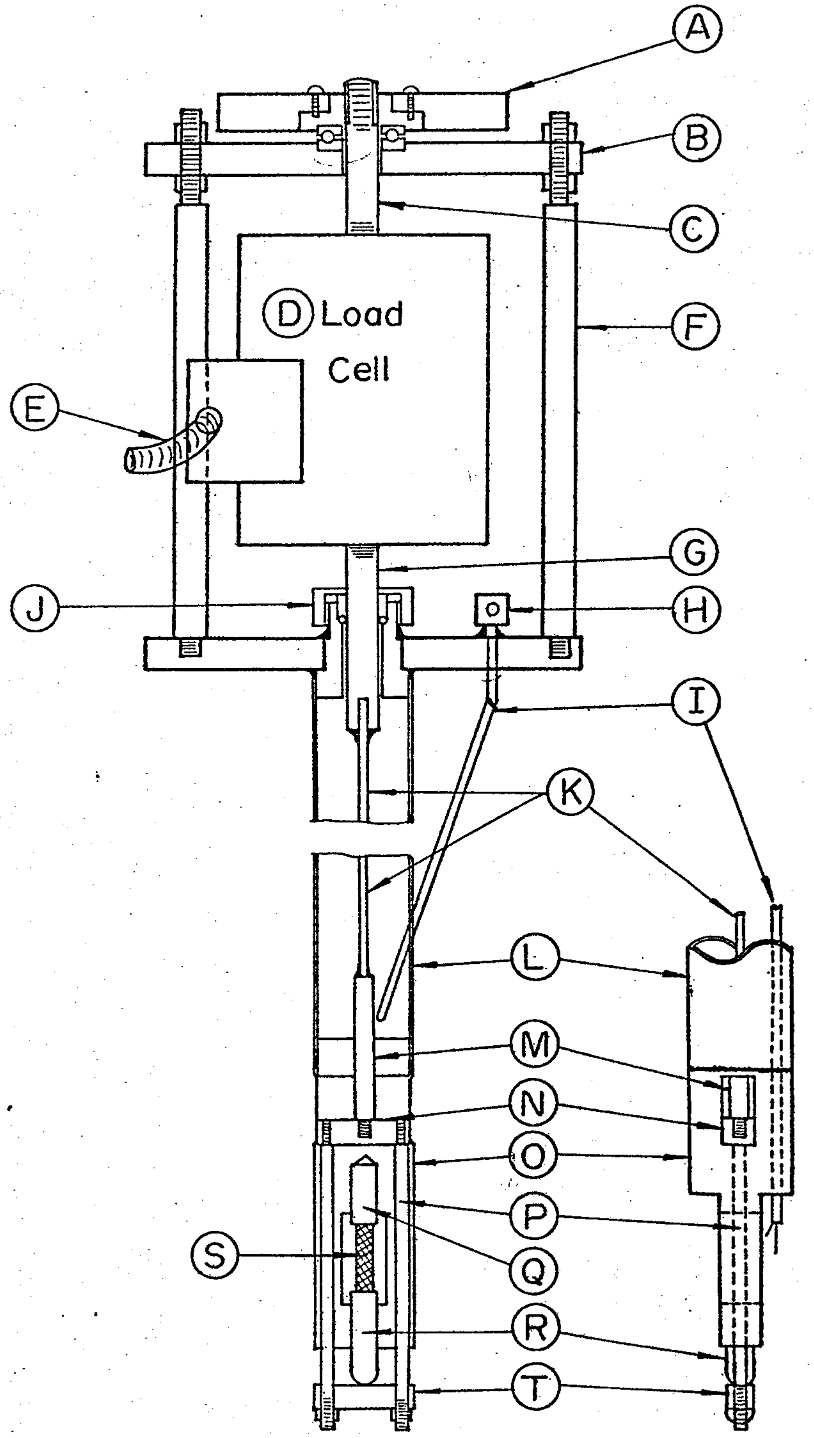

FIG. 2-10. Schematic representation of the uniaxial stress apparatus.

An end of each brass rods (Q) and (R) were flat and perpendicular to the axis of the rods. A top rod (Q) was firmly fixed to a brass holder (O) (32 mm outermost diameter) and a sliding brass rod (R) was placed on the base plate (T). The stress frame was prepared with great care in order to avoid introducing any frictions during the application of the stress.

The strain-generation frame (A)-(G) was usually at room temperature and was firmly fixed to the top end of the tube (L). This frame consisted of two parts: One took part in generation of the strain and another in monitoring its deformation when the stress was applied. Strain was generated by turning a rotatable aluminum disk (A) (100 mm diameter, 10 mm thick) against a 60 mm-long brass rod (C) (10 mm diameter). The central section of (A) was constructed from a fine-threaded brass screw (0.75 mm pitch) and the top part of the rod (C) was also a fine-threaded screw. Four parallel 204 mm-long aluminum rods (E) (12 mm diameter) were fixed by a stationary crosshead (B) and the dewar cap. A ball-bearing was attached between (A) and (B) in order to rotate (A) freely. The bottom end of (C) was fixed to the top of Load Cell (TMI/BLH Inc., Type 50L T3P1). The bottom of Load Cell was attached to the end of the 85 mm-long brass rod (G) (10 mm diameter). The magneitude of the strain was monitored by connecting the out put of Load Cell (E) to a calibrated Wheatstone bridge.

Translational motion of the rod (G) was transfered to the sliding bar (N) through a S.S. tube (K) (3 mm o.d., 2.4 mm i.d.) and a 55 mm-long brass rod (M) (6 mm diameter). In order to get rid of the leakage of the helium gas, a Wilson-type seal (J) was used. Since this seal caused the friction for the motion of (G), we released this seal during the experiment.

The electrical rf pulses were guided to the sample (S) through a BNC connector (H) and a coaxial cable (I), which was the same as described in Sec. II-E.

III. THEORY

A. Acceptor ground-state

When an impurity from Group-III of the periodic table replaces an atom in the crystal lattice of germanium, it produces a set of discrete states in the forbidden gap near the valence-band edge. Approximate energies and waves functions for some of these states have been calculated in the effective mass approximation.[21,22,28,39-41] The state $\Psi(\vec{r})$ of the shallow acceptor can be represented by the Bloch functions $\phi_j(\vec{r})$ of the valence-band edge and the hydrogenic envelope functions $F_j(\vec{r})$ as

$$\Psi(\vec{r}) = \sum_{j=1}^{6} F_j(\vec{r})\phi_j(\vec{r}), \qquad (3.\ 1)$$

where j denotes the six-fold degeneracy of the valence-band edge, a three-fold orbital and a two-fold spin degeneracies. This degeneracy is partly lifted by the spin-orbit interaction, which splits the valence-band edge into a quartet and a doublet corresponding to the total angular momentum $J = 3/2$ and 1/2 states, respectively.

The envelopes $F_j(\vec{r})$ are obtained by expanding in spherical harmonics $Y_{\ell m}(\theta,\phi)$.[39-41] Only even ℓ or only odd ℓ terms contribute simultaneously since the effective mass Hamiltonian is even under inversion.[22] Of importance in the present study are the acceptor-ground-state wave-functions. These are largely *s*-like, in which case the even ℓ expansion should be used. Only the $\ell = 0$ (*s*-like) and the $\ell = 2$ (*d*-like) contributions are considered here. Then, there are six independent envelopes, one *s*-like for $\ell = 0$ and $m = 0$, and five *d*-like corresponding to $\ell = 2$ and $m = 2, 1, 0, -1, -2$. Of particular interest here is the form of the wave functions of the acceptor-ground-state quartet corresponding to the magnetic quantum numbers $M_J = 3/2, 1/2, -1/2, -3/2$. These are now constructed from products of the *s*- and *d*-like envelopes and the bases $\phi_j(\vec{r})$, according to Eq.(3.1). For each M_J, these products can

Table 3-1. The functions $\Phi_i^{(M_J)}$ for an axis of quantization along [001], with corresponding radial functions and amplitude factors.†

M_J	$\frac{3}{2}$	$\frac{1}{2}$	$-\frac{1}{2}$	$-\frac{3}{2}$	Radial Parts	Amplitudes c_i
$\Phi_0^{(M_J)}$	1	0	0	0	$(\frac{1}{4\pi})^{1/2}R_0(r)$	0.860
	0	1	0	0		
	0	0	0	0		
	0	0	0	0		
	0	0	1	0		
	0	0	0	1		
$\Phi_1^{(M_J)}$	$a/2$	0	$\sqrt{3}\,b/4$	0	$(\frac{5}{4\pi})^{1/2}R_1(r)r^{-2}$	-0.198
	0	$-\sqrt{(2/3)}a$	0	0		
	$3b/4$	0	$a/2\sqrt{3}$	0		
	0	$a/2\sqrt{3}$	0	$3b/4$		
	0	0	$-\sqrt{(2/3)}a$	0		
	0	$\sqrt{3}\,b/4$	0	$a/2$		
$\Phi_2^{(M_J)}$	0	$c^*/\sqrt{2}$	$-d/\sqrt{2}$	0	$(\frac{5}{4\pi})^{1/2}R_2(r)r^{-2}$	-0.318
	$\sqrt{3}\,c/2$	0	$-c^*/2$	0		
	$\sqrt{(3/2)}d$	$-c/\sqrt{2}$	0	0		
	0	0	$c^*/\sqrt{2}$	$-\sqrt{(3/2)}d$		
	0	$c/2$	0	$\sqrt{3}\,c^*/2$		
	0	$d/\sqrt{2}$	$-c/\sqrt{2}$	0		
$\Phi_3^{(M_J)}$	$-a/2$	0	$-\sqrt{3}\,b/4$	0	$(\frac{5}{4\pi})^{1/2}R_3(r)r^{-2}$	0.187
	0	0	0	$-b/\sqrt{2}$		
	$b/4$	0	$\sqrt{3}\,a/2$	0		
	0	$\sqrt{3}\,a/2$	0	$b/4$		
	$-b/\sqrt{2}$	0	0	0		
	0	$-\sqrt{3}\,b/4$	0	$-a/2$		
$\Phi_4^{(M_J)}$	0	$-c^*/\sqrt{2}$	$d/\sqrt{2}$	0	$(\frac{5}{4\pi})^{1/2}R_4(r)r^{-2}$	0.292
	$-c/2\sqrt{3}$	0	$-c^*/2$	$2d/\sqrt{3}$		
	$d/\sqrt{6}$	$-c/\sqrt{2}$	0	$-\sqrt{(2/3)}c^*$		
	$-\sqrt{(2/3)}d$	0	$c^*/\sqrt{2}$	$-d/\sqrt{6}$		
	$-2d/\sqrt{3}$	$c/2$	0	$c^*/2\sqrt{3}$		
	0	$-d/\sqrt{2}$	$c/\sqrt{2}$	0		
$\Phi_5^{(M_J)}$	0	$c^*/2$	d	$-\sqrt{3}\,c/2$	$(\frac{5}{4\pi})^{1/2}R_5(r)r^{-2}$	0.002
	$-c/\sqrt{6}$	0	$-c^*/\sqrt{2}$	$-\sqrt{(2/3)}d$		
	$d/\sqrt{3}$	$c/2$	0	$c^*/2\sqrt{3}$		
	$-c/2\sqrt{3}$	0	$-c^*/2$	$-d/\sqrt{3}$		
	$\sqrt{(2/3)}d$	$c/\sqrt{2}$	0	$c^*/\sqrt{6}$		
	$\sqrt{3}\,c^*/2$	$-d$	$-c/2$	0		

---

† $a = z^2 - \frac{1}{2}(x^2 + y^2)$, $b = x^2 - y^2$, $c = z(x - iy)$, and $d = ixy$.

Table 3-2. The functions $\Phi_i^{(M_J)}$ for an axis of quantization along [111].[†] The radial functions, the amplitude factors, and $\Phi_0^{(M_J)}$ are the same as in Table 3-1.

M_J	$\frac{3}{2}$	$\frac{1}{2}$	$-\frac{1}{2}$	$-\frac{3}{2}$
$\Phi_1^{(M_J)}$	$\begin{vmatrix} 0 \\ \sqrt{3}\ A/4 \\ i\sqrt{3}\ A^*/4 \\ 0 \\ 0 \\ 0 \end{vmatrix}$	$\begin{vmatrix} A^*/2\sqrt{2} \\ 0 \\ -A/2\sqrt{2} \\ 0 \\ A^*/4 \\ iA^*/4 \end{vmatrix}$	$\begin{vmatrix} -iA/4 \\ -A/4 \\ 0 \\ A^*/2\sqrt{2} \\ 0 \\ -A/2\sqrt{2} \end{vmatrix}$	$\begin{vmatrix} 0 \\ 0 \\ 0 \\ -\sqrt{3}\ A/4 \\ \sqrt{3}\ A^*/4 \\ 0 \end{vmatrix}$
$\Phi_2^{(M_J)}$	$\begin{vmatrix} iB/\sqrt{6} \\ C/\sqrt{6} \\ -i\sqrt{2}\ C^*/\sqrt{3} \\ 0 \\ 0 \\ 0 \end{vmatrix}$	$\begin{vmatrix} C^*/3 \\ -2B/3 \\ -C/3 \\ B/3\sqrt{2} \\ C/3\sqrt{2} \\ -i\sqrt{2}\ C^*/3 \end{vmatrix}$	$\begin{vmatrix} i\sqrt{2}\ C/3 \\ -C^*/3\sqrt{2} \\ -B^*/3\sqrt{2} \\ C^*/3 \\ 2B^*/3 \\ -C/3 \end{vmatrix}$	$\begin{vmatrix} 0 \\ 0 \\ 0 \\ i\sqrt{2}\ C/\sqrt{3} \\ -C^*/\sqrt{6} \\ -iB^*/\sqrt{6} \end{vmatrix}$
$\Phi_3^{(M_J)}$	$\begin{vmatrix} 0 \\ -A/4\sqrt{3} \\ iA^*/4\sqrt{3} \\ -A/\sqrt{6} \\ -iA^*/\sqrt{6} \\ 0 \end{vmatrix}$	$\begin{vmatrix} -A^*/2\sqrt{2} \\ 0 \\ -A/2\sqrt{2} \\ 0 \\ A/4 \\ -iA^*/4 \end{vmatrix}$	$\begin{vmatrix} iA/4 \\ A^*/4 \\ 0 \\ A^*/2\sqrt{2} \\ 0 \\ A/2\sqrt{2} \end{vmatrix}$	$\begin{vmatrix} 0 \\ iA/\sqrt{6} \\ A^*/\sqrt{6} \\ -iA/4\sqrt{3} \\ A^*/4\sqrt{3} \\ 0 \end{vmatrix}$
$\Phi_4^{(M_J)}$	$\begin{vmatrix} -B/\sqrt{6} \\ -C/3\sqrt{6} \\ -i\sqrt{2}\ C^*/3\sqrt{3} \\ -2C/3\sqrt{3} \\ 4iC^*/3\sqrt{3} \\ 0 \end{vmatrix}$	$\begin{vmatrix} -C^*/3 \\ 0 \\ -C/3 \\ B/\sqrt{2} \\ C/3\sqrt{2} \\ i\sqrt{2}\ C^*/3 \end{vmatrix}$	$\begin{vmatrix} -i\sqrt{2}\ C/3 \\ -C^*/3\sqrt{2} \\ -B^*/\sqrt{2} \\ C^*/3 \\ 0 \\ C/3 \end{vmatrix}$	$\begin{vmatrix} 0 \\ -4iC/3\sqrt{3} \\ 2C^*/3\sqrt{3} \\ i\sqrt{2}\ C/3\sqrt{3} \\ C^*/3\sqrt{6} \\ B^*/\sqrt{6} \end{vmatrix}$
$\Phi_5^{(M_J)}$	$\begin{vmatrix} 0 \\ 2C/3\sqrt{3} \\ iC^*/3\sqrt{3} \\ \sqrt{2}\ C/3\sqrt{3} \\ i\sqrt{2}\ C^*/3\sqrt{3} \\ i\sqrt{2}\ B/\sqrt{3} \end{vmatrix}$	$\begin{vmatrix} -\sqrt{2}\ C^*/3 \\ 0 \\ -\sqrt{2}\ C/3 \\ 0 \\ -2C/3 \\ -iC^*/3 \end{vmatrix}$	$\begin{vmatrix} iC/3 \\ 2C^*/3 \\ 0 \\ \sqrt{2}\ C^*/3 \\ 0 \\ \sqrt{2}\ C/3 \end{vmatrix}$	$\begin{vmatrix} -i\sqrt{2}\ B^*/\sqrt{3} \\ -i\sqrt{2}\ C/3\sqrt{3} \\ -\sqrt{2}\ C^*/3\sqrt{3} \\ -iC/3\sqrt{3} \\ -2C^*/3\sqrt{3} \\ 0 \end{vmatrix}$

[†] $A = x^2 - y^2 - \frac{2i}{\sqrt{3}}[z^2 - \frac{1}{2}(x^2 + y^2)]$, $B = xy + yz + zx$, and
$C = [xy - \frac{1}{2}(x + y)] + \frac{3}{2}z(x - y)$.

then be arranged to form six independent functions, $\Phi_i^{(M_J)}$, each of which satisfies the correct symmetry of the $J = 3/2$ states. Suzuki, Okazaki, and Hasegawa (SOH)[21] have derived these functions in the (M_L, M_S) bases for an axis of quantization along the [001] direction as shown in Table 3-1. Here the members in each colum vector are labelled according to M_L and M_S, i.e., (1, 1/2), (0, 1/2). (-1, 1/2), (1, 1/2), (0, -1/2), and (-1, -1/2), respectively. Radial parts are given by

$$R_0(r) = (4/r_1{}^3)^{1/2} \exp(-r/r_1), \tag{3. 2}$$

$$R_i(r) = (8/45r_2{}^7)^{1/2}\, r^2 \exp(-r/r_2), \quad (i = 1, 2, 3, 4, 5) \tag{3. 3}$$

where the effective Bohr radii r_1 and r_2 are 37.8 and 29.9 Å, respectively.[21] Then the wave functions of the acceptor ground-state can be written in the form

$$\Psi^{(M_J)} = \sum_{i=0}^{5} c_i\, \Phi_i^{(M_J)}, \tag{3. 4}$$

where the c_i (i = 0, 1, 2, 3, 4, 5) are the amplitude factors and are listed in Table 3-1.[21]

The corresponding functions for the axis of quantization along the [111] direction can also derived by the same way. The functions $\Phi_i^{(M_J)}$ and c_i in this case have been derived by Fjeldly, Ishiguro, and Elbaum[28] as shown in Table 3-2.

B. Zeeman splitting of the acceptor ground-state

Several calculations have been reported on the Zeeman effect of the shallow acceptors in germanium. Some of these have utilized either the effective mass wave-functions or the effective mass formalism to obtain explicit

Table 3-3. g-values of the acceptor ground-state in germanium under H // [001].[a]

	g_1'	g_2'	$g_{1/2}'$	$g_{3/2}'$	
Bir *et al.*[b]	5.66	-0.26	5.60	5.10	(calculated)
SOH[c]	-1.44	0.56	-1.30	-0.19	(calculated)
LCW[d]	-1.13	0.63	-0.97	0.29	(calculated)
SP[e]	-1.73±0.11	0.78±0.07	-1.53±0.09	0.03±0.04	(boron)[e]
	-0.26±0.11	0.12±0.07	-0.22±0.09	0.03±0.04	(boron)[f]
Present	-0.16±0.08	0.08±0.04	-0.14±0.07	0.02±0.03	(gallium)

[a] The g-values are given using two notations. The relationships between these are $g_{1/2}' = g_1' + \frac{1}{4} g_2'$ and $g_{3/2}' = g_1' + \frac{9}{4} g_2'$.

[b] See Ref. 42.

[c] See Ref. 21.

[d] See Ref. 43.

[e] See Ref. 34.

[f] See text (Secs. VI-A and VI-D-1).

g-values and intensities of the Zeeman components of the optical spectra. The first such calculation is that of Bir *et al.*[42] in which the g-values of the acceptor ground-state are expressed in terms of those of the free holes using four-component wave-functions of the Kohn-Schechter type.[41] Only the linear Zeeman effect is considered. The results of Bir *et al.* are given in Table 3-3, where the g-values are tabulated using two notations. The g-values have also been calculated by SOH.[21] They have used an effective mass Zeeman Hamiltonian with six-component wave-functions, the latter being calculated by them using the valence-band parameters. A calculation identical to that of SOH, but using four-component wave-functions of Mendelson and James,[40] has been made by Lin-Chung and Wallis (LCW).[43] These results are also given in Table 3-3.

For the study of the Zeeman effect of the acceptor state in germanium and silicon, Bhattacharjee and Rodriguez (BR)[44] have adopted a group theoretical treatment. BR have derived the exact Zeeman Hamiltonian to obtain expressions for the energies of the Zeeman sublevels.

The application of the magnetic field $\vec{H}$ introduces a new term in the Hamiltonian of the acceptor holes. This additional term constitutes the Zeeman Hamiltonian[45]

$$H_{Zeeman} = -\mu_B(\vec{\ell} + 2\vec{s})\cdot\vec{H} - \frac{1}{2} m(\mu_B/\hbar)^2[r^2H^2 - (\vec{r}\cdot\vec{H})^2], \qquad (3.\ 5)$$

where μ_B is the Bohr magneton, m the free electron mass, $\vec{r}$ the position operator of the holes, $\vec{\ell}$ and $\vec{s}$ the orbital and the spin angular momenta in unit of $\hbar$, respectively.

From symmetry consideration, BR have constructed a most general form of the Zeeman-Hamiltonian matrix for the acceptor ground-state in terms of the angular momentum operator $\vec{J}$ ($J = 3/2$) as[44]

$$H_{Zeeman} = \mu_B g_1'(\vec{H}\cdot\vec{J}) + \mu_B g_2'(H_x J_x{}^3 + H_y J_y{}^3 + H_z J_z{}^3)$$

$$+ q_1 H^2 + q_2(\vec{H}\cdot\vec{J})^2 + q_3(H_x{}^2 J_x{}^2 + H_y{}^2 J_y{}^2 + H_z{}^2 J_z{}^2), \qquad (3.\ 6)$$

where the parameters g_1', g_2', q_1, q_2, and q_3 depend on the unperturbed wave functions of the acceptor ground-state. Here the components of $\vec{H}$ are referred to the cubic axes x, y, and z of the crystal.

Now we express the magnetic field by the polar angle θ and the azimuthal angle ϕ, i.e., $\vec{H} = H\vec{n}$ with

$$n_x = \sin\theta\cos\phi,\ n_y = \sin\theta\sin\phi,\ \text{and}\ n_z = \cos\theta. \qquad (3.\ 7)$$

Then the H_{Zeeman} becomes

$$H_{Zeeman} = \mu_B[g_1'(\vec{n}\cdot\vec{J}) + g_2'(n_x J_x{}^3 + n_y J_y{}^3 + n_z J_z{}^3)]$$

$$+ [q_1 + q_2(\vec{n}\cdot\vec{J})^2 + q_3(n_x{}^2 J_x{}^2 + n_y{}^2 J_y{}^2 + n_z{}^2 J_z{}^2)]H^2. \quad (3.\ 8)$$

For an arbitrary direction of the magnetic field, Eq.(3.8) is not necessarily diagonal in the $J = 3/2$ space. The expressions for the energies of the Zeeman sublevels in this case are obtained by diagonalizing the Hamiltonian matrix (3.8). However, the eigenfunctions are no longer defined by the states of $J = 3/2$.

When the magnetic field is applied in the [001] direction, the energies of the Zeeman sublevels are expressed as[44]

$$E_{M_J} = \mu_B(g_1'M_J + g_2'M_J{}^3)H + [q_1 + (q_2 + q_3)M_J{}^2]H^2, \qquad (3.\ 9)$$

where $M_J = 3/2$, $1/2$, $-1/2$, and $-3/2$. When the magnetic field is applied in the [111] direction, the energies of the Zeeman sublevles are derived as[44]

$$E_{\pm 3/2} = \pm\mu_B[(\tfrac{3}{2}g_1' + \tfrac{23}{8}g_2')^2 + \tfrac{1}{2}g_2']^{1/2}H + (q_1 + \tfrac{9}{4}q_2 + \tfrac{5}{4}q_3)H^2, \quad (3.\ 10)$$

$$E_{\pm 1/2} = \pm\mu_B(\tfrac{1}{2}g_1' + \tfrac{13}{8}g_2')H + (q_1 + \tfrac{1}{4}q_2 + \tfrac{5}{4}q_3)H^2. \quad (3.\ 11)$$

C. Interaction of the ultrasonic waves with the acceptor holes

The coupling of the acoustic phonons with the acceptor holes and the energy splittings of the acceptor ground-state are described by a strain Hamiltonian.[21] From symmetry consideration, Hasegawa[20] has constructed the strain Hamiltonian for the valence-band edge in terms of the angular momentum operator $\vec{L}$ ($L = 1$) as

$$H_{strain}^{\ v} = 2D_u[(L_x^{\ 2} - \tfrac{1}{3}L^2)e_{xx} + \text{C.P.}] + D_{u'}[(L_xL_y + L_yL_x)e_{xy} + \text{C.P.}], \quad (3.\ 12)$$

where L_α is α-component of the angular momentum operator ($\alpha = x$, y, and z refering to the four-fold axes). D_u and $D_{u'}$ are the deformation-potential constants of the valence band. C.P. denotes cyclic permutation of the indices x, y, and z. $e_{\alpha\beta}$ are the conventional strain components. The term, which gives the shift of the center of gravity of the valence-band edge, is ignored in Eq.(3.12).

A widely used alternative form of the strain Hamiltonian is written in terms of $\vec{J}$-operator acting only on the four Bloch states defined by $J = 3/2$.[21] This form is obtained by projecting $H_{strain}^{\ v}$ into the $J = 3/2$ space, while all informations about the d-like parts of the envelopes are simultaneously relegated to a set of the deformation-potential constants $D_u^{\ a}$ and $D_{u'}^{\ a}$ replacing D_u and $D_{u'}$, respectively, in Eq.(3.12) (superscript "a" stands for "acceptor"). Thus the strain Hamiltonian for the acceptor ground-state can be written as[21]

$$H_{strain}{}^{a} = \frac{2}{3} D_u{}^{a}[(J_x{}^2 - \frac{1}{3} J^2)e_{xx} + \text{C.P.}] + \frac{1}{3} D_{u'}{}^{a}[(J_xJ_y + J_yJ_x)e_{xy} + \text{C.P.}], \tag{3. 13}$$

where J_α is α-component of the angular momentum operator $\vec{J}$ ($J = 3/2$).

First we consider the energy splittings of the acceptor ground-state induced by applying the uniaxial stress. When the uniaxial stress $\vec{X}$ is applied in either the four-fold or the three-fold axis, the ground state splits into two Kramer's doublets $|M_J| = 3/2$ and $|M_J| = 1/2$,[20,22,46,47] with a separation Δ given by

$$\Delta = \langle\Psi^{(3/2)}|H_{strain}{}^{v}|\Psi^{(3/2)}\rangle - \langle\Psi^{(1/2)}|H_{srain}{}^{v}\ |\Psi^{(1/2)}\rangle$$

$$= \langle\tfrac{3}{2}|H_{strain}{}^{a}|\tfrac{3}{2}\rangle - \langle\tfrac{1}{2}|H_{strain}{}^{a}|\tfrac{1}{2}\rangle, \tag{3. 14}$$

where $\Psi^{(M_J)}$ are the six-column vectors given by Eq.(3.4). $|M_J\rangle$ represent the four acceptor-ground-state vectors corresponding to $J = 3/2$. This results in the following expressions for the energy splittings and for the connection between $D_u{}^{a}$ and D_u or $D_{u'}{}^{a}$ and $D_{u'}$: For $\vec{X}$ // [001],[21]

$$\Delta = \frac{4}{3} D_u{}^{a}(S_{11} - S_{12})X, \tag{3. 15}$$

$$D_u{}^{a} = D_u[c_0{}^2 + c_1{}^2 - c_3{}^2 - \tfrac{1}{2}(c_2 - c_4)^2 + \sqrt{2}\ (c_2 + c_4)c_5], \tag{3. 16}$$

where S_{11} and S_{12} are cubic compliance constants, and c_i (i = 0, 1, 2, 3, 4, 5) are given in Table 3-1. For $\vec{X}$ // [111],[21]

$$\Delta = \frac{2}{3} D_{u'}{}^{a} S_{44} X, \tag{3. 17}$$

$$D_{u'}{}^{a} = D_{u'}[c_0{}^2 - \tfrac{1}{2}(c_1 - c_3)^2 + \tfrac{1}{6}(3c_2{}^2 + 2c_2c_4 - 5c_4{}^2) - \tfrac{2\sqrt{2}}{3}(c_2 + c_4)c_5 + \tfrac{1}{3}c_5{}^2], \tag{3. 18}$$

where S_{44} is a cubic compliance constant, and c_i are given in Table 3-2. If we take only *s*-like parts as the acceptor-ground-state wave-functions, i.e., $c_0 = 1$ and $c_i = 0$ ($i = 1, 2, 3, 4, 5$), Eqs.(3.16) and (3.18) give the relations $D_u^{\,a} = D_u$ and $D_{u'}^{\,a} = D_{u'}$.

Next we calculate the matrix elements describing the interaction of the ultrasonic waves with the acceptor holes under the following assumptions: (1) The phonon dispersion is linear, which is a good approximation for the frequency range of the ultrasonic waves used in present investigation. (2) The crystal is elastically quasi-isotropic in such a way as to represent the true elastic properties of the given crystal as closely as possible, on the average. This leads to the average velocities as[48,49]

$$v_L = [(C_{11} - \tfrac{2}{5}\,C^*)/\rho]^{1/2},$$

$$v_T = [(C_{44} + \tfrac{1}{5}\,C^*)/\rho]^{1/2}, \qquad (3.\ 19)$$

where $C^* = C_{11} - C_{12} - 2C_{44}$ (C_{11}, C_{12}, and C_{44} are the three elastic constants for cubic crystals) and ρ is the crystal density.

The matrix elements are obtained in a straight forward manner by substituting an expansion in normal modes for the strain components into the stain Hamiltonian (3.13), and by using the acceptor-ground-state wave functions presented in Sec. III-A. The matrix elements will contain integrals over all space of the products between the various *s*-like and *d*-like parts of the wave functions, their radial parts, and a phase factor from the expansion of the strain components in normal modes. It is difficult to contain all these integrals. The essential information, however, is obtained by using "form factors" (cut-off functions) which reflect the admixture of the *d*-like parts to the wave functions in an average way.[28] This is done by taking the angular average over all directions of $\vec{q}$ before the spatial integral. Then, from the spatial integral involving only *s*-like parts, the form

$$f_0(q) = [1 + (qr_1/2)^2]^{-2} \tag{3. 20}$$

is obtained.[28] Another type of integrals contains the products of similar *d*-like parts and has the form[28]

$$f_2(q) = [1 - \tfrac{10}{3}(qr_2/2)^2 + (qr_2/2)^4]/[1 + (qr_2/2)^2]^6. \tag{3. 21}$$

In these expressions, r_1 and r_2 are the effective radii for the *s*-like and *d*-like parts, respectively, whose values are shown in Sec. III-A.

By adding the various contributions to the spatial integrals appearing in the matrix elements, the following two form factors are found:[28]

$$f^{I}(q) = c_0{}^2 f_0(q) + [c_1{}^2 - c_3{}^2 + \tfrac{1}{2}(c_2 - c_4)^2 + \surd 2\,(c_2 + c_4)c_5]f_2(q), \tag{3. 22}$$

$$f^{II}(q) = c_0{}^2 f_0(q) + [-\tfrac{1}{2}(c_1 - c_3)^2 + \tfrac{1}{6}(3c_2{}^2 + 2c_1c_4 - 5c_4{}^2) - \tfrac{2\surd 2}{3}(c_2 + c_4)c_5 + \tfrac{1}{3}c_5{}^2]f_2(q). \tag{3. 23}$$

By using the two form factors, the *q*-dependence of the deformation-potential constants can be expressed as[28]

$$D_u{}^a(q) = D_u[f^{I}(q)/f_0(q)] \quad \text{and} \quad D_{u'}{}^a(q) = D_{u'}[f^{II}(q)/f_0(q)]. \tag{3. 24}$$

In the phonon matrix elements, $f^{I}(q)$ is always associated with the appearence of the deformation-potential constant $D_u{}^a$ and $f^{II}(q)$ with the appearence of $D_{u'}{}^a$. For Ge numerical difference between the two is always small; less than 20 % for all q. This suggests the following approximation:[28]

$$f(q) = \tfrac{1}{2}\,[f^{I}(q) + f^{II}(q)] \simeq f^{I}(q) \simeq f^{II}(q). \tag{3. 25}$$

With these expressions, and after expanding the strain compnents in normal modes, the matrix elements of $H_{strain}{}^{a}$ take on the form[19,28]

$$<n|H_{strain}{}^{a}|n'> = \sum_{q,t} (\hbar\omega_{qt}/2Mv_t{}^2)^{1/2}(\tfrac{2}{3} D_{u'}{}^{a})(a_{qt} + a_{qt}^{\dagger})C_{qt}{}^{nn'} f(q), \tag{3. 26}$$

where the acceptor ground-states corresponding to $M_J = 3/2, 1/2, -1/2, -3/2$ are labeled by $n = 1, 2, 3, 4$, respectively. ω_{qt} is an angular frequency and a_{qt} and $a_{qt}{}^{\dagger}$ are destruction and creation operators, respectively, for the phonons of the wave vector $\vec{q}$ and in the branch t ($t = 1, 2$, and 3 refer to the longitudinal, the fast-transverse, and the slow-transverse branches, respectively). v_t is the sound velocity in branch t. The $C_{qt}{}^{nn'}$ are referred to coupling parameters.[27] They are related in the following way:

$$\begin{aligned} &C_{qt}{}^{11} = C_{qt}{}^{44} = -C_{qt}{}^{22} = -C_{qt}{}^{33}, \\ &C_{qt}{}^{12} = -C_{qt}{}^{34}, \quad C_{qt}{}^{13} = C_{qt}{}^{24}, \\ &C_{qt}{}^{14} = C_{qt}{}^{23} = 0, \quad C_{qt}{}^{nn'} = (C_{qt}{}^{n'n})^*. \end{aligned} \tag{3. 27}$$

When an axis of quantization is taken to an arbitrary direction of the crystal, M_J is not a good quantum number as described previously. For the two cases, where the axes of quantization are in the [001] and the [111] directions, the acceptor state are well defined by the $|M_J>$ states. In addition to the above described assumptions, we assume that the small amount of the d-like parts in the acceptor-ground-state wave-functions is ignored. Under these assumptions, we can obtain the explicit expressions of the coupling parameters $C_{qt}{}^{nn'}$ for these two cases in terms of the conventional polar angles (θ, ϕ), where $(0, \phi)$ denotes the [001] direction and $(\pi/2, 0)$ the [100] direction. Then, the $C_{qt}{}^{nn'}$ are calculated for the axis of quantization along both the [001][27] and the [111] directions[28] as given in Tables 3-4 and 3-5, respectively. In Table 3-5,[28]

$$C_{qt}^{12} = X_{1t} + X_{2t} + i(Y_{1t} + Y_{2t}),$$

$$C_{qt}^{13} = -\frac{1}{\sqrt{2}}Y_{1t} + \sqrt{2}\,Y_{2t} + i(-\frac{1}{\sqrt{2}}X_{1t} + \sqrt{2}\,X_{2t}). \tag{3. 28}$$

In these tables, $D = D_u{}^a/D_{u'}{}^a$.

We are interested in the cases where all acoustic phonons of three branches propagate along either the [001] or the [110] direction for two axes of quantization, the [001] and the [111] directions. For the axis of quantization along the [001] direction, the coupling parameters $C_{qt}^{nn'}$ are given in Tables 3-6(a) and 3-6(b) for the propagation along the [001] and the [110] directions, respectively. For the axis of quantization along the [111] direction, they are given in Tables 3-7(a) and 3-7(b), respectively. These tables indicate that the selection rules exist in the coupling of the relevant phonons with the acceptor holes.

Now we will derive the attenuation coefficient of the ultrasonic waves by using the above results. Following Kwok's method, the attenuation coefficient of the ultrasonic waves by the acceptor holes is expressed by[19]

$$\alpha = \frac{\omega_{qt}}{\rho v_t^3}\frac{\hbar\omega_{qt}}{kT}\sum_{n,n'} N_n(\frac{2}{3}D_{u'}{}^a)^2|C_{qt}^{nn'}|^2 \frac{\Gamma_n + \Gamma_{n'}}{(\hbar\omega_{qt} - E_{n'n})^2 + (\Gamma_n + \Gamma_{n'})^2}, \tag{3. 29}$$

where

$$E_{n'n} = E_{n'} - E_n, \tag{3. 30}$$

and N_n and Γ_n are the number of holes per unit volume and the level width in the n-th level, respectively.

Table 3-4. Coupling parameters $C_{qt}^{nn'}$ for an axis of quantization along the [001] direction in the quasi-isotropic approximation.

t	1	2	3
C_{qt}^{11}	$(D/2)(3\cos^2\theta - 1)$	$-(3D/4)\sin 2\theta$	0
C_{qt}^{12}	$(\sqrt{3}/2)\sin 2\theta \times (\cos\phi - i\sin\phi)$	$(\sqrt{3}/2)\cos 2\theta \times (\cos\phi - i\sin\phi)$	$-(\sqrt{3}/2)\cos\theta \times (\sin\phi - i\cos\phi)$
C_{qt}^{13}	$(\sqrt{3}/2)\sin^2\theta \times (D\cos 2\phi - i\sin 2\phi)$	$(\sqrt{3}/4)\sin 2\theta \times (D\cos 2\phi - i\sin 2\phi)$	$-(\sqrt{3}/2)\sin\theta \times (D\sin 2\phi - i\cos 2\phi)$

Table 3-5. C_{qt}^{11}, X_{1t}, X_{2t}, Y_{1t}, and Y_{2t} for an axis of quantization along the [111] direction in the quasi-isotropic approximation.[†]

t	1	2	3
C_{qt}^{11}	$(1/2)\sin^2\theta\sin2\phi$ $+(1/2)\sin2\theta(\sin\phi+\cos\phi)$	$-(1/4)\sin2\theta\sin2\phi$ $-(1/2)\cos2\theta(\cos\phi+\sin\phi)$	$-(1/2)\sin\theta\cos2\phi$ $-(1/2)\cos\theta(\cos\phi-\sin\phi)$
X_{1t}	$(D/\sqrt{2})\sin^2\theta\cos2\phi$	$-(D/2\sqrt{2})\sin2\theta\cos2\phi$	$(D/\sqrt{2})\sin\theta\sin2\phi$
X_{2t}	$(1/2\sqrt{2})\sin2\theta(\cos\phi-\sin\phi)$	$-(1/2\sqrt{2})\cos2\theta(\cos\phi-\sin\phi)$	$(1/2\sqrt{2})\cos\theta(\cos\phi+\sin\phi)$
Y_{1t}	$(D/\sqrt{6})(3\cos^2\theta-1)$	$(\sqrt{3}/2\sqrt{2})D\sin2\theta$	0
Y_{2t}	$-(1/2\sqrt{6})[2\sin^2\theta\cos2\phi$ $-\sin2\theta(\sin\phi$ $+\cos\phi)]$	$(1/2\sqrt{6})[\sin2\theta\cos2\phi$ $-\cos2\theta(\sin\phi$ $+\cos\phi)]$	$(1/2\sqrt{6})[2\sin\theta\cos2\phi$ $-\cos\theta(\cos\phi$ $-\sin\phi)]$

[†] The coupling parameters C_{qt}^{12} and C_{qt}^{13} are expressed in terms of X_{1t}, X_{2t}, Y_{1t}, and Y_{2t} as shown by Eq.(3.28) in the text.

Table 3-6. Values of coupling parameters $C_{qt}^{nn'}$ for an axis of quantization along the [001] direction.

(a) For $\vec{q}$ // [001].

t	1	2	3
C_{qt}^{11}	D	0	0
C_{qt}^{12}	0	$(\sqrt{3}/2)(\cos\phi-i\sin\phi)$	$-i(\sqrt{3}/2)(\sin\phi-i\cos\phi)$
C_{qt}^{13}	0	0	0

(b) For $\vec{q}$ // [110].

t	1	2	3
C_{qt}^{11}	$-D/2$	0	0
C_{qt}^{12}	0	$\pm(\sqrt{6}/4)(1-i)$	0
C_{qt}^{13}	$-\sqrt{3}i/2$	0	$-\sqrt{3}D/2$

Table 3-7. Values of coupling parameters $C_{qt}^{nn'}$ for an axis of quantization along the [111] direction.

(a) For $\vec{q}$ // [001].

t	1	2	3
C_{qt}^{11}	0	$1/2$	$-1/2$
C_{qt}^{12}	$D/\sqrt{2}-i(D+1)/\sqrt{6}$	$1/2\sqrt{2}+i/2\sqrt{6}$	$i/\sqrt{6}$
C_{qt}^{13}	$(D-2)/2\sqrt{3}-iD/2$	$1/2\sqrt{3}+i/2$	$1/\sqrt{3}$

(b) For $\vec{q}$ // [110].

t	1	2	3
C_{qt}^{11}	$1/2$	$1/\sqrt{2}$	0
C_{qt}^{12}	$-iD/\sqrt{6}$	$i/2\sqrt{3}$	$D/\sqrt{2}$
C_{qt}^{13}	$D/2\sqrt{3}$	$1/\sqrt{6}$	$-iD/2$

In order to make the calculation tractable, Suzuki and Mikoshiba (SM)[19] have made the following assumptions and approximations: (1) The ground-state quartet is split by random local strains by an amount Δ, the distribution of which has the Gaussian/Lorentzian form. We take the Gaussian form here, i.e.,

$$g(\Delta) = (2\pi)^{-1/2}\,\sigma^{-1}\,\exp[-(\Delta - \Delta_0)^2/2\sigma^2], \qquad (3.\ 31)$$

where Δ_0 is the average value of Δ and σ the variance. (2) The level width Γ_n is determined by the direct (one-phonon)[14] and the Raman (two-phonon)[50] processes, i.e.,

$$\Gamma_n = \Gamma_n^{\ d} + \Gamma_{Rn}. \qquad (3.\ 32)$$

The Γ_{Rn} is almost independent of n and is given by[19,50]

$$\Gamma_R \simeq \Gamma_{Rn}\ (n = 1,\ 2,\ 3,\ 4)$$

$$\simeq \frac{(1 + D^2)}{25\pi^3\rho^2\hbar^6}\left(\frac{2}{3}D_{u'}^{\ a}\right)^4 (kT)^5 \int_0^\infty dx\,\frac{x^4\,e^x}{(e^x - 1)^2}\,Q(xkT), \qquad (3.\ 33)$$

$$Q(E) = v_L^{\ -5} f^2\left(\frac{E}{\hbar v_L}\right) + \frac{3}{2}\,v_T^{\ -5} f^2\left(\frac{E}{\hbar v_T}\right), \qquad (3.\ 34)$$

where $\omega \equiv \omega_{qt}$, $x \equiv \hbar\omega/kT$, and $D = D_u^{\ a}/D_{u'}^{\ a}$. v_L and v_T are the average velocities. $f(q)$ is the form factor given by Eq.(3.25) which is expressed approximately by

$$f(q) = [1 + (qa^*/2)^2]^{-2}, \qquad (3.\ 35)$$

where a^* is the effective Bohr radius of the acceptor ground-state. The $\Gamma_n^{\ d}$ is given for each case as described later. (3) The internal strains are represented by the normal stresses in the [111] and its equivalent directions. Under these assumptions and approximations mentioned above, the measured attenuation coefficient α is obtained by integrating $\alpha(\Delta)$ which is a function of the local splitting Δ as

$$\alpha = \int_{-\infty}^{\infty} \alpha(\Delta) g(\Delta) d\Delta. \qquad (3.\ 36)$$

First, we consider the attenuation in the absence of the magnetic field. Since the acceptor-ground-state quartet is split into two Kramer's doublets, $|M_J| = 3/2$ and $|M_J| = 1/2$ levels, we denote them by $n = 1$ and $n = 2$, respectively. The axis of quantization is taken to be in the [111] and its equivalent directions. Then, the attenuation coefficient $\alpha(\Delta)$ for the fast-transverse waves propagating along the [110] direction is given by

$$\alpha(\Delta) = \frac{N\hbar\omega^2}{\rho v_2{}^3} \left(\frac{2}{3} D_{u'}{}^{a}\right)^2 [\alpha_1(\Delta) + \alpha_2(\Delta)], \qquad (3.\ 37)$$

$$\alpha_1(\Delta) = \frac{\beta_1}{2kT} \left[N_1 \frac{2\,\Gamma_1}{(\hbar\omega)^2 + 4\Gamma_1{}^2} + N_2 \frac{2\,\Gamma_2}{(\hbar\omega)^2 + 4\Gamma_2{}^2}\right], \qquad (3.\ 38)$$

$$\alpha_2(\Delta) = \frac{\beta_2}{kT} \left[N_2 \frac{\Gamma_1 + \Gamma_2}{(\hbar\omega - \Delta)^2 + (\Gamma_1 + \Gamma_2)^2} + N_1 \frac{\Gamma_1 + \Gamma_2}{(\hbar\omega + \Delta)^2 + (\Gamma_1 + \Gamma_2)^2}\right], \qquad (3.\ 39)$$

with

$$N_1 = [1 + \exp(\Delta/kT)]^{-1}, \quad N_2 = [1 + \exp(-\Delta/kT)]^{-1}; \qquad (3.\ 40)$$

$$\Gamma_1{}^d = \Gamma_0[1 - \exp(-\Delta/kT)]^{-1}, \quad \Gamma_2{}^d = \Gamma_0[\exp(\Delta/kT) - 1]^{-1}; \qquad (3.\ 41)$$

$$\Gamma_0 = \frac{2(1 + D^2)}{45\pi\rho} (\Delta/\hbar)^3 (D_{u'}{}^{a})^2 Q(\Delta), \qquad (3.\ 42)$$

where β_1 and β_2 are scaling factors ($0 < \beta_1, \beta_2 < 1$) which are determined by the best fit of the calculation with the experiment. They are required because the stresses in the <111> directions give larger contribution to the attenuation than that in the other directions.[19] Moreover, β_2 contains the saturation effect of the hole population due to the resonance absorption of the ultrasonic waves.[51] For the other mode and the other propagation direction, the similar expressions of the attenuation coefficient can be obtained. It should be remarked that the attenuation coefficient consists of the relaxation term α_1 and the resonance term α_2.

Next, we consider the attenuation in the presence of the magnetic field and/or the uniaxial stress. In this case, the derivation of the expression of the attenuation coefficient is fairly complicated. However, when the splittings induced by the external fields are larger than the internal splittings, we can easily obtain the expressions. We derive the analytic expressions for the axes of quantization along either the [001] or the [111] direction. For the other directions, we cannot obtain the analytic expressions as described previously.

When the magnetic field and the uniaxial stress are applied in the [001] direction, the expressions of $E_{nn'}$ and Γ_n^d are expressed as follow: From Eqs.(3.9) and (3.15),

$$E_{12} = \Delta_0 + \zeta X + \mu_B(g_1' + \frac{13}{4} g_2')H + 2(q_2 + q_3)H^2, \tag{3. 43}$$

$$E_{13} = \Delta_0 + \zeta X + \mu_B(2g_1' + \frac{7}{2} g_2')H + 2(q_2 + q_3)H^2, \tag{3. 44}$$

$$E_{42} = \Delta_0 + \zeta X - \mu_B(2g_1' + \frac{7}{2} g_2')H + 2(q_2 + q_3)H^2, \tag{3. 45}$$

$$E_{43} = \Delta_0 + \zeta X - \mu_B(g_1' + \frac{13}{4} g_2')H + 2(q_2 + q_3)H^2, \tag{3. 46}$$

where $\zeta = (4/3)D_u^a(S_{11} - S_{12})$. Following the results by Kwok,[14]

$$\Gamma_1^{d} = \frac{(D_{u}'^{a})^2}{45\pi\rho\hbar^3}\left[E_{12}^3\frac{2}{1-\exp(-E_{12}/kT)}Q(E_{12}) + E_{13}^3\frac{D^2+1}{1-\exp(-E_{13}/kT)}Q(E_{13})\right], \tag{3. 47}$$

$$\Gamma_2^{d} = \frac{(D_{u}'^{a})^2}{45\pi\rho\hbar^3}\left[E_{21}^3\frac{2}{1-\exp(-E_{21}/kT)}Q(E_{21}) + E_{24}^3\frac{D^2+1}{1-\exp(-E_{24}/kT)}Q(E_{24})\right], \tag{3. 48}$$

$$\Gamma_3^{d} = \frac{(D_{u}'^{a})^2}{45\pi\rho\hbar^3}\left[E_{31}^3\frac{D^2+1}{1-\exp(-E_{31}/kT)}Q(E_{31}) + E_{34}^3\frac{2}{1-\exp(-E_{34}/kT)}Q(E_{34})\right], \tag{3. 49}$$

$$\Gamma_4^{d} = \frac{(D_{u}'^{a})^2}{45\pi\rho\hbar^3}\left[E_{42}^3\frac{D^2+1}{1-\exp(-E_{42}/kT)}Q(E_{42}) + E_{43}^3\frac{2}{1-\exp(-E_{43}/kT)}Q(E_{43})\right], \tag{3. 50}$$

where $Q(E)$ is given by Eq.(3.34). N_n is expressed by

$$N_n = N\left[\sum_{i=1}^{4}\exp(-E_{ni}/kT)\right]^{-1}, \tag{3. 51}$$

where N is the acceptor concentration per unit volume. The coupling parameters $C_{qt}^{nn'}$ are changed with respect to the acoustic mode or the propagation direction. For both the transverse waves (t = 2) propagating along the [001] direction and the fast-transverse waves (t = 2) propagating along the [110] direction, according to Tables 3-6(a) and 3-6(b), respectively,

$$\begin{gathered} |C_{q2}^{nn}|^2 = 0 \quad (n = 1, 2, 3, 4), \\ |C_{q2}^{12}|^2 = |C_{q2}^{34}|^2 = 0.75, \ |C_{q2}^{13}|^2 = |C_{q2}^{24}|^2 = 0. \end{gathered} \tag{3. 52}$$

For the longitudinal waves (t = 1) propagating along the [001] direction, according to Table 3-7(a),

$$\begin{gathered} |C_{q1}^{nn}|^2 = D^2/4 \quad (n = 1, 2, 3, 4), \\ |C_{q1}^{12}|^2 = |C_{q1}^{34}|^2 = |C_{q1}^{13}|^2 = |C_{q1}^{24}|^2 = 0. \end{gathered} \tag{3. 53}$$

On the other hand, when the magnetic field is applied in the [111] direction, the expressions of $E_{n'n}$ and $\Gamma_n^{\,d}$ are obtained from Eqs.(3.10) and (3.11), and using the Kwok's results, respectively, as follow:

$$E_{12} = \Delta_0 + \mu_B[\{(\tfrac{3}{2}\,g_1' + \tfrac{23}{8}\,g_2')^2 + \tfrac{1}{2}\,g_2'\}^{1/2} - (\tfrac{1}{2}\,g_1' + \tfrac{23}{8}\,g_2')]H + 2q_2H^2, \tag{3. 54}$$

$$E_{13} = \Delta_0 + \mu_B[\{(\tfrac{3}{2}\,g_1' + \tfrac{23}{8}\,g_2')^2 + \tfrac{1}{2}\,g_2'\}^{1/2} + (\tfrac{1}{2}\,g_1' + \tfrac{23}{8}\,g_2')]H + 2q_2H^2, \tag{3. 55}$$

$$E_{42} = \Delta_0 - \mu_B[\{(\tfrac{3}{2}\,g_1' + \tfrac{23}{8}\,g_2')^2 + \tfrac{1}{2}\,g_2'\}^{1/2} + (\tfrac{1}{2}\,g_1' + \tfrac{23}{8}\,g_2')]H + 2q_2H^2, \tag{3. 56}$$

$$E_{43} = \Delta_0 - \mu_B[\{(\tfrac{3}{2}\,g_1' + \tfrac{23}{8}\,g_2')^2 + \tfrac{1}{2}\,g_2'\}^{1/2} - (\tfrac{1}{2}\,g_1' + \tfrac{23}{8}\,g_2')]H + 2q_2H^2; \tag{3. 57}$$

$$\Gamma_1^{\,d} = \frac{2(D_{u'}^{\,a})^2}{135\pi\rho\hbar^3}[E_{12}^{\,3}\frac{2D^2+1}{1-\exp(-E_{12}/kT)}\,Q(E_{12}) + E_{13}^{\,3}\frac{D^2+2}{1-\exp(-E_{13}/kT)}\,Q(E_{13})], \tag{3. 58}$$

$$\Gamma_2^{\,d} = \frac{2(D_{u'}^{\,a})^2}{135\pi\rho\hbar^3}[E_{21}^{\,3}\frac{2D^2+1}{1-\exp(-E_{21}/kT)}\,Q(E_{21}) + E_{24}^{\,3}\frac{D^2+2}{1-\exp(-E_{24}/kT)}\,Q(E_{24})], \tag{3. 59}$$

$$\Gamma_3^{\,d} = \frac{2(D_{u'}^{\,a})^2}{135\pi\rho\hbar^3}[E_{31}^{\,3}\frac{D^2+2}{1-\exp(-E_{31}/kT)}\,Q(E_{31}) + E_{34}^{\,3}\frac{2D^2+1}{1-\exp(-E_{34}/kT)}\,Q(E_{34})], \tag{3. 60}$$

$$\Gamma_4^{\,d} = \frac{2(D_{u'}^{\,a})^2}{135\pi\rho\hbar^3}[E_{42}^{\,3}\frac{D^2+2}{1-\exp(-E_{42}/kT)}\,Q(E_{42}) + E_{43}^{\,3}\frac{2D^2+1}{1-\exp(-E_{43}/kT)}\,Q(E_{43})]. \tag{3. 61}$$

The expression of N_n is also given by Eq.(3.52) in this case. The coupling parameters $C_{qt}^{\,nn'}$ are also changed with respect to the acoustic mode or the propagation direction, which is derived from Tables 3-7(a) and 3-7(b): for example, for the transverse waves ($t = 2$) propagating along the [001] direction,

$$|C_{q2}^{\,nn}|^2 = 1/4 \quad (n = 1,\ 2,\ 3,\ 4),$$
$$|C_{q2}^{\,12}|^2 = |C_{q2}^{\,34}|^2 = 1/6, \quad |C_{q2}^{\,13}|^2 = |C_{q2}^{\,24}|^2 = 1/3. \tag{3. 62}$$

It should be noted that the attenuation coefficient obtained above is functions of Δ, $\vec{H}$, or $\vec{X}$, i.e., $\alpha(\Delta,\vec{H},\vec{X})$. As for Δ, we can integrate according to Eq.(3.36). The effects of $\vec{H}$ and $\vec{X}$ appear through $E_{nn'}$, and $\Gamma_n^{\,d}$ in the attenuation coefficient (3.29). If the attenuation is measured as a function of the external magnetic field, we will meet the field at which $\hbar\omega_{qt} = E_{n'n}$ $(n' \neq n)$. This results in the resonance attenuation of the ultrasonic waves. Generally speaking, the attenuation coefficient consists of two terms in the presence of the magnetic field, which is similar to the case in the absence of the magnetic field described previously: one is the resonance term and the other the relaxation term which exists under the condition of $|C_{qt}^{\;nn}|^2 \neq 0$. In summary, the measured attenuation coefficient is given by

$$\alpha = \int_{-\infty}^{\infty} d\Delta\; \alpha(\Delta,\vec{H},\vec{X})g(\Delta)$$

$$= \alpha_{resonance}(\vec{H},\vec{X}) + \alpha_{relaxation}(\vec{H},\vec{X}). \tag{3. 63}$$

Numerical calculations described in later sections reveal that the relaxation attenuation is small compared with the resonance attenuation below 4.2 K and is henceforth disregarded in the present investigation in most cases. Moreover, when we compare the attenuation coefficient described above with the observations, we introduce a scaling factor β in the presence of the magnetic field by the same reasons as β_1 and β_2.

IV. EXPERIMENTAL RESULTS

A. Temperature dependence of the attenuation in the absence of the magnetic field

Prior to the description of the magnetoacoustic resonance attenuation (MARA), we show the temperature dependence of the ultrasonic attenuation in the absence of the magnetic field. The attenuation was measured in the temperature range 1.3 to 45 K at various acoustic power levels in four samples with different concentrations (Table 2-1).

Figure 4-1 shows the temperature dependences of the attenuation of the 1.11 GHz-fast-transverse waves propagating along the [110] direction in #15LB at four acoustic power levels. The attenuation increases with decreasing the temperature below 15 K except for the case of 6 mW/cm^2, which changes little with the temperature. The residual attenuations of ∿4 dB/cm are caused by the following facts; the scattering by defects, the lack of the parallelism of the sample faces, and the interference of the ultrasonic waves reflected at two faces of a ZnO film. The attenuations at low temperatures decrease with increasing the acoustic power; the saturation effect[51] is observed. The temperature dependences of the 1.23 GHz-transverse waves propagating along the [001] direction in #15LA are shown in Fig. 4-2 at three acoustic power levels. The feature of the temperature dependence is similar to the case shown in Fig. 4-1. The temperature dependence of the longitudinal waves in these samples is similar to that of the transverse waves except for an amount of the attenuation, which is small reflecting the fast propagation of the former waves.

The results for the 1.06 GHz-transverse waves and the 1.28 GHz-longitudinal waves propagating along the [001] direction in #15H are shown in Figs. 4-3 and 4-4, respectively. The feature of the temperature dependence is similar to the cases in #15LA and #15LB except for an attenuation increment near 7 K. This increment becomes clear with increasing the acoustic power. The temper-

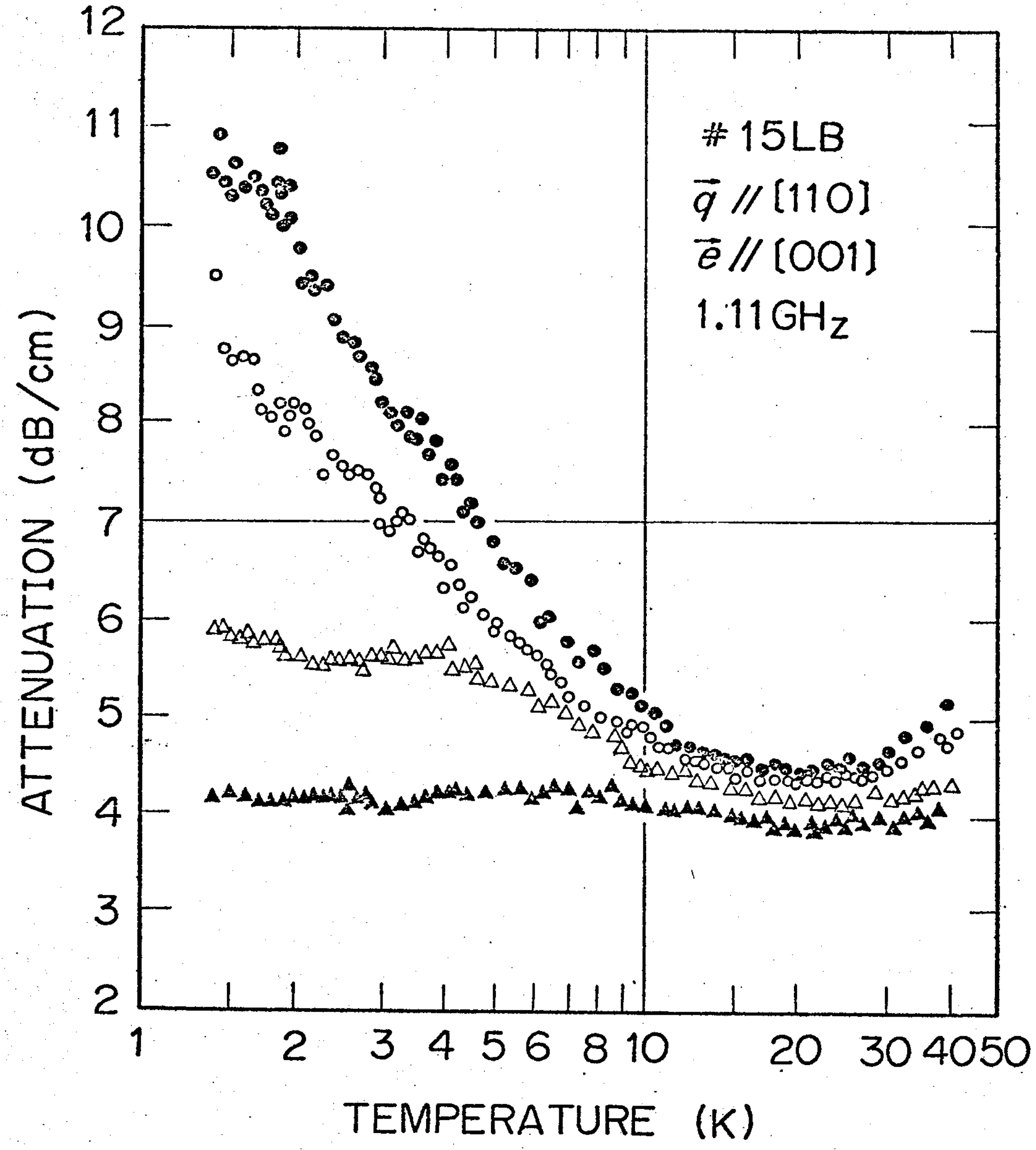

FIG. 4-1. Temperature dependences of the attenuation of the 1.11 GHz-fast-transverse waves propagating along the [110] direction in #15LB. Closed and open circles denote the attenuation at the acoustic power levels of 0.01 and 0.06 mW/cm^2, respectively. Open and closed triangles denote those at 0.6 and 6 mW/cm^2, respectively.

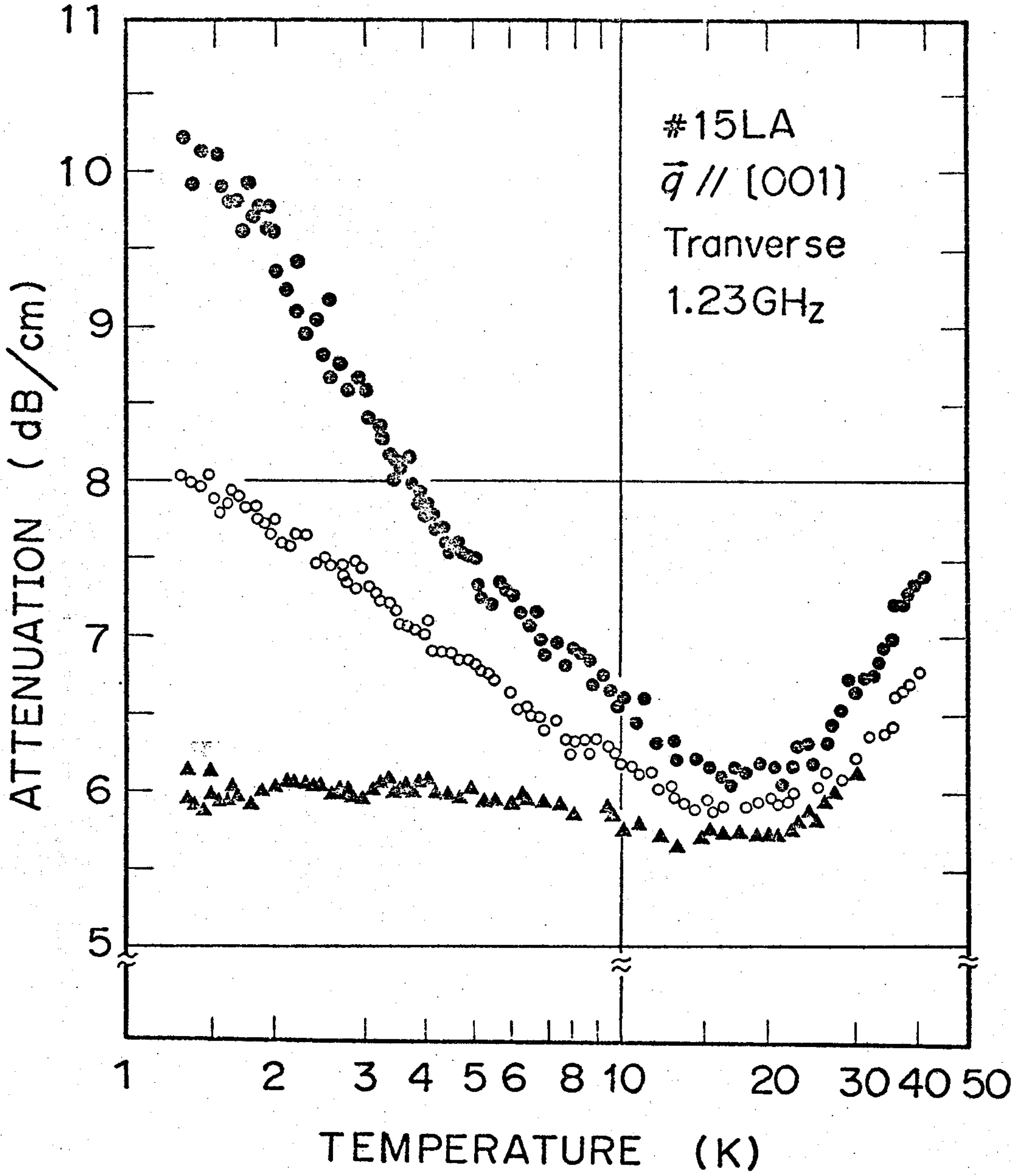

FIG. 4-2. Temperature dependences of the attenuation of the 1.23 GHz-transverse waves propagating along the [001] direction in #15LA. Closed circles, open circles, and closed triangles denote the attenuations at the acoustic power levels of 0.06, 0.2, and 2 mW/cm^2, respectively.

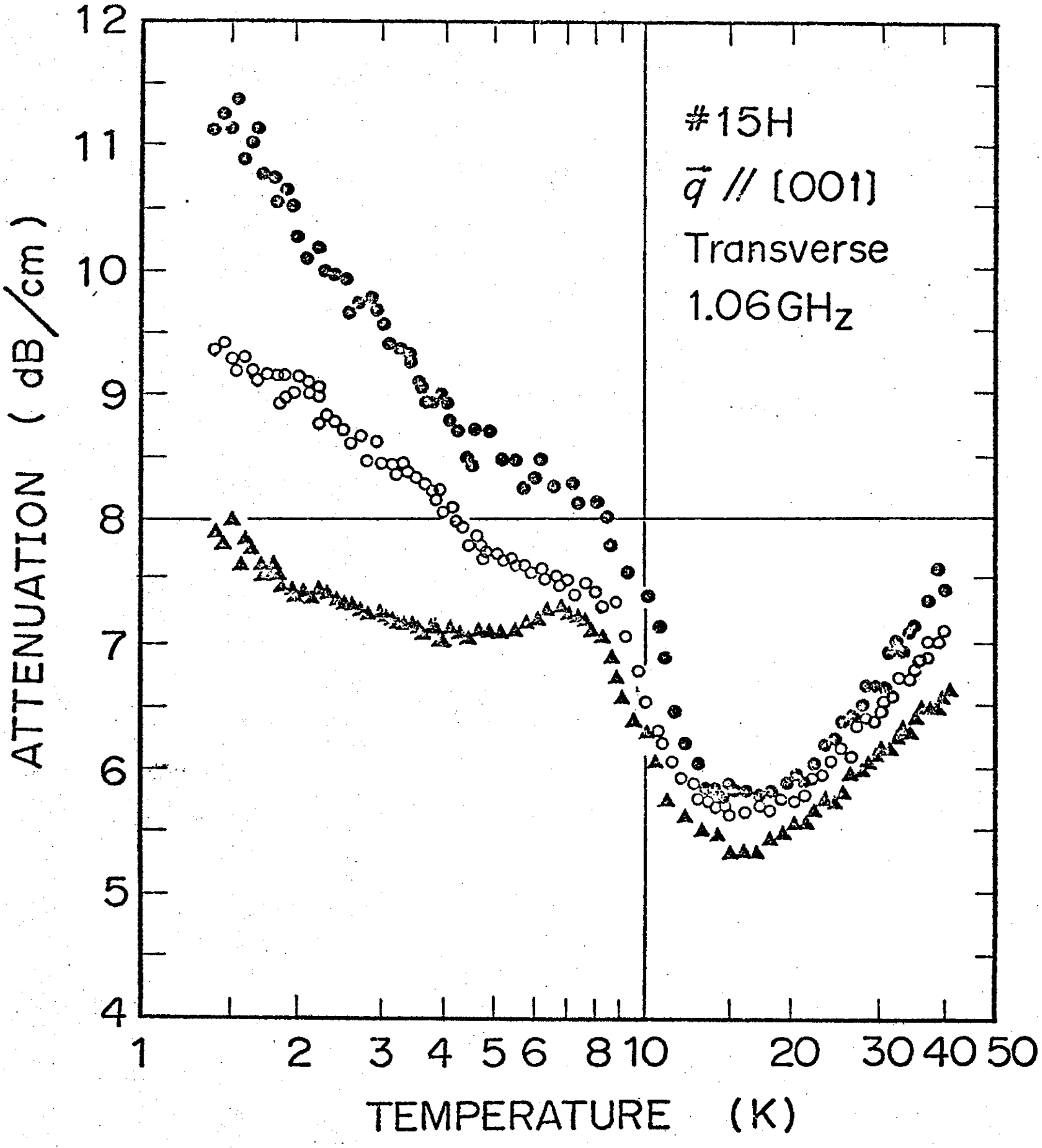

FIG. 4-3. Temperature dependences of the attenuation of the 1.06 GHz-transverse waves propagating along the [001] direction in #15H. Closed circles, open circles, and closed triangles denote the attenuations at the acoustic power levels of 0.03, 0.1, and 1 mW/cm^2, respectively.

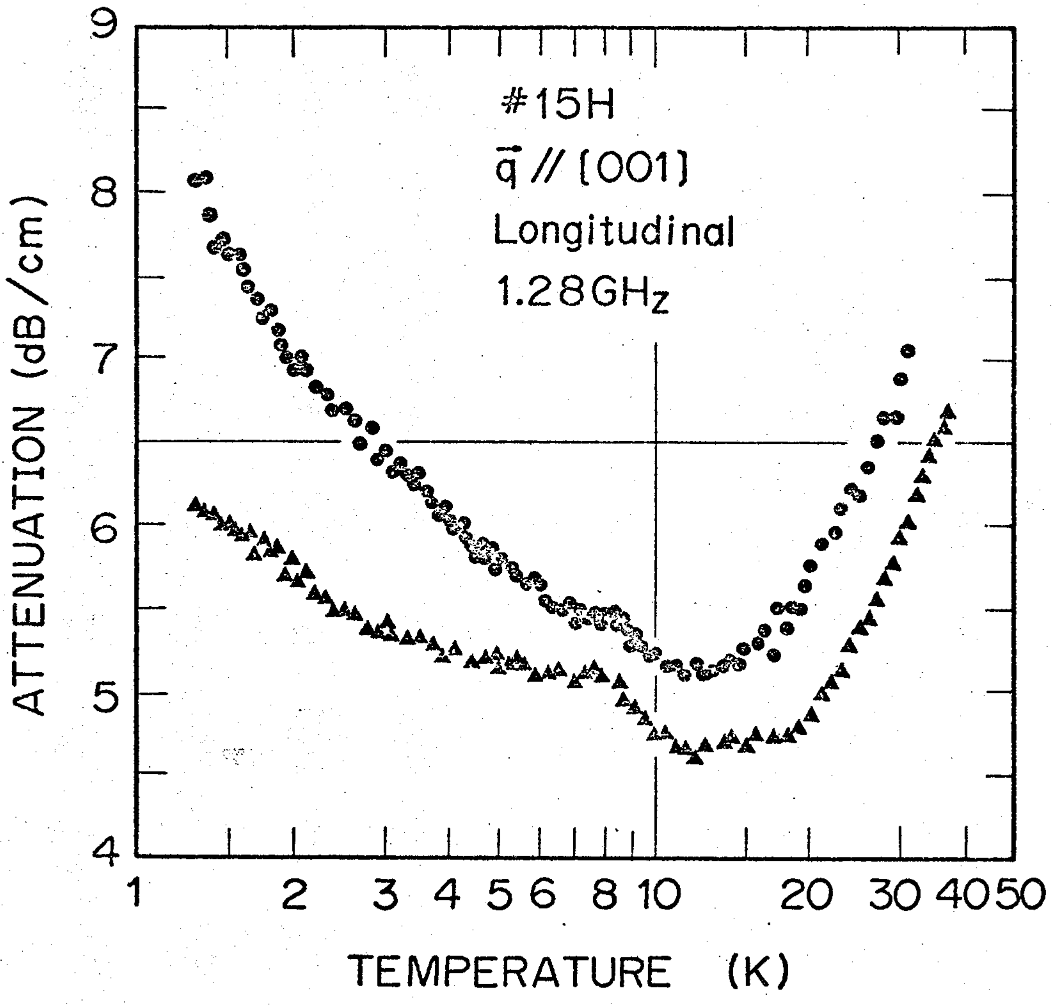

FIG. 4-4. Temperature dependences of the attenuations of the 1.28 GHz-longitudinal waves propagating along the [001] direction in #15H. Closed circles and closed triangles denote the attenuations at the acoustic power levels of 0.1 and 0.5 mW/cm^2, respectively.

ature dependence of the attenuation in #16L is similar to the case in #15H except for an amount of the attenuation.

B. Magnetoacoustic resonance attenuation (MARA)

1. Magnetic field dependence of the ultrasonic attenuation by the acceptor holes

We measured the magnetic field dependence of the ultrasonic attenuation in five samples (Table 2-1). The magnetic field up to 120 kG was applied in the $(1\bar{1}0)$ plane. The attenuation was measured in the temperature range 1.3 to 4.2 K at a fixed acoustic power.

The effect of the magnetic field on the attenuation of the 1.23 GHz-transverse waves propagating along the [001] direction in #15LA is shown in Fig. 4-5. Since the magnetic field was monitored by the magnetoresistance of the copper wire, the abscissa is not evenly spaced because of its non-linearlity (hereafter we use this abscissa in most cases). When the magnetic field is applied in the [001] direction, the attenuation is characterized by four peaks *A*, *B*, *C*, and *D*. When the magnetic field is applied in the [111] direction, the attenuation shows four peaks *a*, *b*, *c*, and *d* at different fields from the above. We regard these peaks as the resonance-attenuation peaks, since they appear in the limited field region, shift with the acoustic frequency, and saturate with increasing the acoustic power. The background attenuation rapidly decreases up to 20 - 30 kG and then is almost constant up to 120 kG. The overall behavior of the magnetic field dependence is similar in #15H and #16L as shown in Fig. 4-6.

We show that these resonance behaviors are specific to the attenuation by the acceptor holes in germanium.[32,33,52] We could observe the MARA in neither B-doped Si nor Zn-doped GaP, though we could observe the attenuation by the acceptor holes which are characterized by the increase with decreasing the temperature below 20 K.[24] In Fig. 4-7 are shown the magnetic field

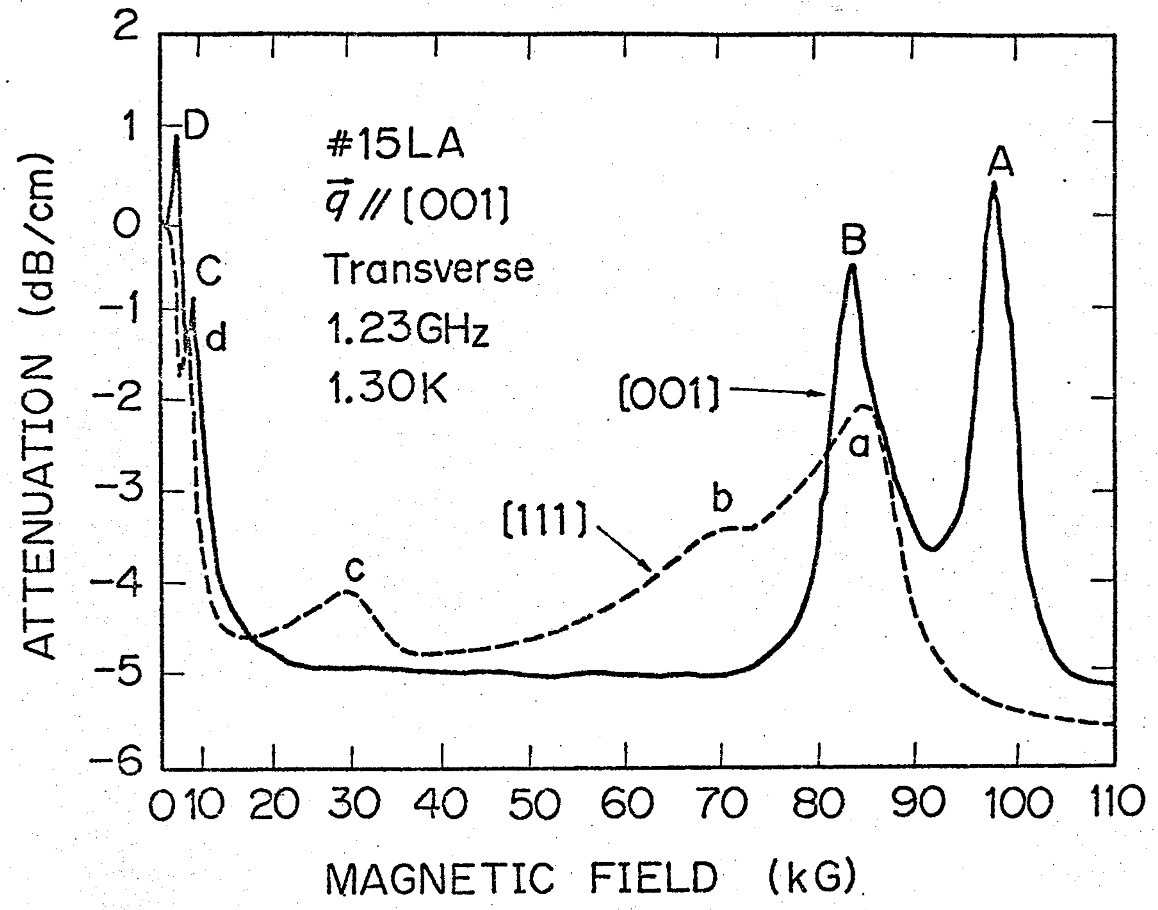

FIG. 4-5. Magnetic field dependences of the attenuation of the 1.23 GHz-transverse waves propagating along the [001] direction in #15LA at 1.3 K and at the acoustic power level of 0.06 mW/cm^2. The Miller indices attached to the lines indicate the direction of the magnetic field. The peaks are assigned by *A*, *B*, *C*, and *D* for $\vec{H}$ // [001], and by *a*, *b*, *c*, and *d* for $\vec{H}$ // [111].

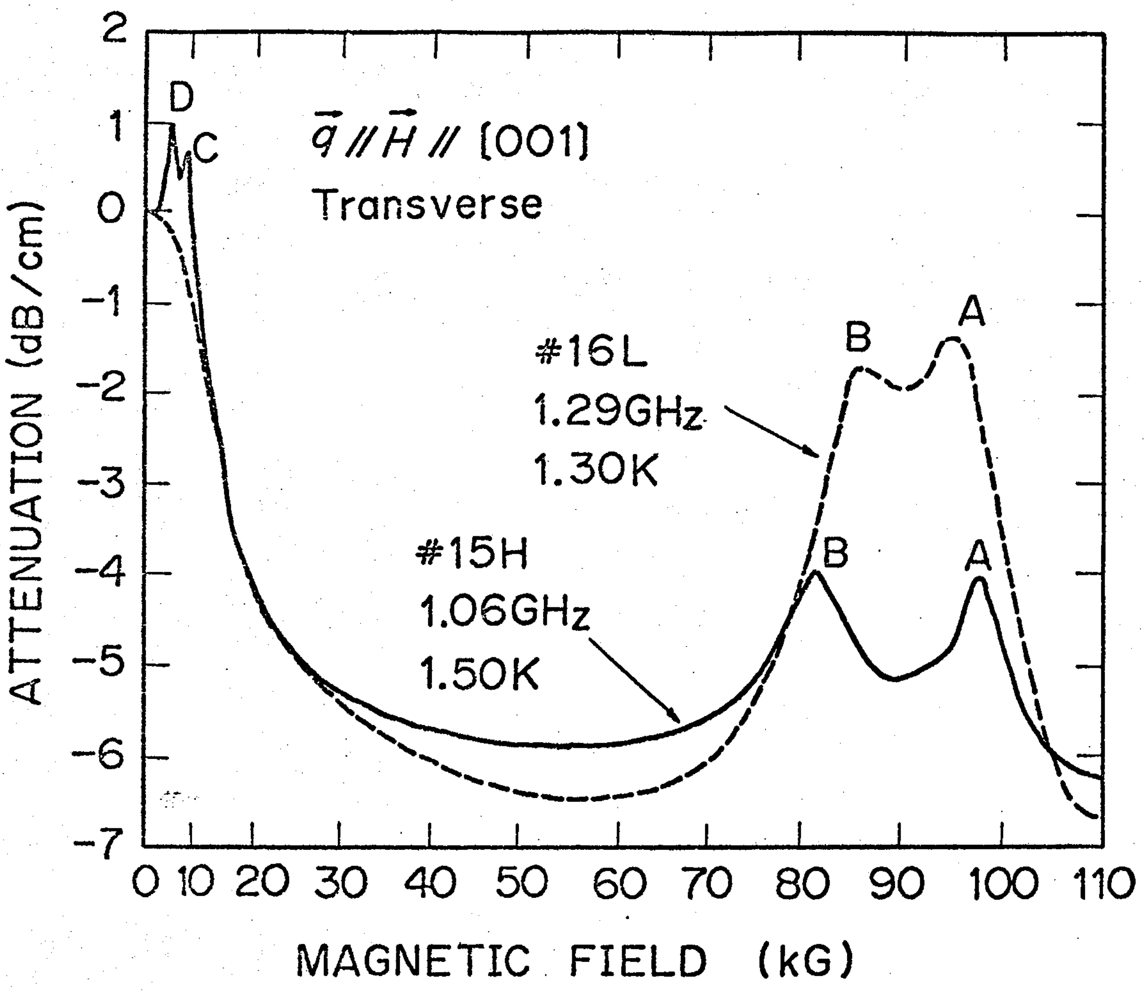

FIG. 4-6. Magnetic field dependences of the attenuation of the transverse waves propagating along the [001] direction in #15H (solid line) and #16L (broken line). The magnetic field was applied in the [001] direction. The experimental conditions are attached to the lines. The acoustic power levels were 1 and 0.1 mW/cm^2 in #15H and #16L, respectively. The peaks denoted by *A*, *B*, *C*, and *D* correspond to the peaks assigned by the same letters in Fig. 4-5.

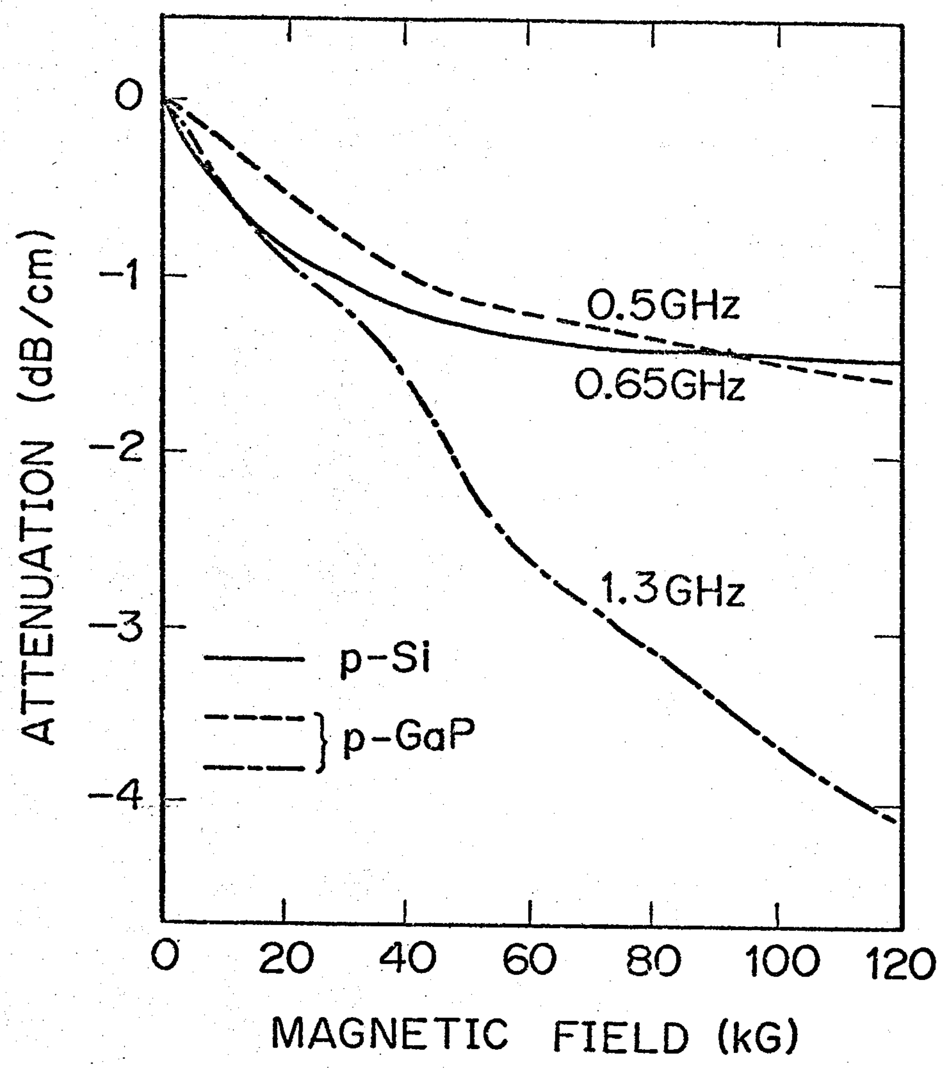

FIG. 4-7. Magnetic field dependences of the attenuation in B-doped Si (solid line) and Zn-doped GaP (broken lines) at 4.2 K. The attenuations in the absence of the magnetic field are set to 0 dB. The acoustic frequencies are attached to the lines.

dependences of the attenuation in these two samples. In B-doped Si (the sample Si16LD in Ref. 24), the attenuation of the 0.65 GHz-fast-transverse waves propagating along the [110] direction at 4.2 K under $\vec{H}$ // [110] decreases rapidly up to 40 kG and then decreases gradually up to 120 kG. In Zn-doped GaP ($\sim 1.5 \times 10^{17}$ cm^{-3}), the attenuations of both the 0.5- and the 1.3 GHz-longitudinal waves propagating along the [112] direction at 4.2 K under $\vec{H}$ // [112] decrease rather monotonically up to 120 kG. These magnetic field dependences in *p*-Si and *p*-GaP look like the background attenuation in *p*-Ge.

In later sections, we describe the MARA in Ga-doped Ge. In the present investigation, we concentrate our attention to the resonance-attenuation peaks at high magnetic fields (> 30 kG), in order to make possible to compare with the theory (Sec. V). We found that the MARA varied with both the temperature and the acoustic power reflecting the attenuation in the absence of the magnetic field (Sec. IV-A). However, it turned out that the resonance-peak positions are affected by neither the temperature nor the acoustic power. We show that the MARA changes with the acoustic frequency, the acoustic mode, the magnetic field direction, and the uniaxial stress.

2. *Acoustic power dependence*

When we changed the acoustic power, the resonance-peak attenuations were affected but the shifts in the resonance-peak positions were not observed. We measured the acoustic power dependence of the MARA in #15LB using the 1.11 GHz-fast-transverse waves propagating along the [110] direction. The magnetic field was applied in the [001] direction.

Figure 4-8 shows the effect of the acoustic power on the MARA at 1.5 K. The bottom line represents the MARA at $\sim$6 mW/cm^2 and the attenuation peaks are faint. The successive lines upwards represent the MARA obtained with decreasing the acoustic power. Numerals attached to the lines show the acoustic power levels in unit of dB; 0 dB corresponds to 6 mW/cm^2. As the acoustic power

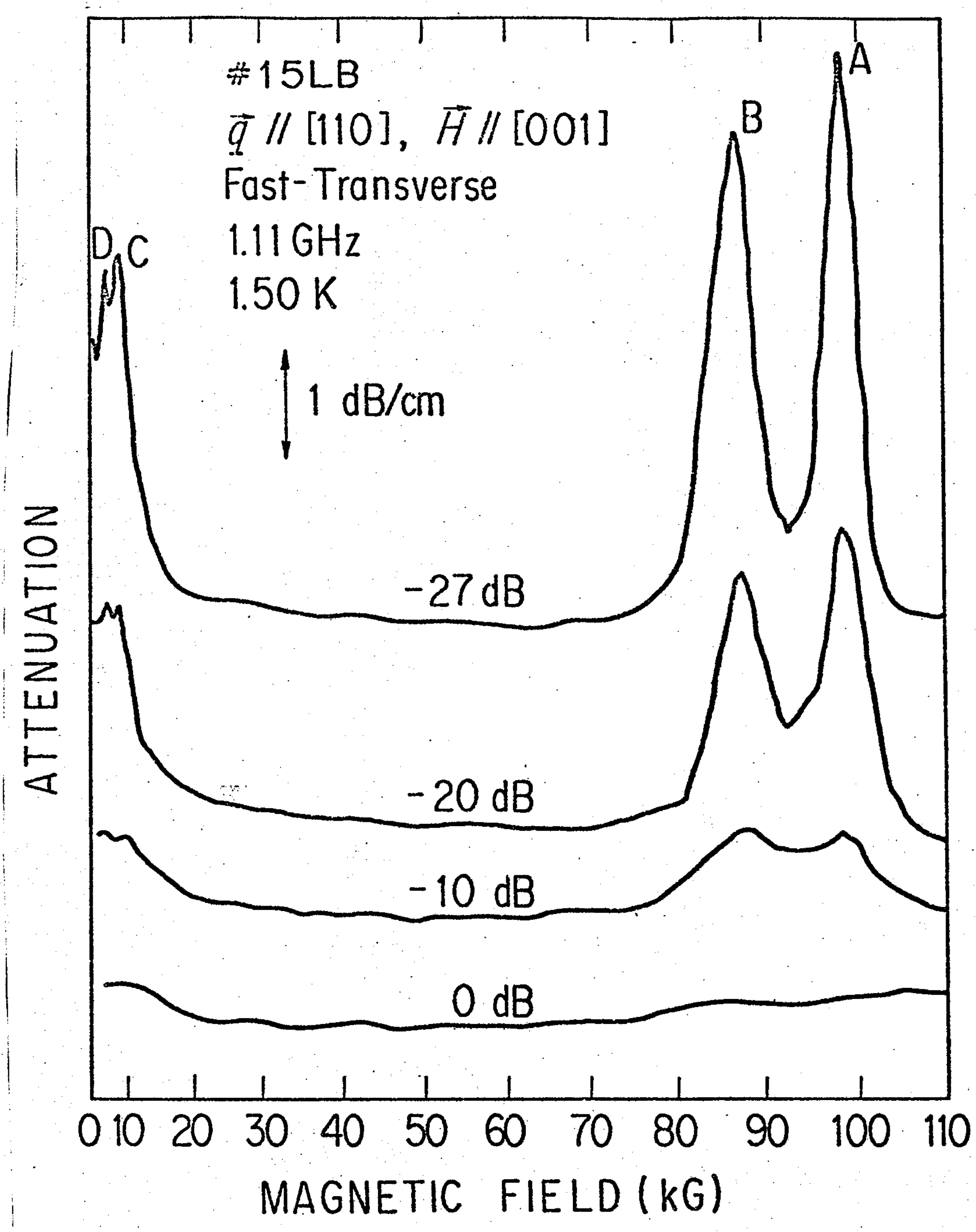

FIG. 4-8. Acoustic power dependence of the MARA of the 1.11 GHz-fast-transverse waves propagating along the [110] direction in #15LB at 1.5 K. The magnetic field was applied in the [001] direction. The scale of the ordinate is indicated by an arrow representing 1 dB/cm. Numerals attached to the lines show the acoustic power levels in unit of dB; 0 dB corresponds to 6 mW/cm^2. The peaks denoted by *A*, *B*, *C*, and *D* correspond to the peaks assigned by the same letters in Fig. 4-5.

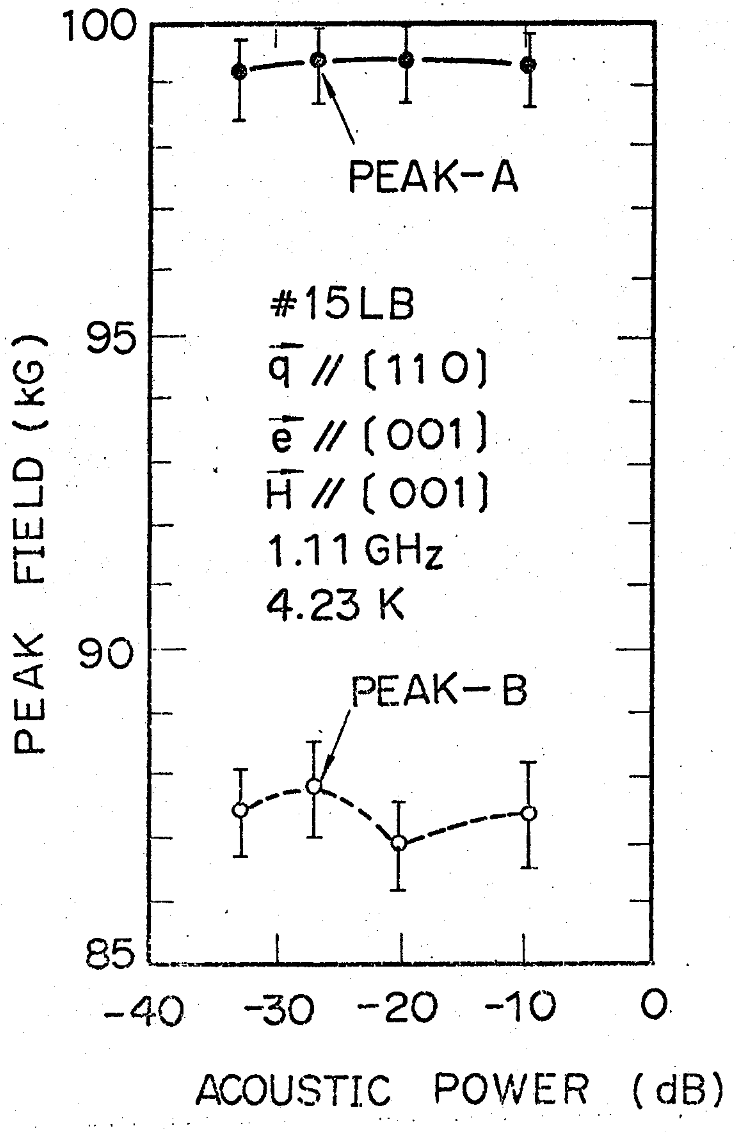

FIG. 4-10. Acoustic power dependences of the resonance-peak fields at 4.23 K for the case of Fig. 4-8. Closed and open circles denote the resonance-peak positions of the peaks *A* and *B*, respectively.

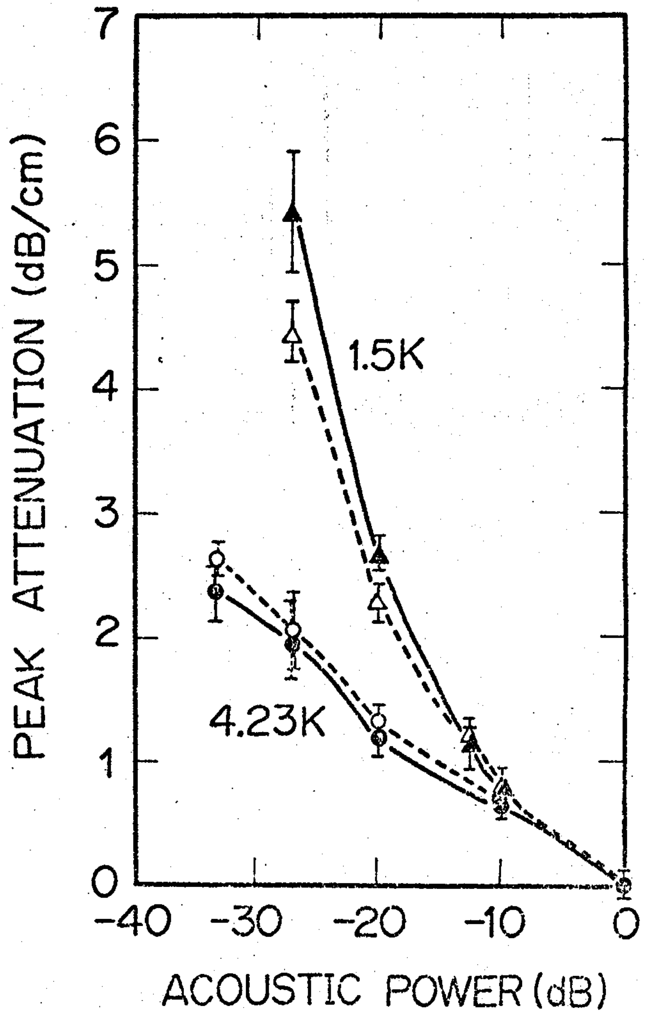

FIG. 4-9. Acoustic power dependences of the resonance-peak attenuations for the case of Fig. 4-8. Closed and open triangles denote the attenuations of the peaks *A* and *B*, respectively, at 1.5 K. Closed and open circles denote those of the peaks *A* and *B*, respectively, at 4.23 K.

was decreased, the attenuations of the peaks *A* and *B* were increased, whose feature is shown in Fig. 4-9. In this figure, we define the resonance-peak attenuations as the differences between the peak attenuations and the background attenuations. On the other hand, the resonance-peak positions did not shift appreciably with the acoustic power, whose feature is shown in Fig. 4-10. These behaviors of the acoustic power dependence of the MARA were found at any temperatures below 4.2 K or in the other samples.

The acoustic power dependence of the MARA is related to the saturation effect described in Sec. IV-A and will be discussed in Sec. V-C. In the following sections, our measurements were performed in the low acoustic power where the signal is clear enough to follow the detailed behavior. Our analysis which is related to the determination of the Zeeman-splitting parameters of the acceptor ground-state is carried out in relation to the resonance-peak positions, which are not affected appreciably by the acoustic power.

3. *Temperature dependence*

When the temperature was varied, the resonance-peak attenuations were changed appreciably but the resonance-peak positions were affected little. Figure 4-11 shows the effect of the temperature on the MARA in #15LA for the 1.23 GHz-transverse waves propagating along the [001] direction at 0.06 mW/cm^2. The magnetic field was applied in the [001] direction. The bottom line represents the MARA at 1.3 K, which is the same as the solid line in Fig. 4-5. The successive lines upwards represent the MARA obtained with increasing the temperature. As decreasing the temperature, the attenuations of the peaks *A* and *B* increased appreciably but the resonance-peak positions shifted little, whose features are shown in Figs. 4-12 and 4-13, respectively. The similar temperature dependences were found in the other samples or the other acoustic mode.

When the magnetic field was applied in the [111] direction, three peaks

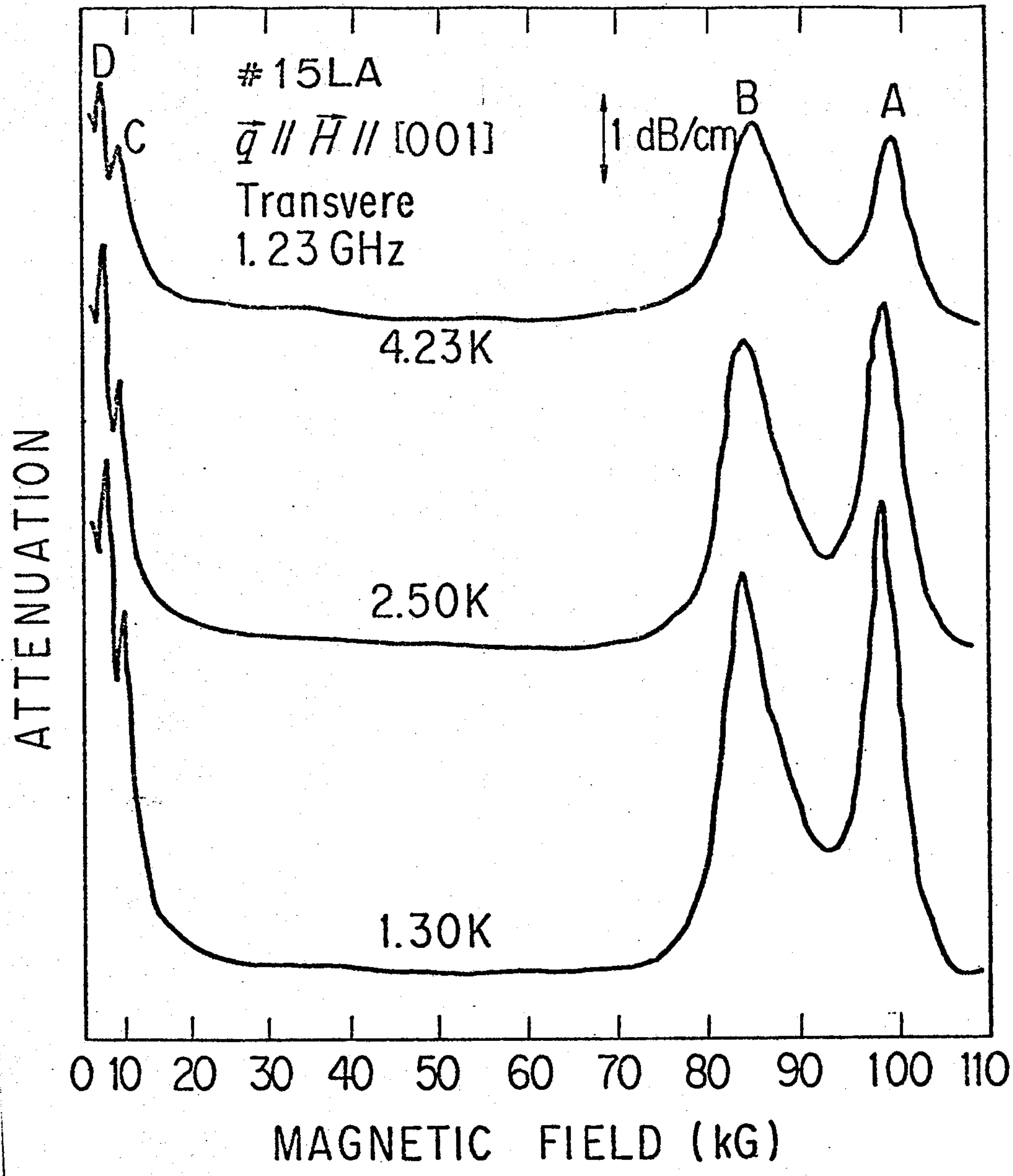

FIG. 4-11. Temperature dependence of the MARA of the 1.23 GHz-transverse waves propagating along the [001] direction in #15LA at 0.06 mW/cm^2. The magnetic field was applied in the [001] direction. The scale of the ordinate is indicated by an arrow representing 1 dB/cm. The peaks denoted by *A*, *B*, *C*, and *D* correspond to the peaks assigned by the same letters in Fig. 4-5.

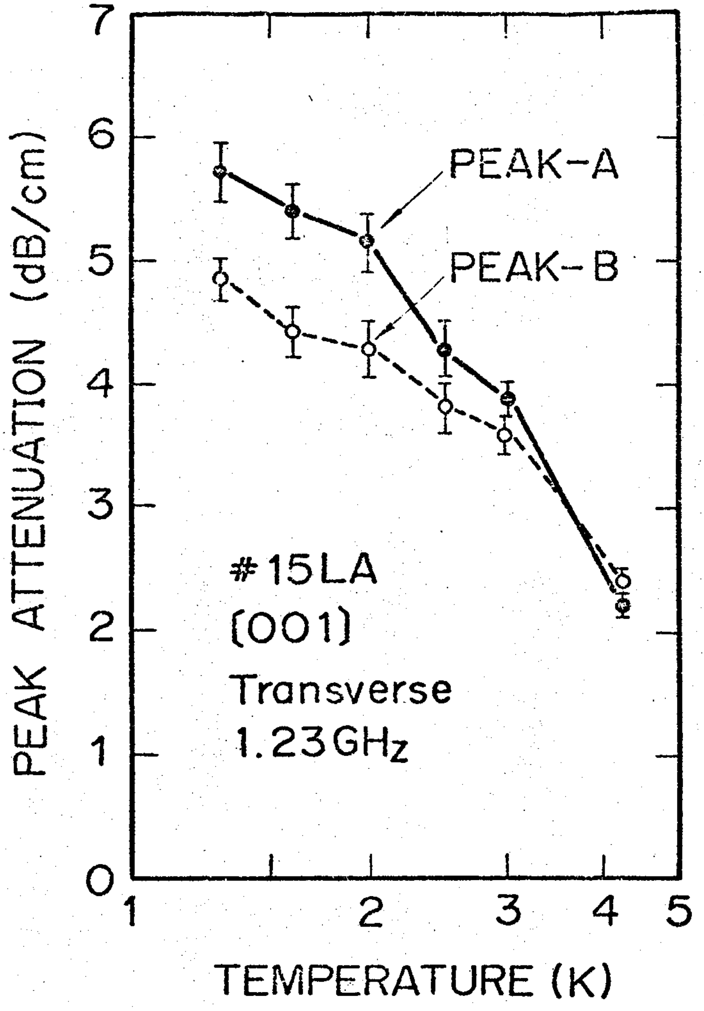

FIG. 4-12. Temperature dependences of the resonance-peak attenuations for the case of Fig. 4-11. The Miller index inserted indicates the direction of the ultrasonic wave-propagation and the magnetic field.

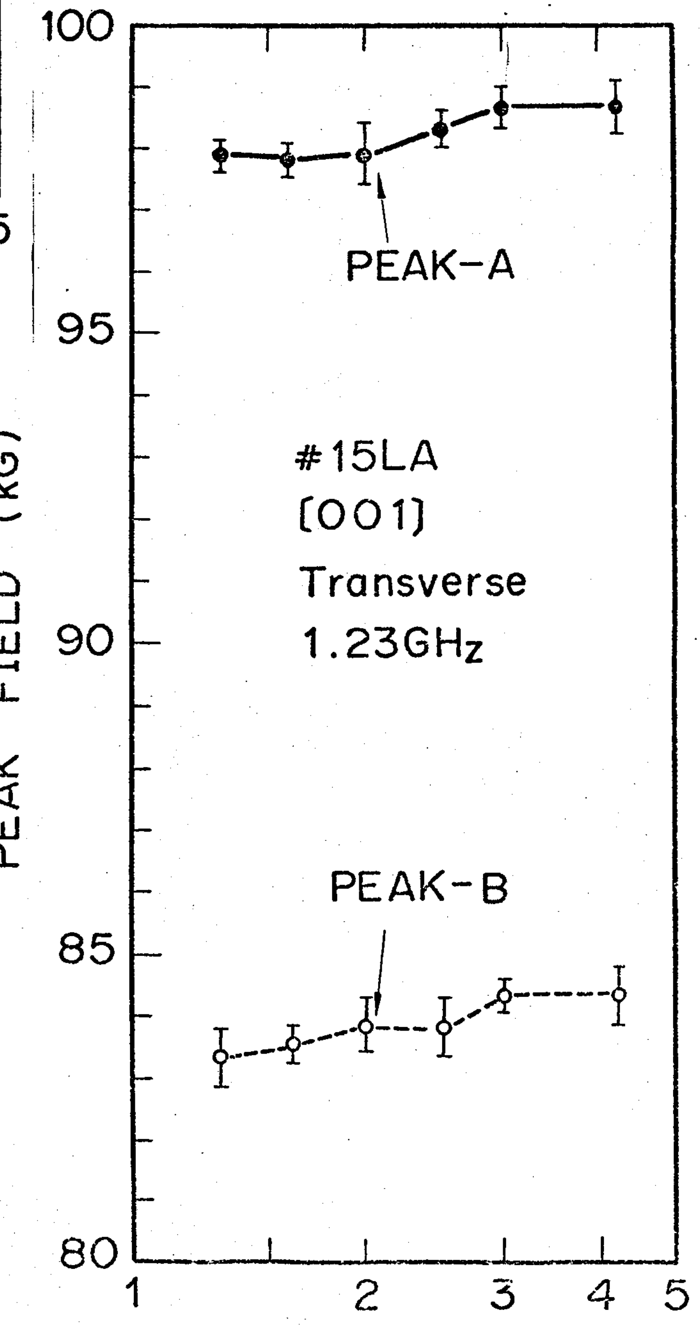

FIG. 4-13. Temperature dependence of the resonance-peak fields for the case of Fig. 4-11. The Miller index inserted indicates the direction of the ultrasonic wave-propagation and the magnetic field.

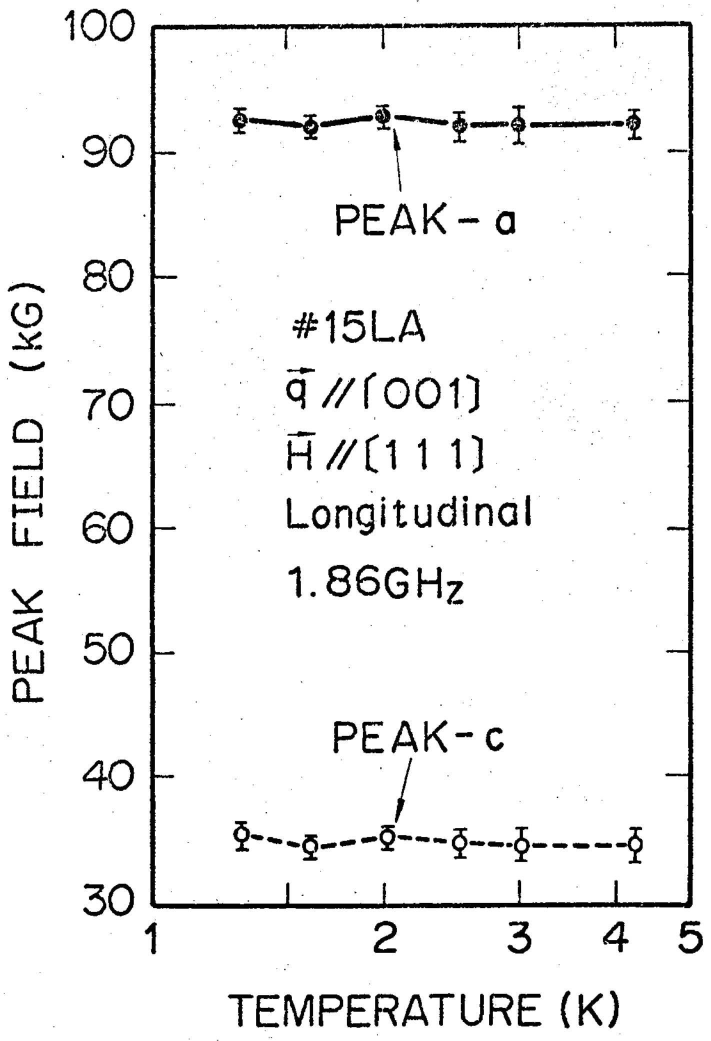

FIG. 4-15. Temperature dependences of the resonance-peak fields for the case of Fig. 4-14.

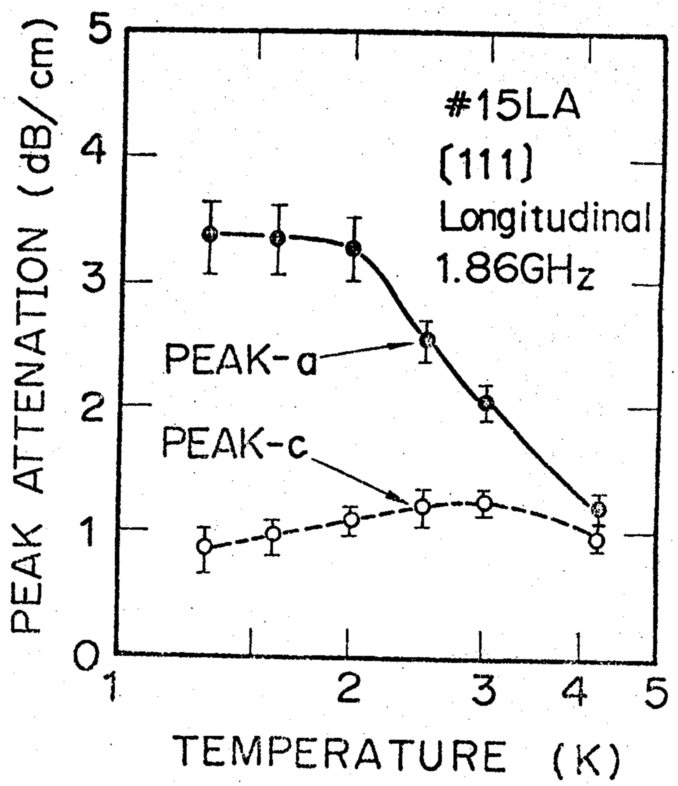

FIG. 4-14. Temperature dependences of the resonance-peak attenuations of the 1.86 GHz-longitudinal waves propagating along the [001] direction in #15LA at 0.06 mW/cm^2. The Miller index inserted indicates the direction of the magnetic field.

(assigned by *a*, *b*, and *c* in Fig.4-5) were found above 30 kG. Since the peak *b* was, however, not clear enough to follow the temperature dependence, we disregarded this peak in this case. The temperature dependences of the resonance-peak attenuations and positions in #15LA for the 1.86 GHz-longitudinal waves propagating along the [001] direction are shown in Figs. 4-14 and 4-15, respectively. The attenuation of the peak *a* increased with decreasing the temperature down to 2 K and saturated below 2 K. The attenuation of the peak *c* saturated over whole temperatures between 1.3 and 4.2 K. The saturation effect will be discussed in Sec. V-C.

4. *Acoustic frequency dependence*

When the acoustic frequency was changed, the resonance-peak positions were shifted. Figure 4-16 shows the acoustic frequency dependence of the MARA of the fast-transverse waves propagating along the [110] direction at 1.5 K under $\vec{H}$ // [001] in #15LB. The successive lines downwards represent the MARA obtained with decreasing the acoustic frequency. As decreasing the frequency, the resonance-peak positions shifted appreciably; the peak *A* shifted toward the lower magnetic field and the peak *B* shifted toward the higher magnetic field with decreasing the frequency. At 0.58 GHz, two resonance peaks could not be observed separately. Below 0.30 GHz, we could observe one peak at the high magnetic field.

The feature of the resonance-peak shifts with the acoustic frequency is shown in Fig. 4-17 for the above case. The peak *A* almost linearly shifts toward the lower magnetic field, whereas the peak *B* toward the higher magnetic field with decreasing the frequency. Consequently, these two peaks approach each other with decreasing the frequency and overlap near 92 kG.

When the magnetic field was applied in the [111] direction, the observed acoustic frequency dependence of the resonance-peak positions in #15LA is shown in Fig. 4-18. The measurements were carried out at 1.3 K by using both

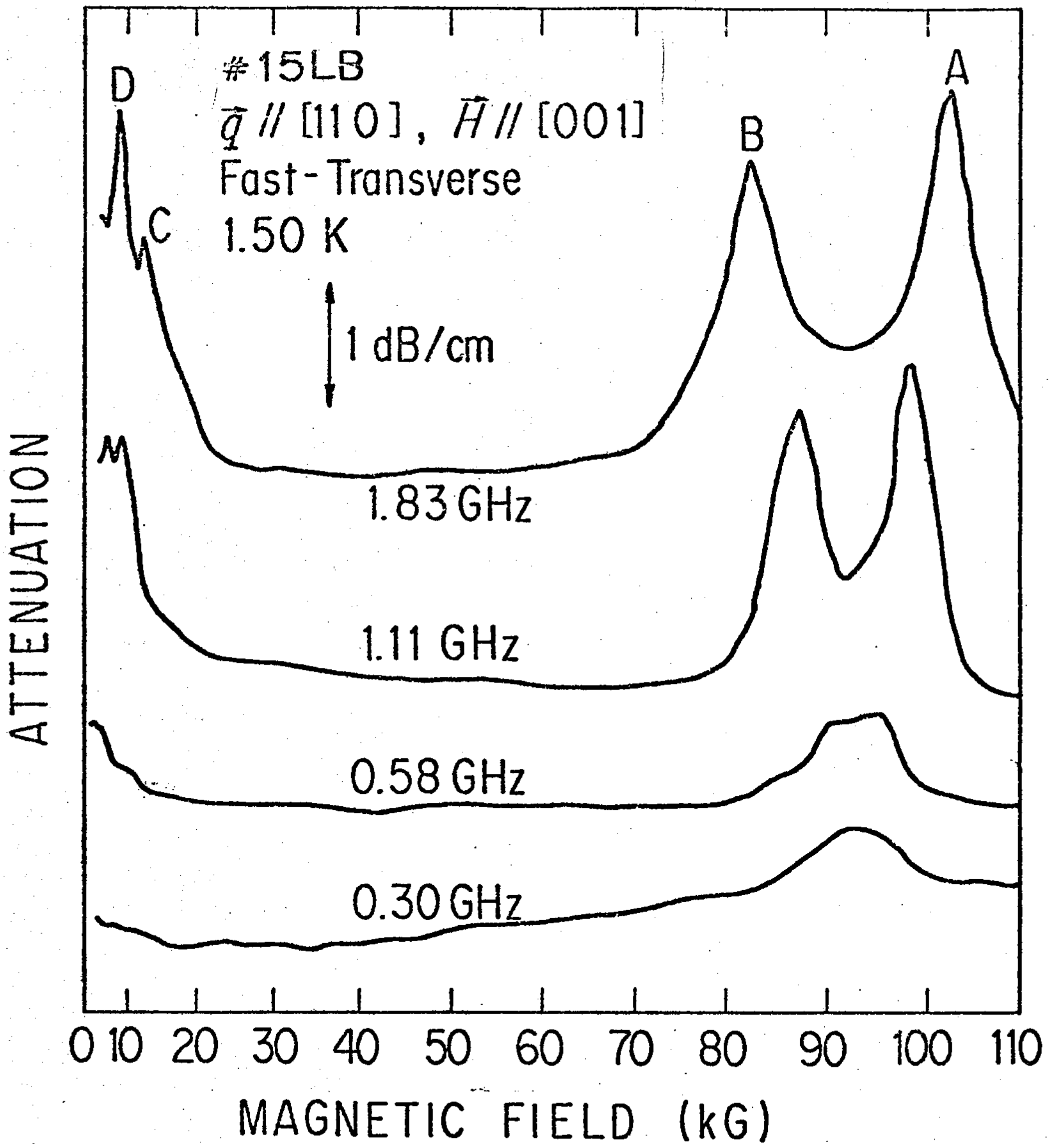

FIG. 4-16. Acoustic frequency dependence of the MARA of the fast-transverse waves propagating along the [110] direction in #15LB at 1.5 K under $\vec{H}$ // [001]. The scale of the ordinate is indicated by an arrow representing 1 dB/cm. The acoustic power levels are not the same for all cases. The peaks denoted by *A*, *B*, *C*, and *D* correspond to the peaks assigned by the same letters in Fig. 4-5.

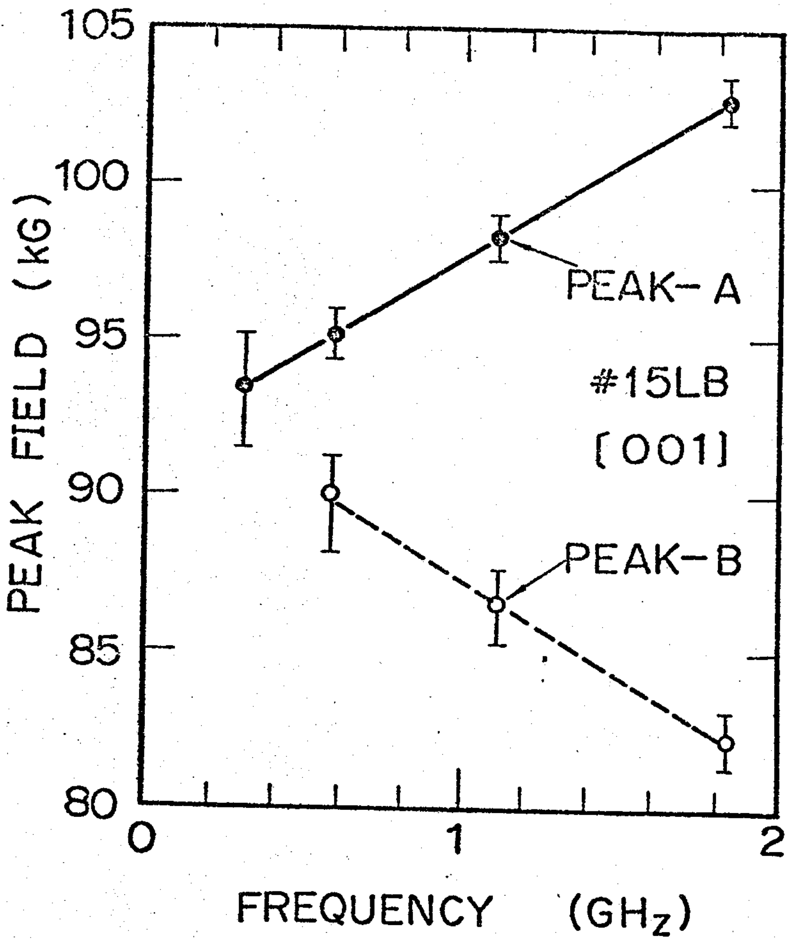

FIG. 4-17. Acoustic frequency dependences of the resonance-peak fields for the case of Fig. 4-16. The Miller index inserted indicates the direction of the magnetic field.

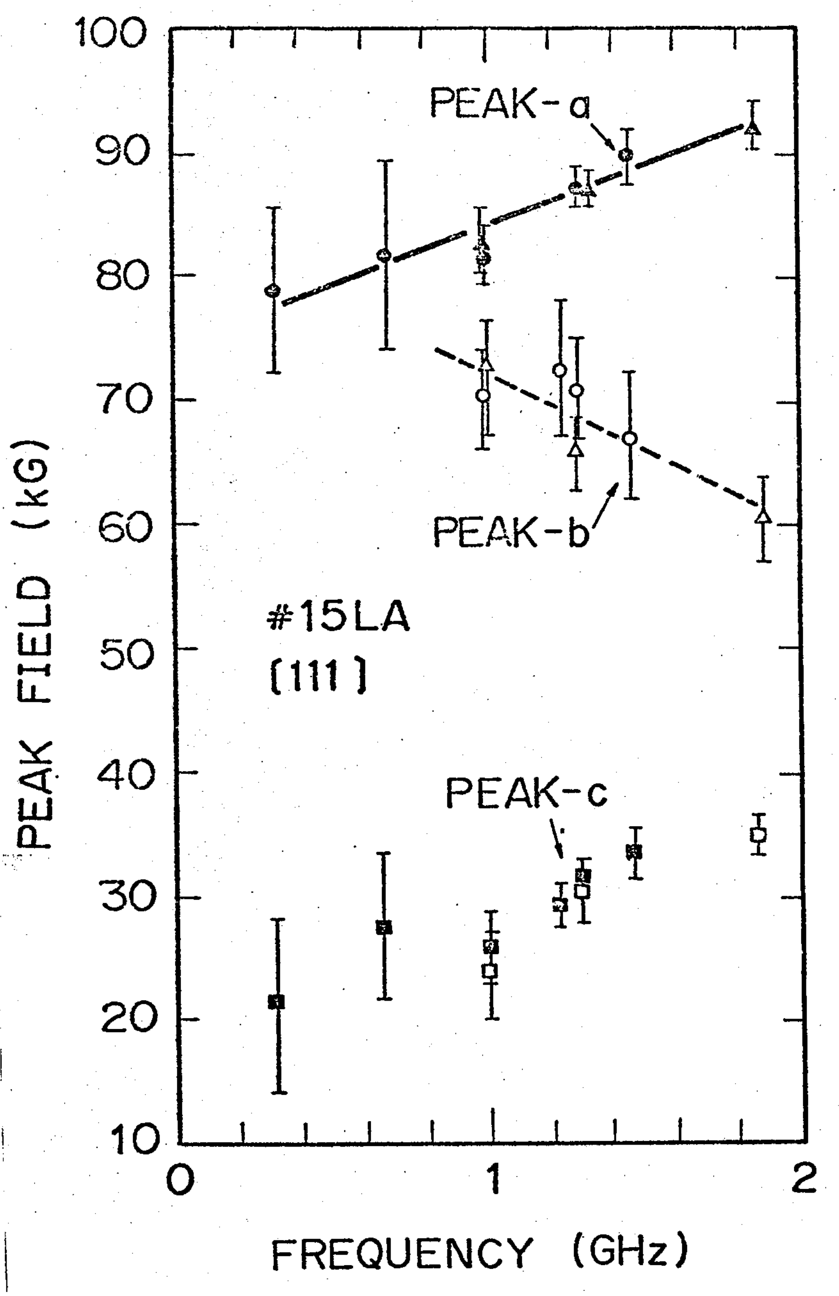

FIG. 4-18. Acoustic frequency dependences of the resonance-peak fields of the ultrasonic waves propagating along the [001] direction in #15LA at 1.3 K. Circles and triangles denote the peak fields for the transverse and the longitudinal waves, respectively. The Miller index indicates the direction of the magnetic field.

the transverse and the longitudinal waves propagating along the [001] direction. The peak *a* shifts almost linearly toward the lower magnetic field, whereas the peak *b* toward the higher magnetic field with decreasing the acoustic frequency. Consequently, these two peaks approach each other with decreasing the frequency and overlap near 75 kG. In this figure, the frequency dependence of the peak *c* is shown.

The overall behaviors of the acoustic frequency dependence in #15H and #16L are similar to the above cases. We do not show the acoustic frequency dependence of the resonance-peak attenuations, since we could not observe the attenuation by controlling the degree of the saturation.

5. Acoustic mode dependence

The MARA changes with the acoustic mode and the direction of the ultrasonic waves in both the magnitude and the peak positions. This reflects the difference in the coupling parameters or the selection rules.

Figure 4-19 shows the MARA of the 1.86 GHz-longitudinal waves propagating along the [001] direction at 1.3 K and 0.1 mW/cm^2 in #15LA. The magnetic field was applied in the [001] direction. This corresponds to that of the transverse waves shown by the solid line in Fig. 4-5. The effect of the magnetic field on the attenuation of the longitudinal waves is smaller than that of the transverse waves reflecting the fast propagation of the former waves. In addition to this difference in magnitude, we observe an extra attenuation increment near 40 kG for the case of the longitudinal waves.

Figure 4-20 shows the MARA of the 1.83 GHz-fast-transverse waves and of 1.84 GHz-longitudinal waves propagating along the [110] direction at 1.5 K and 0.06 mW/cm^2 in #15LB. For the transverse waves, the MARA consists of four peaks whose feature was quite similar to the solid line in Fig. 4-5. On the other hand, for the longitudinal waves, the feature of the MARA is quite different from that of the transverse waves; the peak *A* and *B* were not

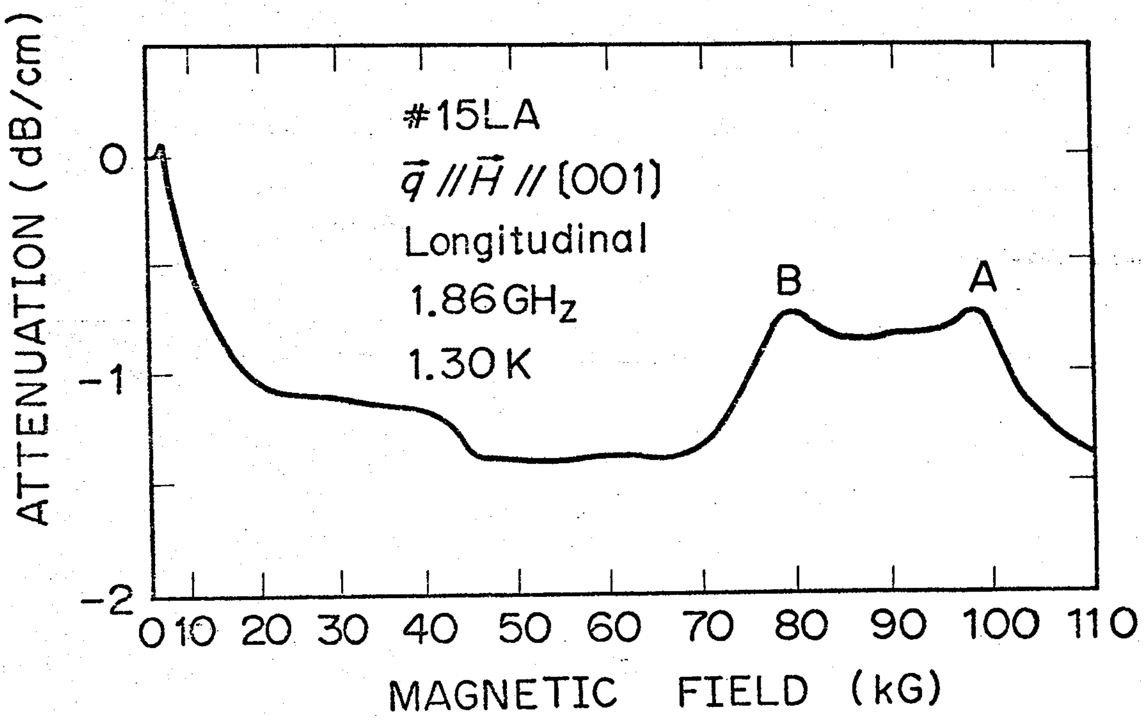

FIG. 4-19. Magnetic field dependence of the attenuation of the 1.86 GHz-longitudinal waves propagating along the [001] direction in #15LA at 1.3 K and at 0.1 mW/cm^2. The magnetic field was applied in the [001] direction. The peaks denoted by *A* and *B* correspond to the peaks assigned by the same letters in Fig. 4-5.

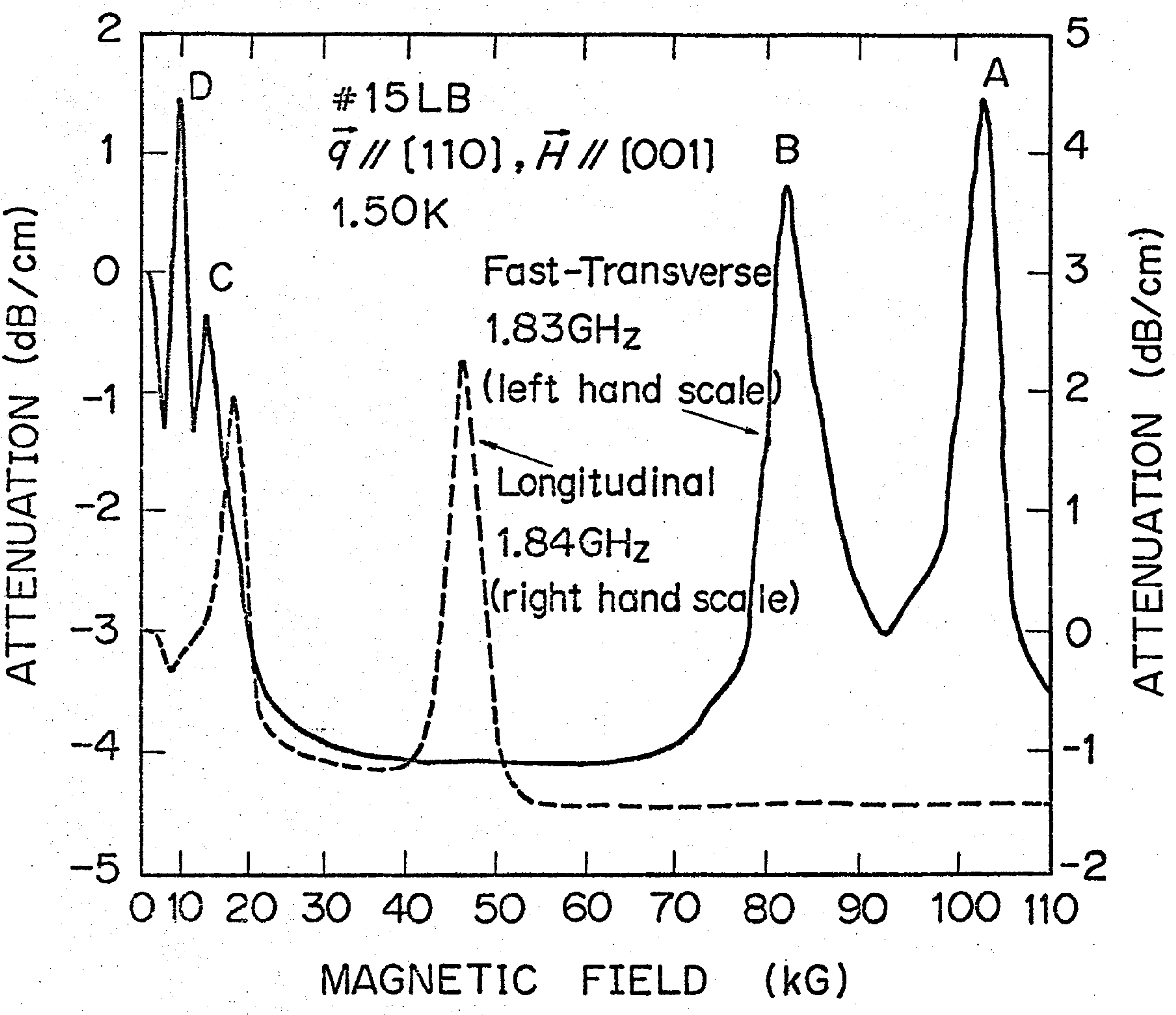

FIG. 4-20. Magnetic field dependences of the attenuations of both the 1.83 GHz-fast-transverse waves (solid line) and the 1.84 GHz-longitudinal waves (broken line) propagating along the [110] direction in #15LB at 1.5 K and at 0.06 mW/cm^2. The magnetic field was applied in the [001] direction. The peaks denoted by *A*, *B*, *C*, and *D* correspond to the peaks assigned by the same letters in Fig. 4-5.

observed, but two clear resonance peaks were found near 18 and 46 kG.

6. *Magnetic field-direction dependence*

When the sample was rotated so that the magnetic field direction rotated from the [001] to the [111] direction in the $(1\bar{1}0)$ plane, we found the shifts of the resonance-peak positions. We measured the magnetic field-direction dependence of the MARA in #15LA using the 1.23 GHz-transverse waves and the 1.84 GHz-longitudinal waves propagating along the [001] direction.

Figure 4-21 shows the MARA of the transverse waves at several magnetic field directions. The [001] and the [111] directions correspond to 0° and 54.7°, respectively. Thus, the resonance peaks A, B, C, and D for 0° and the peaks a, b, c, and d for 54.7° were observed in accordance with Fig. 4-5. The successive lines downwards from the line for 0° represent the MARA obtained with increasing θ, which is an angle from the [001] direction. The resonance-peak positions were strongly affected by the magnetic field direction.

In Figs. 4-22 and 4-23 are shown the magnetic field-direction dependences of the resonance-peak positions observed for the transverse and the longitudinal waves, respectively. These two figures are quite similar to each other. When the magnetic field was set in the [001] direction, four peaks A, B, C, and D were found. The peaks A and B shift toward the higher magnetic fields with increasing θ slightly. When $\theta > 10°$, these peaks could not be found in the magnetic field up to 120 kG. Following the disappearence of the high magnetic field peaks, two peaks were found at the low magnetic fields (near 20 and 40 kG). The low-field peaks did not shift appreciably as θ increased from 10° to 40°. When $40° < \theta < 70°$, the low-field peaks shifted toward the higher magnetic fields making the maximum near 55°. At 54.7°, the peak at 40 kG will be connected to the peaks a or b and the peak at 20 kG to the peak c.

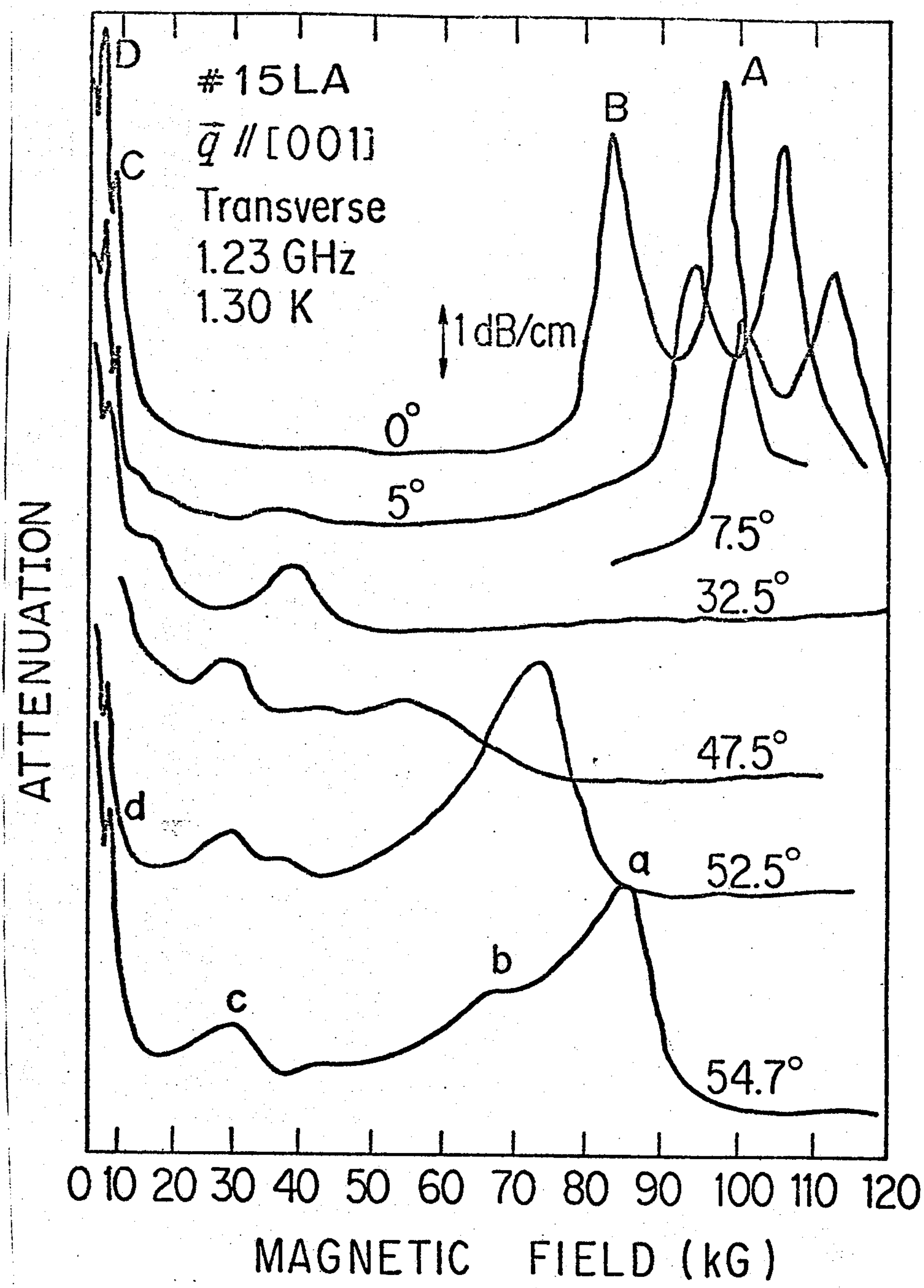

FIG. 4-21. Magnetic field-direction dependence of the MARA of the 1.23 GHz-transverse waves propagating along the [001] direction in #15LA at 1.3 K. Numerals attached to the lines denote angles in unit of degrees between the [001] direction and the magnetic field in the $(1\bar{1}0)$ plane. The acoustic power levels are not the same for all cases. The peaks denoted by A, B, C, and D at 0°, and by a, b, c, and d at 54.7° correspond to the peaks assigned by the same letters in Fig. 4-5.

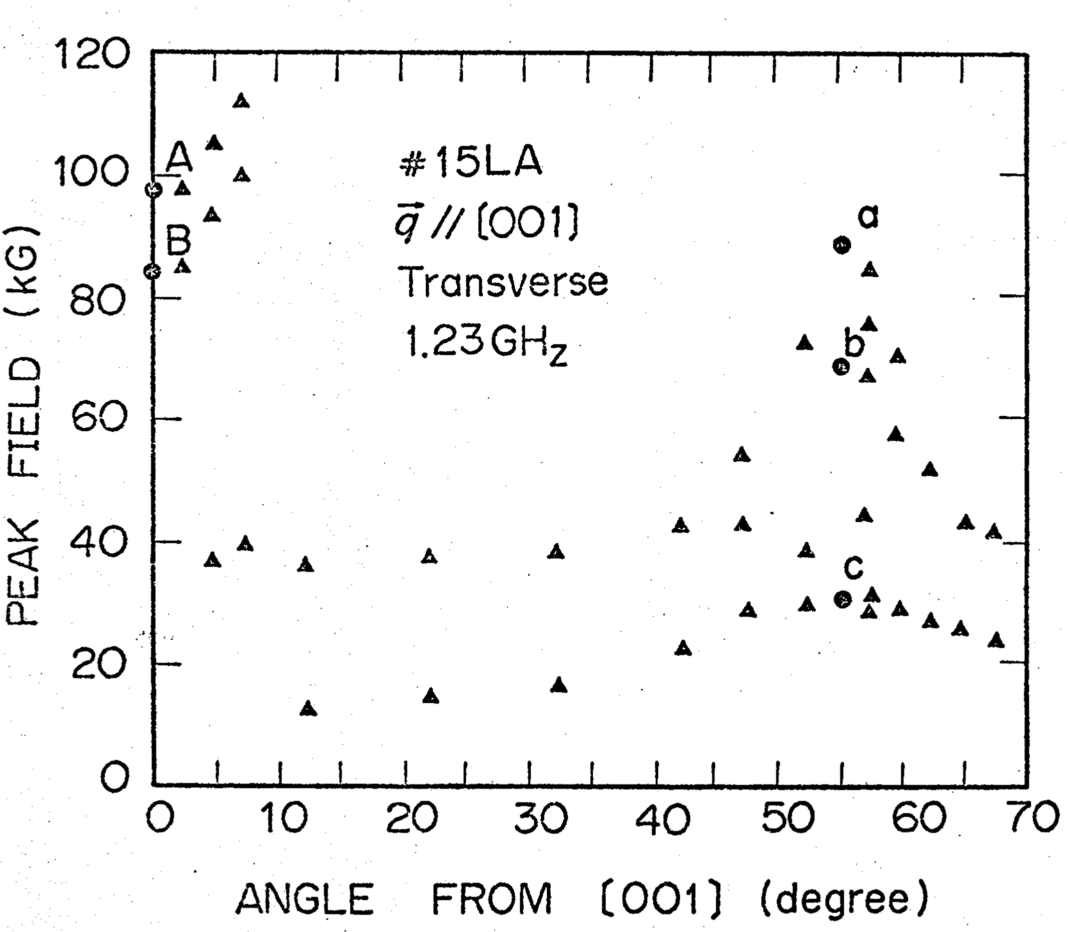

FIG. 4-22. Magnetic field-direction dependence of the resonance-peak fields for the case of Fig. 4-21. Circles denoted by *A* and *B* at 0° and *a*, *b*, and *c* at 54.7° correspond to the peaks assigned by the same letters in Fig. 4-5. Triangles denote the peak positions at the other angles.

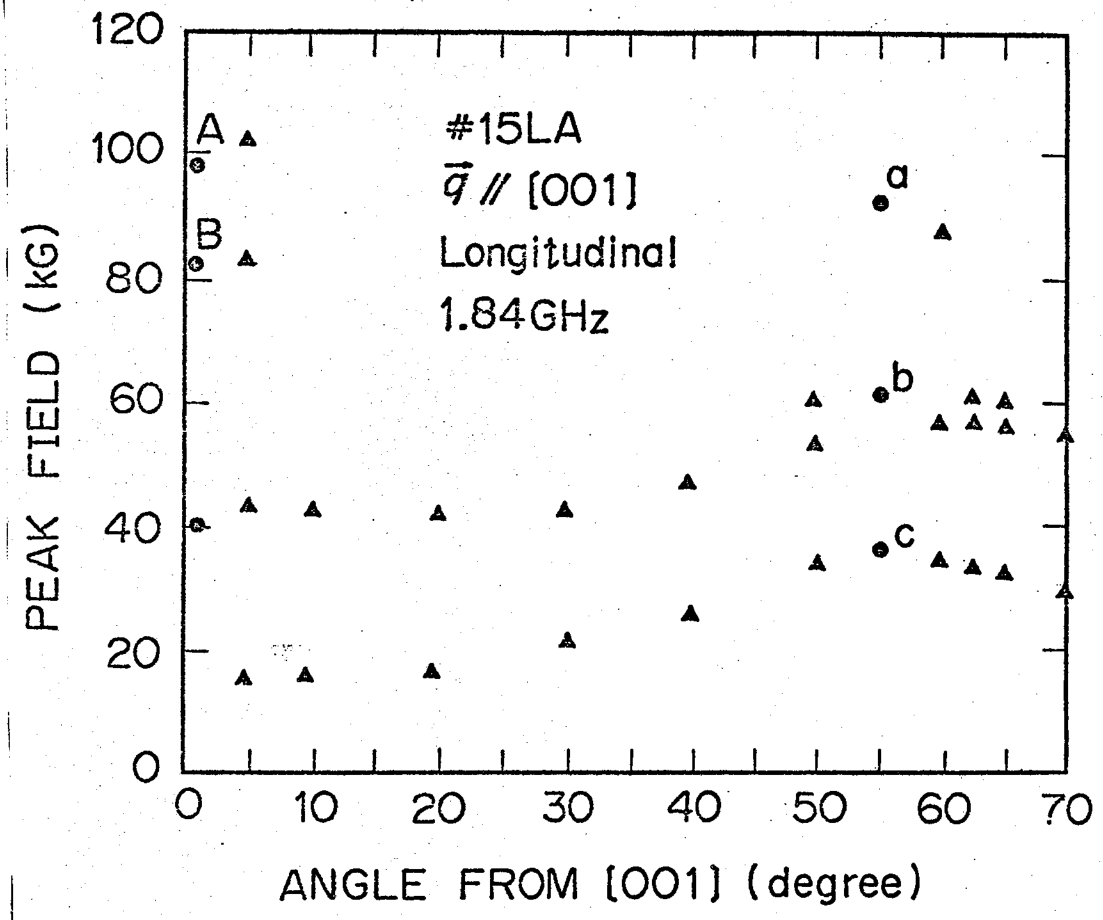

FIG. 4-23. Magnetic field-direction dependence of the resonance-peak fields of the 1.84 GHz-longitudinal waves propagating along the [001] direction in #15LA at 1.3 K. Circles denoted by *A* and *B* at 0° and by *a*, *b*, and *c* correspond to the peaks assigned by the same letters in Fig. 4-5. Triangles denote the peak positions at the other angles.

7. Uniaxial stress dependence

When the uniaxial stress was applied, the shifts of the resonance-peak positions were observed at rather weak stress.[52] The sample #15LC was prepared for this experiment so that the compressional uniaxial stress and the magnetic field were applied in the [001] direction. The 1.11 GHz-fast-transverse waves were propagated along the [110] direction at 4.2 K.

Figure 4-24 shows the effect of the uniaxial stress on the MARA. The top line represents the MARA in the absence of the stress. The successive lines downwards represent the MARA obtained with increasing the stress. Since we used the stress apparatus described in Sec. II-F, the stress had a large error due to the friction for the translational motion of the rod (G) etc. Typical error was $\pm 1.0 \times 10^7$ dyns/cm^2 at 1.4×10^7 dyns/cm^2: The error was estimated by increasing and decreasing the stress as monitoring the MARA. As increasing the stress, the peaks *A* and *B* shift toward the lower magnetic fields and the peaks *C* and *D* toward the higher magnetic fields. At $\sim 1.8 \times 10^7$ dyns/cm^2, the peaks overlap near 45 kG. Above 2.4×10^7 dyns/cm^2, we could observe no peaks in the magnetic field up to 120 kG.

It should be noted that the MARA is strongly affected by the stress at rather weak level. This means that, in order to get the intrinsic attenuations, we must have paid attention to avoid giving external stresses except for the experiment of the uniaxial stress dependence.

8. Acceptor-concentration dependence

The resonance-peak positions were not affected by the acceptor concentration remarkably in the adopted samples, when the acoustic mode and the magnetic field direction were the same. The MARA obtained in three samples with different concentrations by using the transverse waves propagating along the [001] direction under $\vec{H}$ // [001] are shown in Figs. 4-5 and 4-6. The resonance-peak positions did not shift appreciably but the resonance-peak widths were broadened

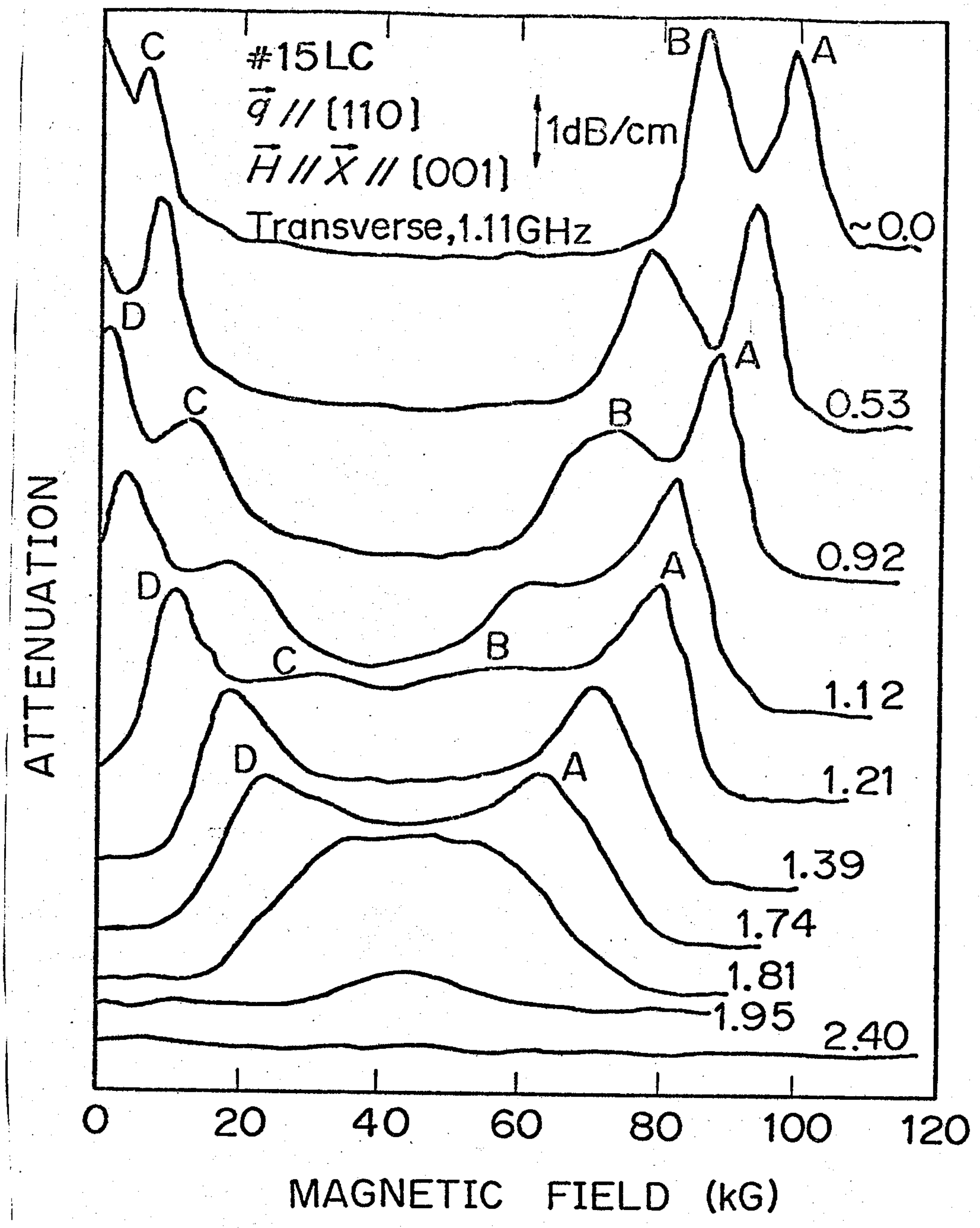

FIG. 4-24. Uniaxial stress dependence of the MARA of the 1.11 GHz-fast-transverse waves propagating along the [110] direction in #15LC at 4.2 K and at 0.06 mW/cm^2. Both the magnetic field and the uniaxial stress were applied in the [001] direction. Numerals attached to the lines denote the magnitudes of the uniaxial stress in unit of 10^7 dynes/cm^2. The scale of the ordinate is indicated by an arrow representing 1 dB/cm. The peaks denoted by *A*, *B*, *C*, and *D* correspond to the peaks assigned by the same letters in Fig. 4-5.

with increasing the acceptor concentration. The peaks *A* and *B* became obscure with increasing the acceptor concentration. The peaks *C* and *D* became faint and disappeared with increasing the concentration. Since the degrees of the saturation effect are not the same for the three cases, we cannot compare the magnitude of the resonance-peak attenuations.

V. ANALYSES OF EXPERIMENTAL RESULTS

A. Temperature dependence of the attenuation in the absence of the magnetic field

As described in Sec. II-C, we can regard the gallium impurities in our samples as isolated in the first-order approximation. Therefore, we analyze our experimental results in the light of the theory described in Sec. III. In this section, we consider the temperature dependence of the attenuation in the absence of the magnetic field.

The formulas for the ultrasonic attenuation in the absence of the magnetic field are given by Eqs. (3.37) - (3.42). Two types of attenuations exist: the relaxation-type α_1 and the resonance-type α_2.

To calculate the coupling of the ultrasonic waves with the acceptor holes, we use the deformation-potential constants obtained by piezospectroscopy.[53] On the other hand, in the calculation of the level width Γ_n, we adopt the "dynamic" deformation-potential constants determined by the heat-pulse experiment[28] by the following facts: (1) The analysis of the heat-pulse data stands basically on the same principle adopted here. (2) Γ_n is determined by the phonons which are in the same frequency range as the phonons contained in the heat pulse. These phonons have the wavelength $1/q$ (q is the wave number of the phonon), which is smaller than the effective Bohr radius a^* of the acceptor holes. (3) The third reason will be described later in this section. Moreover, since it is assumed in the derivation of the ultrasonic attenuation formulas in Sec. III-C that the envelope functions consist of solely s-like parts, the deformation-potential constants for the acceptors become equal to those for the valence-band edge according to Eqs. (3.16) and (3.18). Thus, we use the deformation-potential constants of $D_u{}^a = 5.45$ eV and $D_{u'}{}^a = 6.10$ eV[54] for Γ_n, whereas $D_u{}^a = 3.32$ eV and $D_{u'}{}^a = 3.81$ eV[53,55] for the coupling of the ultrasonic waves with the acceptor holes.

First, we calculate the temperature dependence of the level width Γ_n in the absence of the magnetic field. Figure 5-1 shows the calculated temperature dependences of Γ_R and Γ_n^d (n = 1, 2), where we assume that the splitting is uniform throughout the sample. The splitting Δ is expressed in unit of degrees of Kelvin. Other constants used are given in Table 5-1. For Δ = -0.02 K, which is determined by the analysis of the MARA as described in Sec. V-B, Γ_n^d are smaller than those for Δ = -0.1 K by one or more orders at any temperatures. Thus, the contribution of Γ_n^d to the level width is negligibly small and that of Γ_R dominates.

Now we calculate the temperature dependence of the attenuation of the 1.11 GHz-fast-transverse waves propagating along the [110] direction in #15LB. In Fig. 5-2 is shown the calculated temperature dependence of the attenuation, where we assume that the scaling factors $\beta_1 = \beta_2 = 1$ and the Gaussian distribution for the initial splittings with Δ_0 = -0.02 K and σ = 0.03 K, whose values are determined by the line shapes of the MARA as described in Sec. V-B. Inserted figure shows the relaxation attenuation α_1. The calculated attenuation indicates that the attenuation below 4.2 K, where the MARA was observed, is ascribed to the resonance attenuation α_2: The resonance attenuation is caused by the hole transitions between the split levels due to the internal stresses.

The slight increment near 7.3 K is ascribed to the relaxation attenuation, which is independent on the acoustic power. This is explained as follows. Γ_R near 12 K becomes equal to the energy corresponding to 1.11 GHz ultrasonic waves as shown by an arrow in Fig. 5-1 and then the Lorentzian has a maximum value. Since the relaxation attenuation α_1 includes the terms N_1, N_2, and $1/T$, in addition to the Lorentzian, the resultant temperature dependence has the maximum near 7.3 K. This is consistent with the observations.

At this stage, we consider about the third reason for the use of the "dynamic" deformation-potential constants in the calculation of Γ_n. If we take the values D_u^a = 3.32 eV and $D_{u'}^a$ = 3.81 eV, the slight increment near

Table 5-1. Values of physical parameters used in the calculations.

Symbol	Numerical values	Dimension
ρ	5.32	g/cm^3
κ	16	———
$v_1[001]$[a]	4.92×10^5	cm/sec
$v_2[001]$[a]	3.55×10^5	cm/sec
$v_1[110]$[a]	5.41×10^5	cm/sec
$v_2[110]$[a]	3.55×10^5	cm/sec
v_L	5.37×10^5	cm/sec
v_T	3.28×10^5	cm/sec
$S_{11} - S_{12}$	1.20×10^{-12}	cm^2/dyne
a^*	37.8	Å
m^*	$0.2\ m_0$[b]	grams
m_0	9.1×10^{-28}	grams
$D_u{}^a$	3.32	eV
$D_{u'}{}^a$	3.81	eV
$D_u{}^a$[dynamic][c]	5.45	eV
$D_{u'}{}^a$[dynamic][c]	6.10	eV

[a] The Miller indices denote the propagation direction.

[b] The effective mass m^* is calculated from the ionization energy ($\simeq 10.97$)[59] in the effective mass theory.[60]

[c] The meaning of "dynamic" is discussed in Sec. V-A in the text.

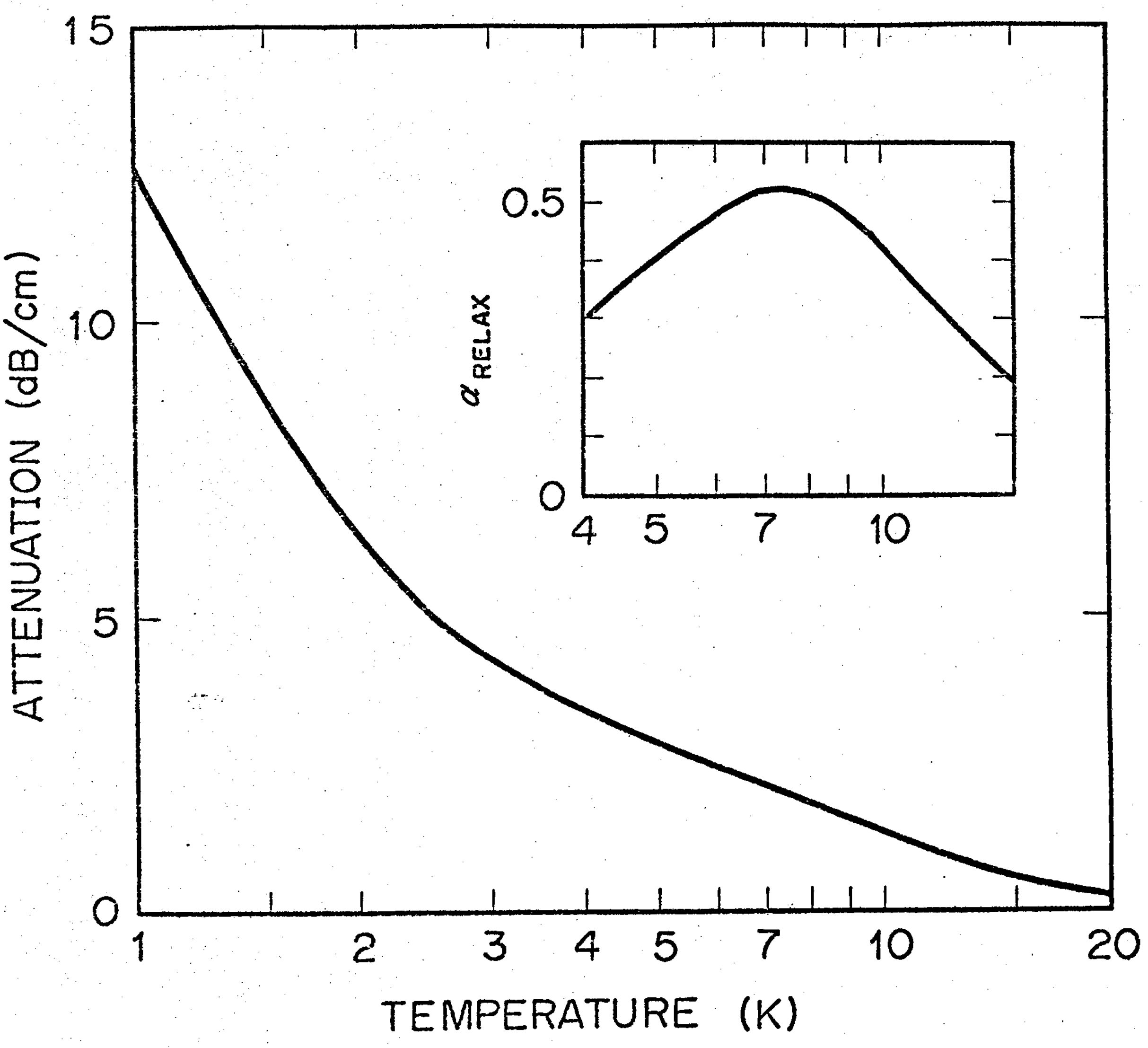

FIG. 5-2. Calculated temperature dependence of the attenuation of the 1.11 GHz-fast-transverse waves propagating along the [110] direction in #15LB. Inset shows the relaxation attenuation in the temperature range 4 to 15 K.

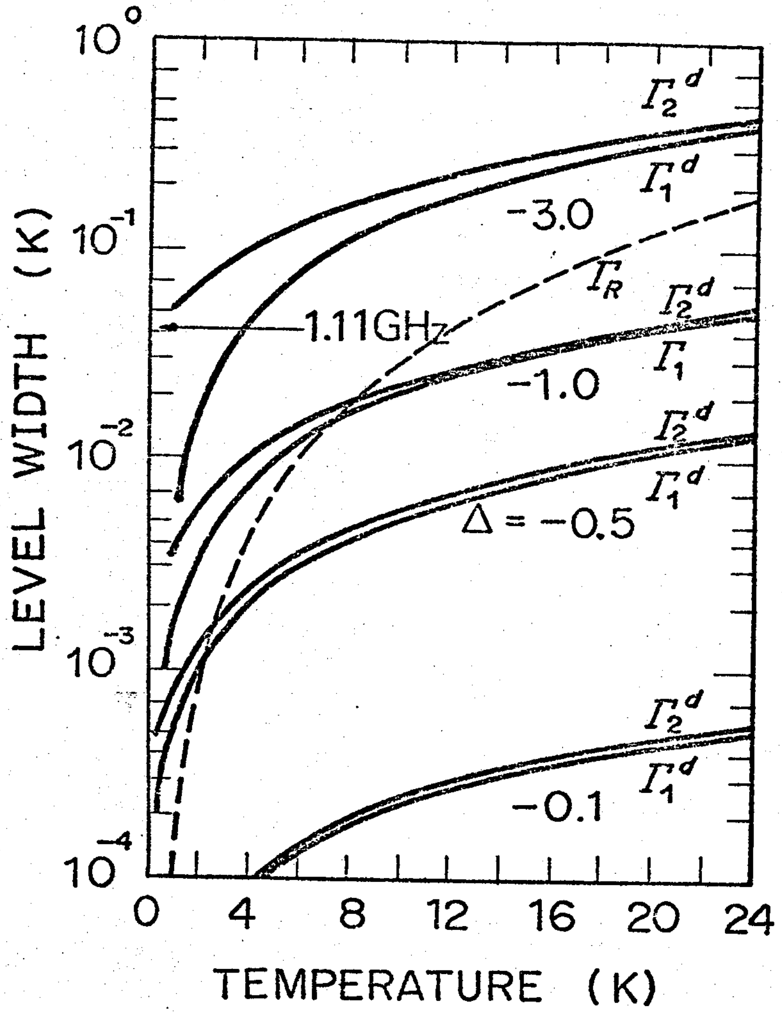

FIG. 5-1. Calculated temperature dependences of the level widths Γ_R and Γ_n^d (n = 1, 2) as a function of the uniform splitting Δ. The value of Δ is represented in unit of degrees Kelvin. An arrow mark denotes the temperature corresponding to 1.11 GHz.

7.3 K is shifted toward ∿20 K. This is inconsistent with the observations.

The calculated temperature dependence is similar to the observations in the weak acoustic power limit except for the scaling factors. In order to get the better fitting of the calculated with the observations, we must take account of the saturation effect. The saturation effect may be taken into account by adjusting a scaling factor β_2 in the present formulas. As the acoustic power increases, the saturation effect becomes strong and β_2 is reduced. In the strong acoustic power limit, the resonance attenuation is suppressed as shown in Figs. 4-1, 4-2, 4-3, and 4-4. Under these considerations, we can almost neglect the relaxation attenuation at low temperatures, e.g., below 4.2 K, where the MARA was measured. The detailed discussion on the saturation effect is given in Sec. V-C together with that on the MARA.

It should be noted that the scaling factors β_1 and β_2 are changed by the way to taking the randomly distributed internal strains into the theory. In Sec. III-C, we took the simple way in order to perform the calculation in an analytically tractable way: The internal stresses are represented by the normal stresses in the [111] and its equivalent directions. The actual crystal has the more complex internal stresses than the above since the internal stresses are caused by the interactions among the acceptor impurities as well as the internal mechanical strains, which will be discussed in Sec. VI-C. Thus, it is very difficult to obtain the values of β_1 and β_2 theoretically. Therefore, we treat β_1 and β_2 as the adjustable scaling factors in comparison of the experimental results with the theory.

B. Magnetoacoustic resonance attenuation (MARA)

1. *Introduction*

As described in the previous section, the ultrasonic attenuation below 4.2 K is mainly due to the resonance attenuation. When the attenuation is measured as a function of the magnetic field, the resonance absorption of the ultrasonic waves is observed at the fields where $E_{n'n} = \hbar\omega \ (n' \neq n)$. The magnitude of the resonance attenuation is proportional to $1/(\Gamma_n + \Gamma_{n'})$, where n and n' denote the relevant levels to the resonance process. Since Γ_n decreases with decreasing the temperature as shown in Fig. 5-1, the attenuation is expected to increase with decreasing the temperature. When the value of Γ_n is small, i.e., the relaxation time is long, the saturation effect appears; the attenuation decreases with increasing the acoustic power. This is consistent with the observations in Sec. IV-B-2. However, since both the temperature and the acoustic power do not affect the resonance-peak positions and therefore the energy splittings, we can disregarded these effects in the consideration of the level splittings of the acceptor ground-state. The resonance fields change with the acoustic frequency, the magnetic field direction, and the uniaxial stress as described in Sec. IV-B. In addition to these facts, the selection rules exist in the MARA, which is seen in the acoustic mode dependence of the MARA described in Sec. IV-B-5.

When we analyze these experimental results in the light of the theory described in Sec. III, the information about the energy levels of the acceptor ground-state is obtained. It should be noted that the theory and formulas described in Sec. III are adequate for the analyses of the experimental results under the strong magnetic fields. Thus, we will derive the Zeeman-splitting parameters of the ground state in Ga-doped Ge by comparing the observations with the theory above 30 kG.

2. *Comparison of the observed resonance fields with the theory*

In order to find the resonance fields, we calculate the magnetic field dependence of the energy splitting $E_{n'n}$. We consider first two cases where the magnetic field is applied in either the [001] or the [111] direction. In these two cases, the acceptor ground-state is well represented by the state for the angular momentum $J = 3/2$ and the formulas are simplified as described in Sec. III. The expressions of $E_{n'n}$, Eqs. (3.43) - (3.46) for $\vec{H}$ // [001] and Eqs. (3.54) - (3.57) for $\vec{H}$ // [111], include five parameters g_1', g_2', q_2, q_3, and Δ_0. In what follows, we try to determine these parameters by comparing the observed resonance fields with the calculations.

We take account of the following factors; the selection rules in the coupling of the ultrasonic waves with the acceptor holes, the acoustic frequency dependence of the MARA, the uniaxial stress dependence of the MARA, and the magnetic field-direction dependence of the MARA. The selection rules are derived from Tables 3-6 and 3-7. For $\vec{H}$ // [001], the hole transitions between levels 1 and 2 and between levels 3 and 4 are allowed for both the transverse waves propagating along the [001] direction and the fast-transverse waves propagating along the [110] direction. For the longitudinal waves propagating along the [110] direction, the transitions between levels 1 and 3 and between levels 2 and 4 are allowed when $\vec{H}$ // [001]. For $\vec{H}$ // [111], all transitions are allowed for both the transverse and the longitudinal waves propagating along the [001] direction. Based on these selection rules, the allowed resonance transitions are related to the observed peaks under $\vec{H}$ // [001] as follows: For the peaks A and B,

$$|E_{12}| = \hbar\omega, \tag{5. 1}$$

or

$$|E_{43}| = \hbar\omega, \tag{5. 2}$$

and, for the peak near 46 kG in Fig. 4-20,

$$|E_{13}| = \hbar\omega, \tag{5. 3}$$

or

$$|E_{42}| = \hbar\omega. \tag{5.4}$$

In addition to these resonance conditions, we take the uniaxial stress dependence of the levels into account. When the stress $\vec{X}$ is applied in the [001] direction, the acceptor ground-state splits according to Eq. (3.15). This indicates that the $|3/2>$ states are higher than $|1/2>$ states in energy.

First, we consider the case of $\vec{H}$ // [001]. Since we try to determine the above five parameters, it is necessary to take four cases for each resonance conditions, (5.1) or (5.2):

$$\begin{aligned}
&(a) \quad q_2 + q_3 > 0 \quad \text{and} \quad g_1' + \tfrac{13}{4} g_2' > 0;\\
&(b) \quad q_2 + q_3 > 0 \quad \text{and} \quad g_1' + \tfrac{13}{4} g_2' < 0;\\
&(c) \quad q_2 + q_3 < 0 \quad \text{and} \quad g_1' + \tfrac{13}{4} g_2' > 0;\\
&(d) \quad q_2 + q_3 < 0 \quad \text{and} \quad g_1' + \tfrac{13}{4} g_2' < 0.
\end{aligned} \tag{5.5}$$

Consequently, eight possible transitions exist for the resonance peaks A and B, which are discussed in Appendix A. From the consideration in Appendix A, the eight cases are reduced to two as

(1) the case (b) for (5.1),

(2) the case (a) for (5.2). (5.6)

Further we take account of the transitions (5.3) and (5.4). When we take

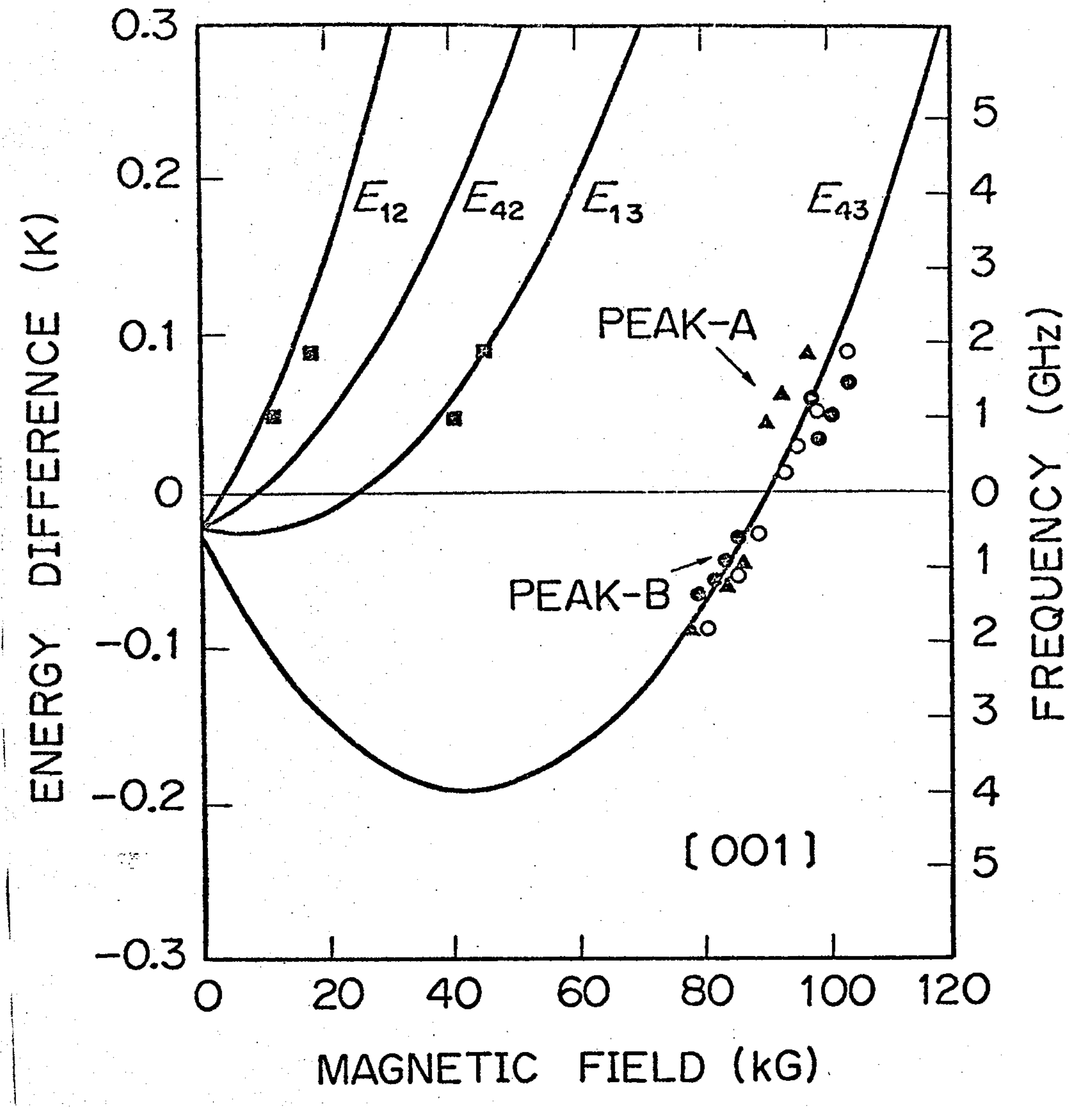

FIG. 5-3. Calculated magnetic field dependences of the energy differences $E_{n'n}$ for $\vec{H}$ // [001] and $\vec{X} = 0$. The ordinate is expressed in two ways: The left scale is in unit of degrees Kelvin. The right scale is in giga-Hertz for plotting the observed frequency dependences of the resonance-peak fields. Closed circles and triangles represent the transverse and the longitudinal waves, respectively, propagating along the [001] direction in #15LA. Open circles and closed rectangles represent the fast-transverse and the longitudinal waves, respectively, propagating along the [110] direction in #15LB.

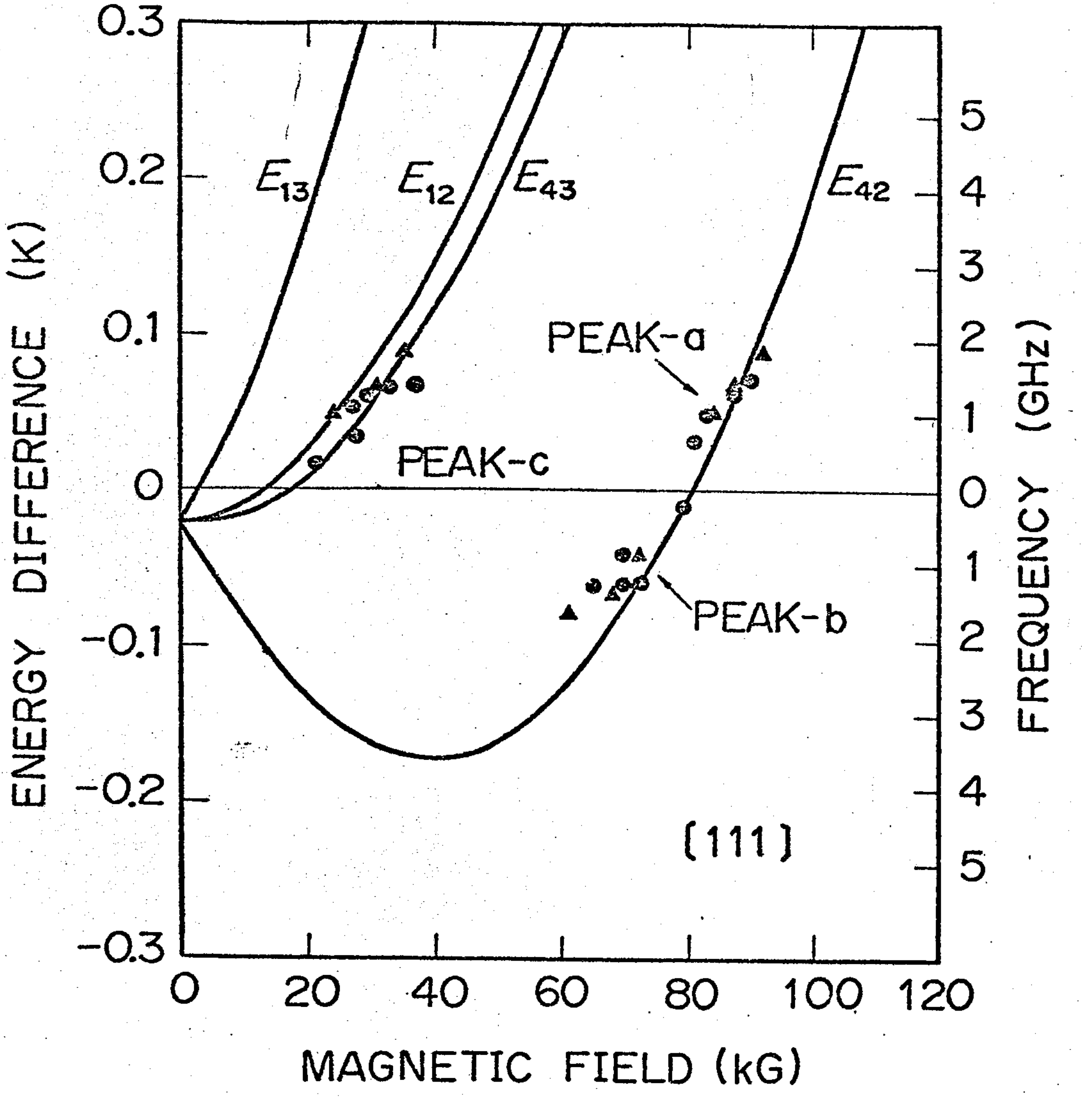

FIG. 5-4. Calculated magnetic field dependences of the energy differences $E_{n'n}$ for $\vec{H}$ // [111]. The ordinate is the same as Fig. 5-3. Closed circles and triangles represent the transverse and the longitudinal waves, respectively, propagating along the [001] direction in #15LA.

Table 5-2. Parameters of the acceptor ground-state obtained from the MARA.

Δ_0	-0.02 ± 0.006 K
g_1'	-0.16 ± 0.08
g_2'	0.08 ± 0.04
q_2	$(0.5 \pm 0.2) \times 10^{-4}$ K/kG^2
q_3	$-(0.6 \pm 0.2) \times 10^{-5}$ K/kG^2
σ	0.03 K for #15LA and #15H
	0.05 K for #16L

(5.3), the linear Zeeman-splitting parameters are obtained by the least-squares fits of the calculations to the observed behavior of the MARA as follows:

(I) $g_1' = 2.75$ and $g_2' = -1.58$ for the case (1) in (5.6);

(II) $g_1' = -0.16$ and $g_2' = 0.08$ for the case (2) in (5.6).

When we take (5.4), the following linear Zeeman-splitting parameters are obtained by the same procedure:

(III) $g_1' = 0.43$ and $g_2' = -1.60$ for the case (1) in (5.6);

(IV) $g_1' = -0.08$ and $g_2' = 0.06$ for the case (2) in (5.6).

The quadratic Zeeman-splitting parameters for the above four cases are the same as $q_2 + q_3 = 0.44 \times 10^{-5}$ K/kG^2. A further reduction in the number is allowed when we take account of the observations for $\vec{H}$ // [111].

Since all transitions are allowed for $\vec{H}$ // [111] as described above, we take the way to calculate the energy splittings $E_{n'n}$ by using the values of the linear Zeeman-splitting parameters obtained above four cases and by adjusting the value of q_2, then to compare those with the observations. Consequently, it turned out that only one case, (II), is adequate to explain the observed behavior of the MARA consistently, whose feature is shown in Figs. 5-3 and 5-4 for $\vec{H}$ // [001] and $\vec{H}$ // [111], respectively. The values of the five parameters obtained are listed in Table 5-2.

3. *Magnetic field-direction dependence of the resonance fields*

We can explain the magnetic field-direction dependence of the resonance fields by using the parameters derived in the previous section. We consider the case where the magnetic field is rotated from the [001] to the [111] direction in the $(1\bar{1}0)$ plane. We choose the magnetic field direction as the axis of quantization of the system under the strong magnetic field.

For an arbitrary direction of the magnetic field in the $(1\bar{1}0)$ plane, we put $\phi = \pi/4$ in Eq. (3.7). Then the Zeeman Hamiltonian is written as

$$\begin{aligned} H_{Zeeman} = \mu_B[g_1'\{\frac{1}{\sqrt{2}}\sin\theta(J_x + J_y) + \cos\theta J_z\} \\ + g_2'\{\frac{1}{\sqrt{2}}\sin\theta(J_x{}^3 + J_y{}^3) + \cos\theta J_z{}^3\}]\, H \\ + [q_1 + q_2\{\frac{1}{\sqrt{2}}\sin\theta(J_x + J_y) + \cos\theta J_z\}^2 \\ + q_3\{\frac{1}{2}\sin^2\theta(J_x{}^2 + J_y{}^2) + \cos^2\theta J_z{}^2\}]\, H^2, \end{aligned} \qquad (5.\ 7)$$

where θ is the angle from the [001] direction. We can obtain the energies of the Zeeman sublevels by diagonalizing the Hamiltonian matrix (5.7). We calculated the energies numerically by using a computer under two assumptions: $q_1 = 0$ K/kG^2 and $\Delta_0 = 0$ K. Since q_1 is cancelled out in the calculation of $E_{n'n}$, the assumption of $q_1 = 0$ K/kG^2 is harmless.

Figure 5-5 shows the calculated magnetic field dependences of the Zeeman sublevels for $\vec{H}$ // [001] and $\vec{H}$ // [111]. For $\vec{H}$ // [001], the levels 3 and 4 cross near 84 kG. Then the resonance condition (5.2) is satisfied at both sides of its crossing, which are shown by broken arrows with T, for the 1.83 GHz-fast-transverse waves propagating along the [110] direction. Broken arrows with L show the allowed transitions for the 1.84 GHz-longitudinal waves propagating along the [110] direction. Solid arrows show the allowed transitions for the 1.23 GHz-transverse waves propagating along the [001] direction (hereafter this waves is considered). For $\vec{H}$ // [111], levels 2 and 4 cross near 80 kG and the transitions are allowed at both sides of there as

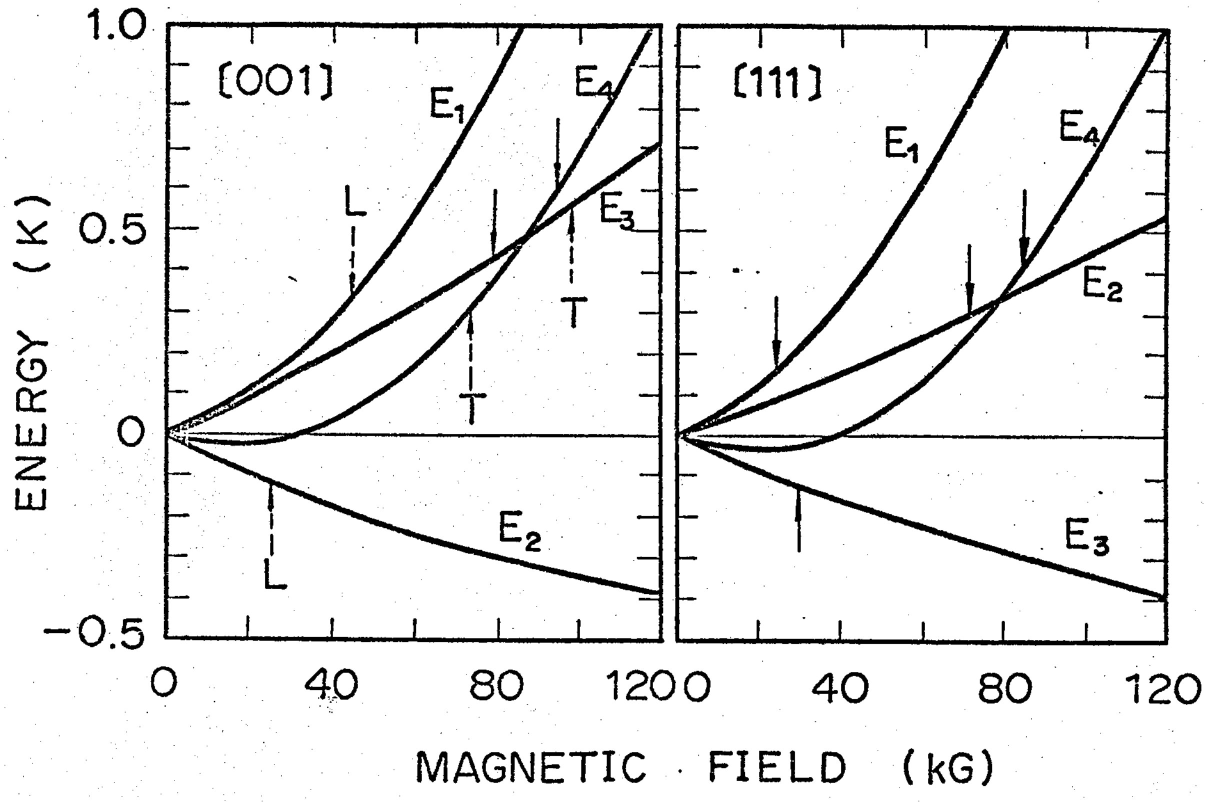

FIG. 5-5. Calculated magnetic field dependences of the energies of the Zeeman sublevels for $\vec{H}$ // [001] and $\vec{H}$ // [111]. The resonance transitions are indicated by arrows: Solid arrows with no letters correspond to the 1.23 GHz-transverse waves propagating along the [001] direction; Broken arrows denoted by the letters *T* and *L* correspond to the 1.83 GHz-fast-transverse waves and the 1.84 GHz-longitudinal waves, respectively, propagating along the [110] direction.

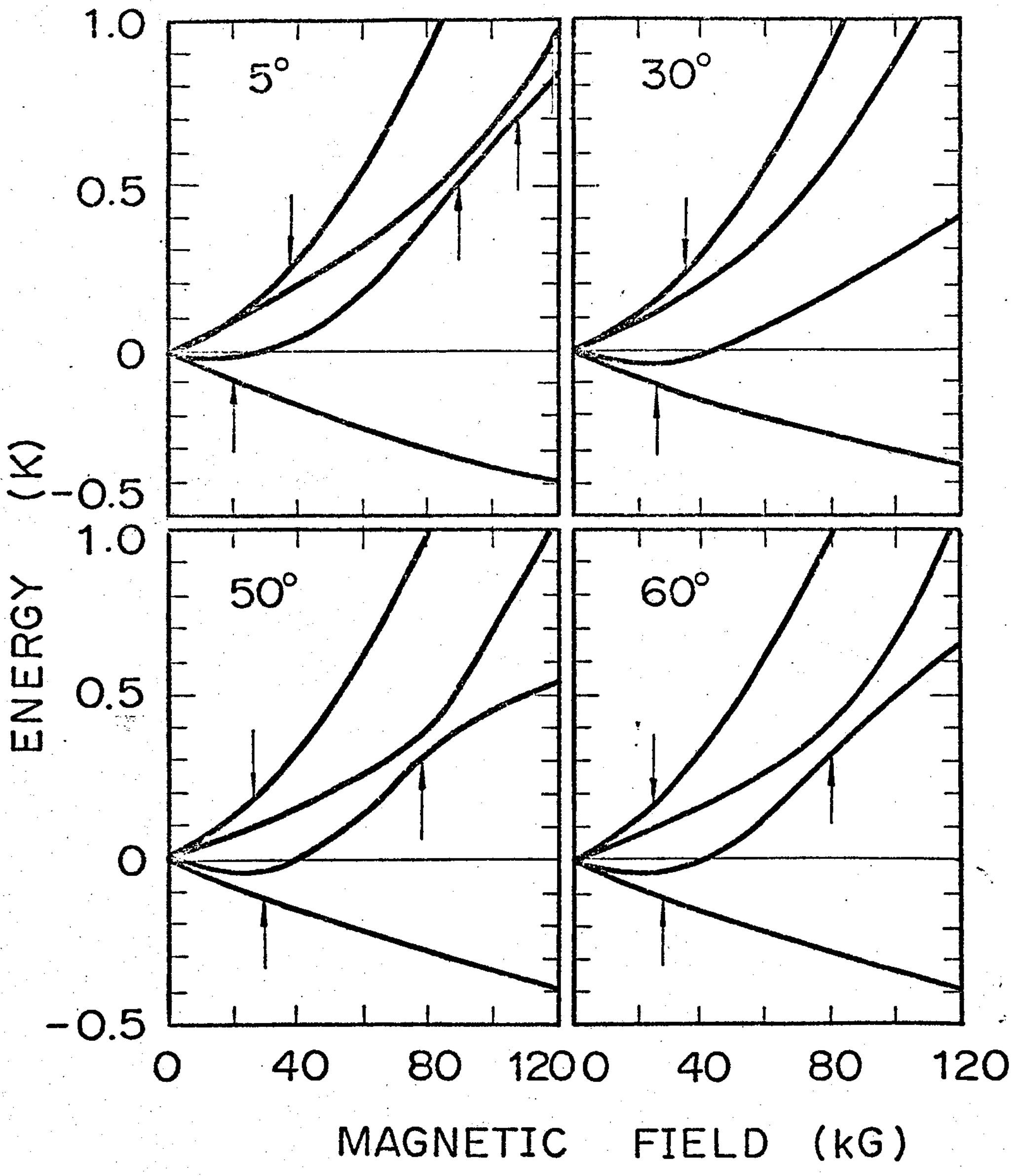

FIG. 5-6. Calculated magnetic field dependences of the energies of the Zeeman sublevels for the cases θ = 5°, 30°, 50°, and 60° (θ is the angle between the [001] direction and the magnetic field in the (1$\bar{1}$0) plane.). Arrows indicate the resonance transitions corresponding to the 1.23 GHz-transverse waves propagating along the [001] direction.

shown by solid arrows. Moreover, two allowed transitions exist in the low magnetic field as shown by solid arrows.

When the magnetic field is rotated from the [001] to the [111] direction by 5°, 30°, 50°, and 60°, the calculated magnetic field dependences of the Zeeman sublevels are shown in Fig. 5-6. In these cases, the movements of the levels with the magnetic field are different from the above two cases (Fig. 5-5). When two levels approach each other, the level anticrossing occurs. This is ascribed to the fact that the acceptor ground-state is described by the linear combination of the $J = 3/2$ states. In other words, the Zeeman-Hamiltonian matrix in the space of $J = 3/2$ states has off-diagonal elements for the arbitrary direction of the magnetic field. When the matrix is diagonalized, these off-diagonal elements cause splittings of the levels in the vicinity of the crossing point. At 5°, the splitting energy due to the anticrossing is smaller than the ultrasonic waves energy and hence the resonance condition allows four transitions as shown by solid arrows. Two arrows in the high magnetic field shift toward the higher magnetic fields than those for $\vec{H}$ // [001]. Two transitions in the low magnetic field, which are forbidden for $\vec{H}$ // [001], are allowed in the present case. When θ increased to 30°, the resonance condition in the high magnetic field is not satisfied below 120 kG but two transitions in the low magnetic field are arrowed as shown by solid arrows, whose positions shift little from those for 5°. For 50° and 60°, the feature of the magnetic field dependences is similar to each other and the anticrossing occurs near 80 kG. The splitting energy is comparable with the ultrasonic waves energy and hence only one transition is allowed in the high magnetic field. In the low magnetic field, two transitions are allowed as the cases for 5° and 30°.

The above calculated results agree well with the observations in Figs. 5-5 and 5-6. So far, we assumed $\Delta_0 = 0$ K, which is inconsistent with the result in Sec. V-B-2. However, since Δ_0 is about -0.02 K, the introduction of it changes only slightly the level diagrams in Figs. 5-5 and 5-6.

We can explain qualitatively the resonance line-shape under the strong magnetic field by using Figs. 5-5 and 5-6. In the vicinity of the [001] direction, the splitting energy due to the anticrossing is small compared with the ultrasonic waves energy used in the present experiment. On the other hand, in the vicinity of the [111] direction, the splitting energy is larger than that of $\vec{H}$ // [001]. Moreover, the levels relevant to the resonance process move slowly with the magnetic field for $\vec{H}$ // [001] than for $\vec{H}$ // [111] as shown in Fig. 5-5. From these facts, we expect the sharper resonance line in the vicinity of the [001] than the [111] direction. This is consistent with the observations in Fig. 4-21.

4. *Magnetic field dependence of the level width* Γ_n

To calculate the level width Γ_n, we use the "dynamic" deformation-potential constants by the same reasons described in Sec. V-A. When the magnetic field is applied in the [001] or the [111] direction, the calculated magnetic field dependences of Γ_R and Γ_n^d ($n = 1, 2, 3, 4$) are shown in Fig. 5-7 or 5-8, respectively. In these calculations, we use the parameters listed in Tables 5-1 and 5-2 and assume that the initial splitting Δ is uniform. These figures show the following facts: The level width is determined by Γ_R below 30 kG and is $\sim 2 \times 10^{-4}$ K. Above 30 kG, the contribution of Γ_n^d to the level width dominates since Γ_n^d increases with increasing the magnetic field. At 120 kG, Γ_1^d becomes $\sim 2 \times 10^{-2}$ K.

Now we consider the attenuations of the 1.23 GHz-ultrasonic waves. The energy of this wave is 6.1×10^{-2} K and then the following relation stands;

$$\hbar\omega \gtrsim 2\Gamma_1^d > 2\Gamma_n^d \quad (n = 2, 3, 4). \tag{5. 8}$$

This indicates that the relaxation attenuation is not neglected under the

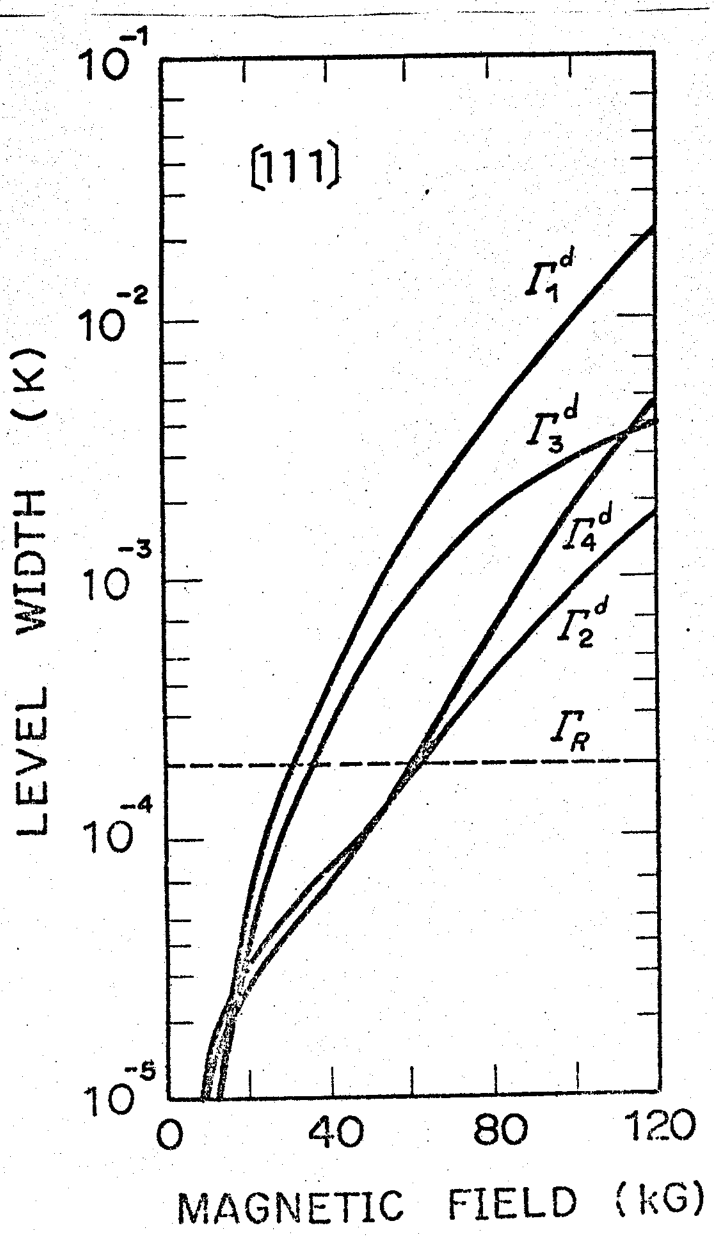

FIG. 5-8. Calculated magnetic field dependences of the level widths Γ_R and $\Gamma_n{}^d$ (n = 1, 2, 3, 4) at 1.3 K for $\vec{H}$ // [111].

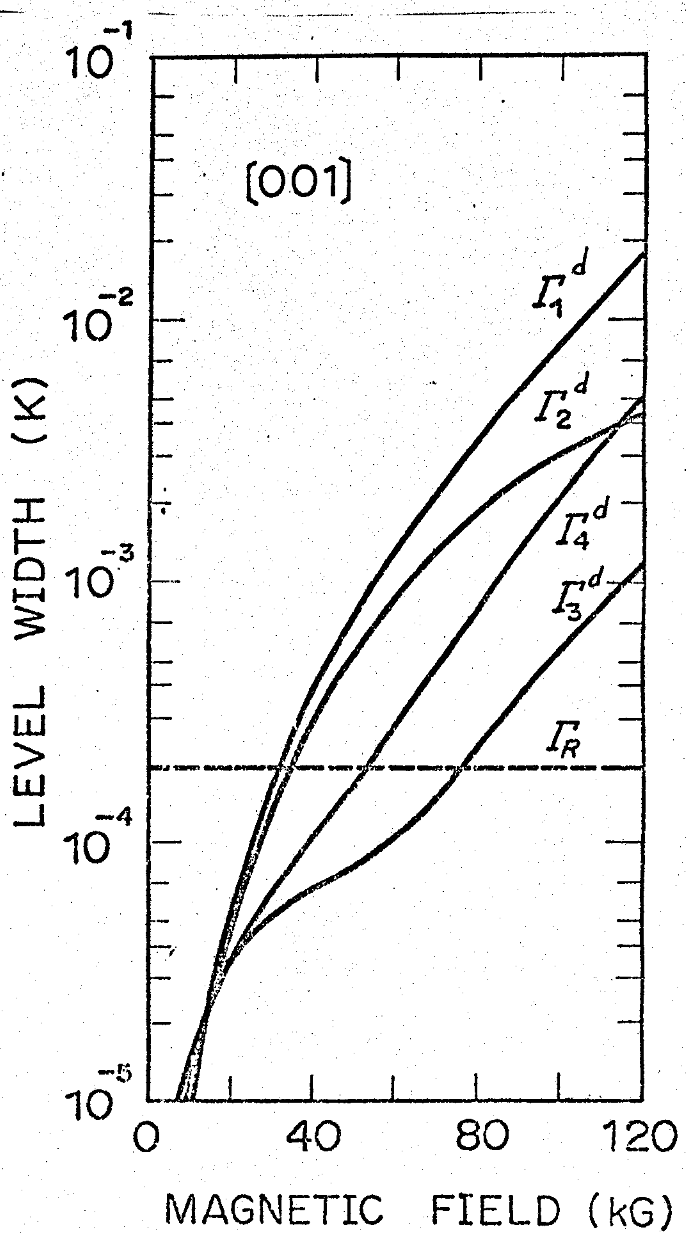

FIG. 5-7. Calculated magnetic field dependences of the level widths Γ_R and $\Gamma_n{}^d$ (n = 1, 2, 3, 4) at 1.3 K for $\vec{H}$ // [001].

strong magnetic field. However, the calculated attenuation shows that the relaxation attenuation makes no peak structures and increases slightly with increasing the magnetic field near 120 kG. Therefore, we can also neglect the relaxation attenuation in the presence of the magnetic field up to 120 kG.

5. *Temperature dependence of the resonance-peak attenuations*

When the resonance condition is satisfied, the resonance-peak attenuation is proportional to $1/(\Gamma_n + \Gamma_{n'})$ as described previously. Since Γ_n decreases with decreasing the temperature as shown in Fig. 5-1, the peak attenuation increases with decreasing the temperature. This is consistent with the observations described in Sec. IV-B-3. Moreover, Γ_n is affected by the magnetic field as shown in Figs. 5-7 and 5-8. To compare the numerical calculation with the observed temperature dependence, we take account of the distributed initial splittings estimated by the line-shape fitting as will be described in the next section.

Figure 5-9 shows the calculated temperature dependences of the resonance attenuations of the peaks *A* (solid lines) and *B* (broken lines) for the 1.23 GHz-transverse waves propagating along the [001] direction in #15LA under $\vec{H}$ // [001]. Groups of lines *AL* and *AH* are obtained by fitting the calculations to the data of the peak *A* at 1.3 and 4.2 K, respectively. Then the scaling factor β is 0.37 for the line *AL* and 0.67 for the line *AH*. All of the observed attenuations lie between the lines *AL* and *AH*; the scaling factor decreases with decreasing the temperature. This is ascribed to the saturation effect, which is more probable at the lower temperatures reflecting the decrease of the level width (Fig. 5-1).

6. *Acceptor-concentration dependence: Line shapes*

The resonance fields are almost the same for three samples with different concentrations as shown in Figs. 4-5 and 4-6, when we take account of those

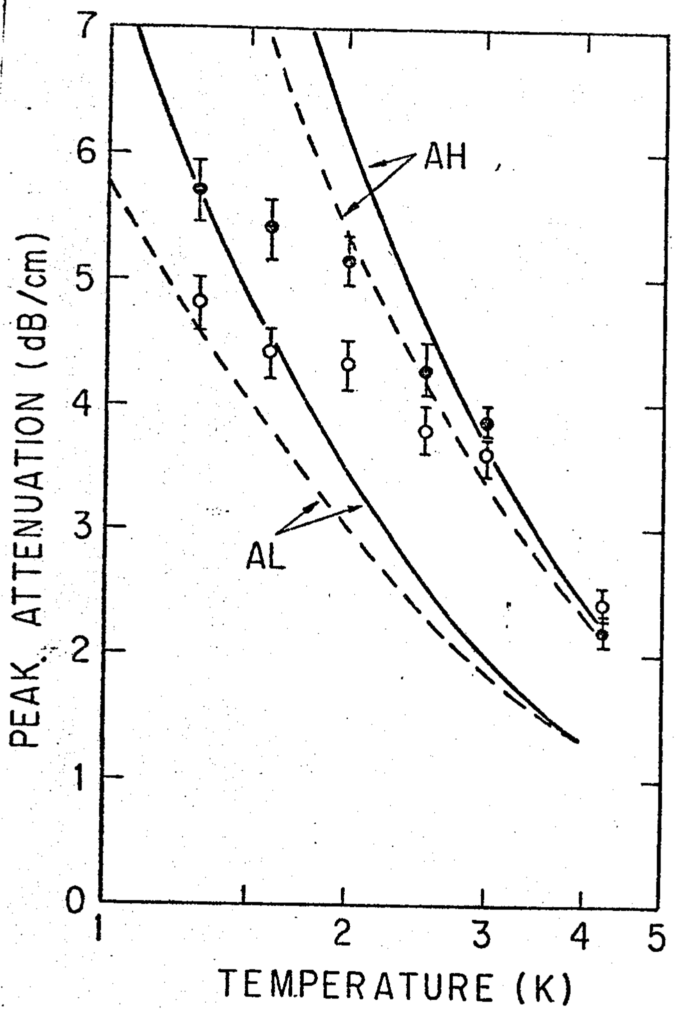

FIG. 5-9. Calculated temperature dependences of the resonance attenuations of the peaks *A* (solid lines) and *B* (broken lines) of the 1.23 GHz-transverse waves propagating along the [001] direction in #15LA under $\vec{H}$ // [001]. Closed and open circles show the data for the peaks *A* and *B*, respectively. Groups of the lines *AL* and *AH* represent the fitted lines to the data at 1.3 and 4.2 K, respectively.

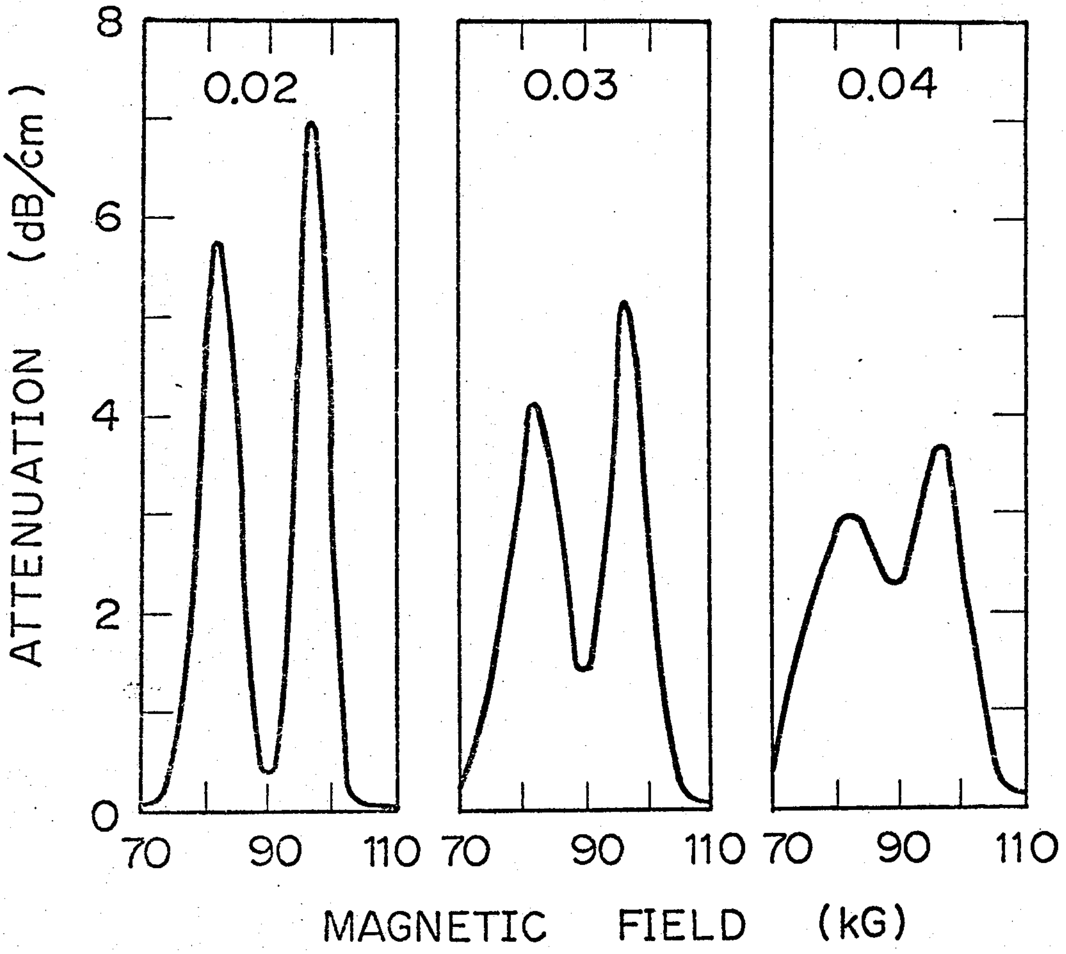

FIG. 5-10. Calculated magnetic field dependences of the attenuation for the case of Fig. 4-5 (solid line) in the range 70 to 110 kG. Inserted decimals indicate the values of σ in unit of degrees Kelvin. The scaling factor β is 0.29.

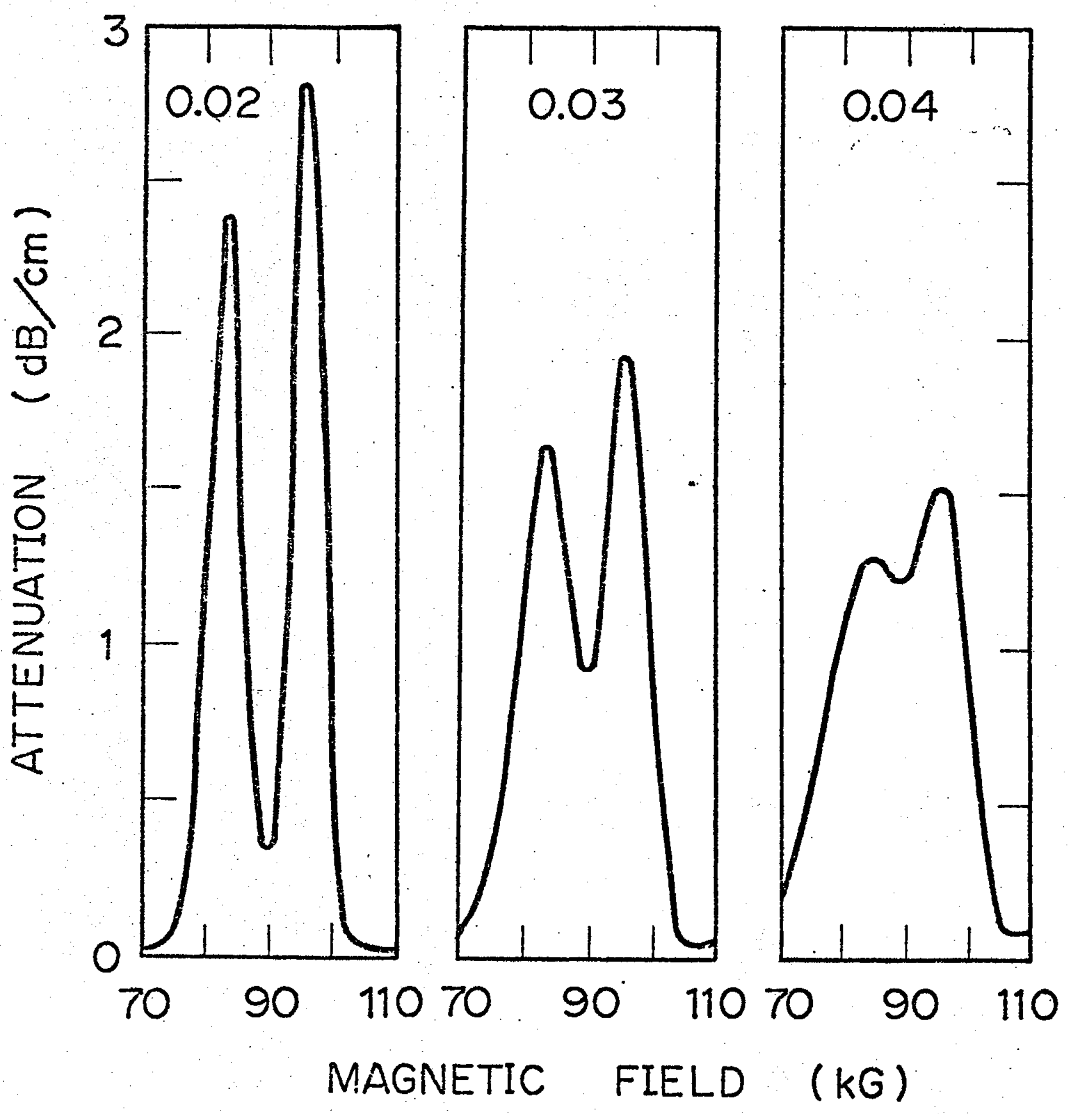

FIG. 5-11. Calculated magnetic field dependences of the attenuation for the case of Fig. 4-6 (solid line) in the range 70 to 110 kG. Inserted decimals indicate the values of σ in unit of degrees Kelvin. The scaling factor β is 0.1.

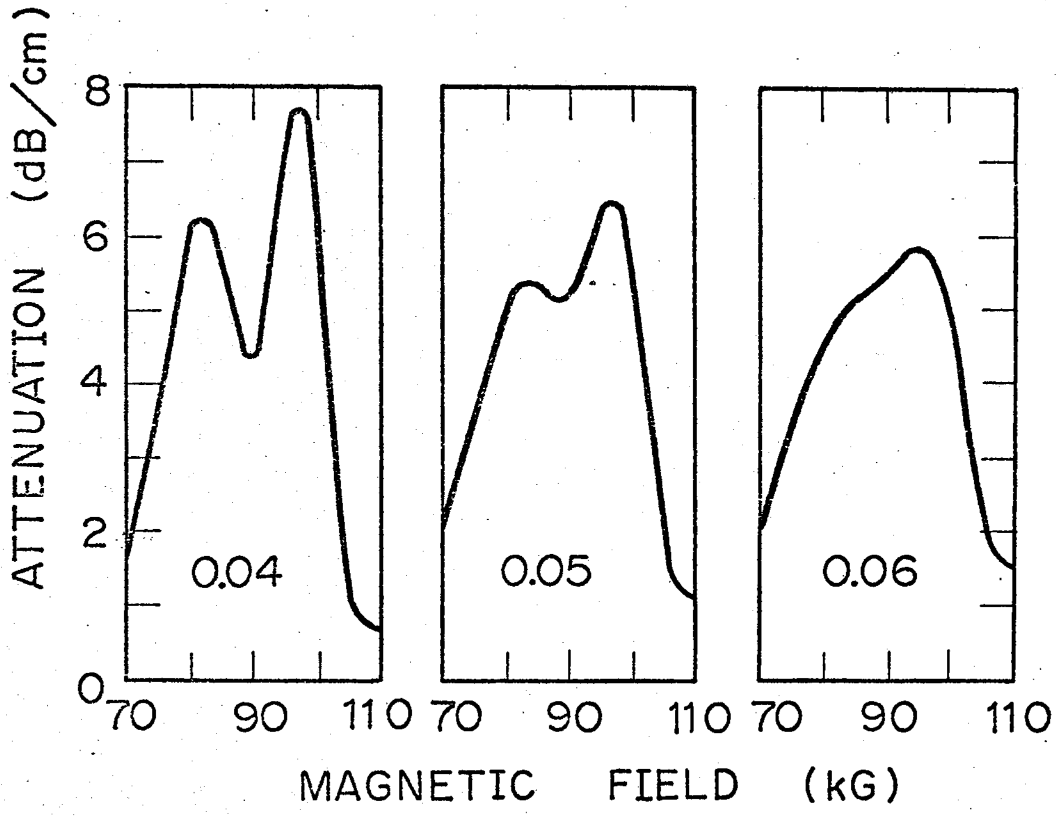

FIG. 5-12. Calculated magnetic field dependences of the attenuation for the case of Fig. 4-6 (broken line) in the range 70 to 110 kG. Inserted decimals indicate the values of σ in unit of degrees Kelvin. The scaling factor β is 0.09.

shifts due to the difference of the acoustic frequency. However, the line shape of the MARA changes with the acceptor concentration. We assume that the resonance line-width is due to the distributed initial splittings. Then we try to fit the line shapes by varying the initial splittings. We take up the resonance line-shapes of the peaks *A* and *B*, since their shapes are clear.

Figures 5-10, 5-11, and 5-12 show the calculated MARA line-shapes in #15LA, #15H, and #16L, respectively. These correspond to the cases of Figs. 4-5 and 4-6. The scaling factor β is adjusted so that the resonance-peak attenuation coinsides with the experimental: $\beta = 0.29$ for #15LA, $\beta = 0.1$ for #15H, and $\beta = 0.09$ for #16L. When σ is taken to be 0.02, 0.03, and 0.04 K for #15LA, the calculated line shape is varied as shown in Fig. 5-10. A good fitting to the observation (the solid line in Fig. 4-5) is obtained for σ = 0.03 K. For #15H and #16L, the calculations with σ = 0.03 and 0.05 K, respectively, are the best fits to the observations (Fig. 4-6). These are listed in Table 5-2. If the value of Δ_0 is changed, the resonance fields shift and then the calculated MARA becomes inconsistent with the observation.

C. Saturation effect in the ultrasonic attenuation

The resonance process may be suppressed by the saturation effect: As increasing the acoustic power, the lower level becomes more depopulated and hence the attenuation saturates. When the relaxation time of the two level system is long, the acoustic power level causing the saturation is lowered.

When we consider first that the two level system is localized mutually, the acoustic power, *P*, dependence of the ultrasonic resonance attenuation is expressed by[56]

$$\alpha_{resonance} = \alpha_0 (1 + P/P_c)^{-1}, \qquad (5.\ 9)$$

where α_0 is the unsaturated attenuation and P_c the critical acoustic power, which is inversely proportional to the relaxation time. We consider two extreme cases for the acoustic power level: (1) $P << P_c$: The number of the resonance process is small enough not to influence noticeably the occupation number. The attenuation in this acoustic power range is unsaturated and is independent on the acoustic power. (2) $P >> P_c$: The resonance attenuation is expected to vary as P^{-1}.

In the absence of the magnetic field, the acoustic power dependences of the attenuations at 1.5 and 4.2 K in #15LB are shown in Fig. 5-13. The attenuations are obtained by subtracting the residual attenuations in Fig. 4-1. As described in Sec. V-A, the attenuations at low temperatures in Fig. 5-13 are mostly ascribed to the resonance process. In the presence of the magnetic field, the acoustic power dependences of the resonance attenuations of the peaks *A* and *B* at two temperatures (1.5 and 4.2 K) in #15LB are shown in Fig. 5-14. This figure is the same as Fig. 4-9; in this case the attenuation is plotted logarithmically.

When we take the most probable fitting of Eq.(5.9) to the experimental results in these figures, the solid lines are obtained and then α_0 and P_c are also obtained as listed in Table 5-3. The critical acoustic power level P_c in the absence and the presence of the magnetic field are almost the same. Since Γ_n in the absence of the magnetic field is much smaller than Γ_n near 100 kG as shown in Fig. 5-7, it is expected that P_c in the absence of the magnetic field is much smaller than P_c near 100 kG. This does not agree with the experimental results in which two P_c are similar. This indicates that the other interactions causing the level broadening exist in addition to both the direct and the Raman processes which are taken into account in the present theory described in Sec. III: for example, the transverse relaxation mechanism due to the interaction among the acceptor impurities as in the amorphous materials.[57] When we assume that the level broadening due to the direct process dominates over the transverse relaxation process near 100 kG, the

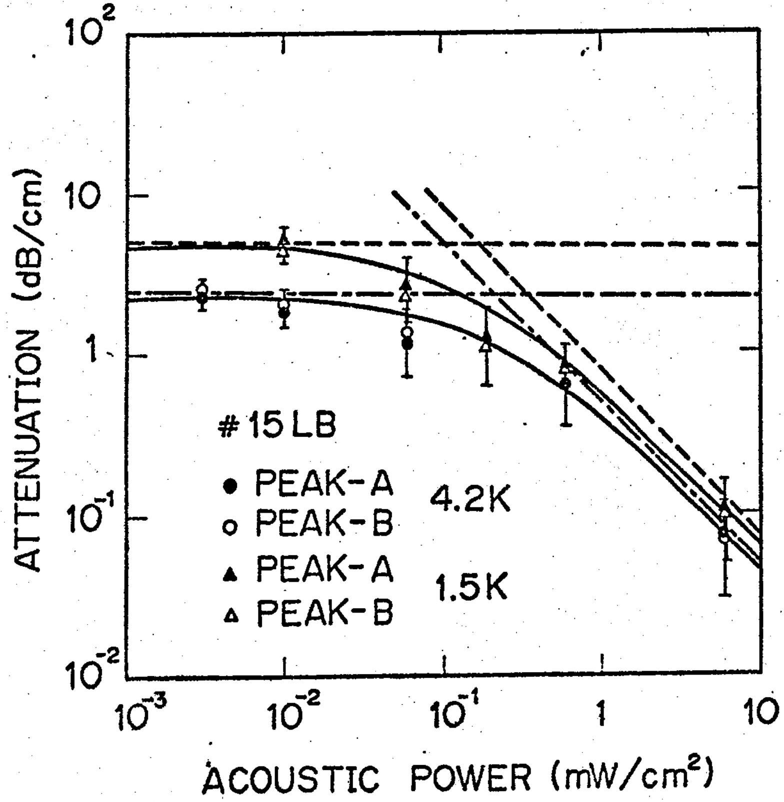

FIG. 5-14. Acoustic power dependences of the resonance-peak attenuations at 1.5 K (triangles) and at 4.2 K (circles) for the case of Fig. 4-8. Solid lines and broken lines are the same as Fig. 5-13.

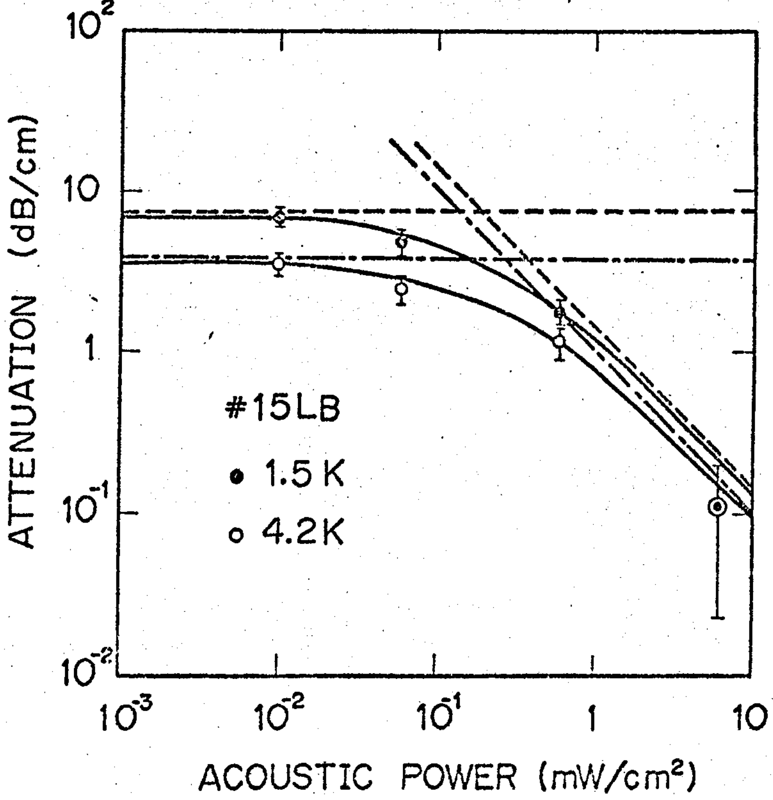

FIG. 5-13. Acoustic power dependences of the attenuations at 1.5 K (closed circles) and 4.2 K (open circles) for the case of Fig. 4-1. Solid lines indicate the most probable fitting lines of Eq.(5.9). Broken lines indicate the asymptotic lines in two extreme cases.

Table 5-3. Unsaturated attenuation α_0 and critical acoustic power level P_c in #15LB.

(a) In the absence of the magnetic field.

T (K)	α_0 (dB/cm)	P_c (mW/cm^2)
1.5	7.1	0.19
4.2	3.6	0.27

(b) Near 100 kG.

T (K)	α_0 (dB/cm)	P_c (mW/cm^2)
1.5	3.9	0.17
4.2	2.2	0.22

level width in the absence of the magnetic field is mostly determined by the other mechanism than either the direct or the Raman process in the acceptor state ground-state with the small splitting ($\sim$0.02 K).

The saturation effect in the ultrasonic attenuation in *p*-Ge was observed first by Ortlieb *et al.*[51] They measured the acoustic power dependence of the attenuation and then the critical acoustic power level is estimated to be $\sim$0.2 mW/cm^2. Their critical acoustic power level is the same order of ours.

We should remark here about the calculated temperature dependence of the ultrasonic attenuation in the absence of the magnetic field described in Sec. V-A. As described above, the calculated Γ_n at low temperatures becomes too small in the absence of the magnetic field and hence it is expected that some other relaxation processes may dominate. At the present stage, however, we cannot take account of these quantitatively. Therefore, we calculated the temperature dependence of the attenuation as shown in Sec. V-A neglecting these relaxation processes.

VI. DISCUSSION

A. Linear Zeeman effect

Soepangkat and Fisher (SF) have investigated the transverse Zeeman effect of boron and thallium acceptors in germanium by means of the optical absorption.[34] The g-values derived by SF are listed in Table 3-3 for boron acceptors. We attempted first to explain the MARA by using the g-values derived by SF.[32,33] However, we found that these values were not adequate to explain the MARA described in Sec. IV consistently. As described in Sec. V-B, we derived the g-values so that the observed behaviors of the MARA were explained consistently.

It is clear that SF's and ours are quite different beyond the experimental error even if the difference of the chemical shift among these impurities is taken into account. To resolve this problem, we reconsidered the SF's way to derive the g-values. By comparing the observed excitation spectra for the Zeeman components with the calculations by Lin-Chung and Wallis (LCW)[43] and by Bhattacharjee and Rodriguez (BR),[44] SF have chosen an assignment out of thirty-two possibilities for the D-line spectra (Fig. 23 in Ref.34): Their guiding principle was to adopt the values which are close to the theoretical values.[43] We searched whether an alternative assignment was possible by unloosing a little their guiding principle. Then, we found a new reasonable assignment by exchanging D_4 and D_5 transitions in Fig. 23 of Ref. 34 (see Sec. VI-D-1). The g-values obtained by the new assignment are given in Table 3-3 at the second entry for SF. The new g-values are in good agreement with those obtained from the MARA.

The g-values obtained in the present investigation are much less than those calculated in the effective mass theory (Table 3-3). The cause is not clear. It should be noted, however, that the theoretical g-values are sensitive to the values of the valence-band parameters, as pointed out by SOH.[21] The present formulas for the Zeeman splittings of the acceptor ground-state are derived under the following assumptions: The unperturbed ground state is separated from both the excited states and the valence-band edge, and the magnetic field is so small that the splitting of each level can be treated independently. This means that the theory described in Sec. III-B is valid when γ is small compared with unity, where γ is the dimensionless parameter for the magnetic field introduced by Yafet *et al.*[58]

By using the values of the parameters listed in Table 5-1, $\gamma = 0.27$ is obtained at 100 kG for Ga-doped Ge. In this calculation of γ, we used $m^* = 0.2\, m_0$ (m_0 is the free electron mass) as the effective mass of Ga-acceptor holes in Ge, whose value is determined from the ionization energy of Ga-acceptor ($\simeq$ 10.97 meV)[59] in the effective mass approximation.[60] Therefore, the value of γ may be larger than the above one. Thus, although the behavior of the MARA is explained successfully, the derived Zeeman-splitting parameters may include some errors since the theory approaches its limit for the validity.

The g-values of the acceptor ground-state can be derived directly by means of ESR method. In p-Ge, the successful ESR study have not been reported in our knowledge. Mitsuma and Morigaki[61] have searched the ESR signal in p-Ge with X-band microwaves by sweeping the magnetic field from 0 to 15 kG. This means that the ESR signal was searched in the regime $g > 0.48$. The new g-values does not conflict with the ESR study.

B. Quadratic Zeeman effect (diamagnetic shift)

The quadratic Zeeman effect is effective for the holes moving in a large orbits under the strong magnetic field (Sec. III-B). In order to check this, we calculate the coefficient of the quadratic Zeeman effect by taking a simple model. The Hamiltonian of the quadratic Zeeman effect is expressed by[45]

$$H'' = (e^2/2mc^2)\,\vec{A}^2, \qquad (6.\ 1)$$

where e, m, and c are the electronic charge, the electron mass, and the light velocity, respectively. The vector potential $\vec{A}$ is given by

$$\vec{A} = \frac{1}{2}\vec{H} \times \vec{r}, \tag{6.2}$$

where $\vec{r}$ is the position vector.

By using Eqs.(6.1) and (6.2), we can calculate the quadratic Zeeman energy (diamagnetic shift) in the first-order perturbation. When we take the s-like envelope function of the acceptor ground-state as the unperturbed wave function, i.e., according to Eq.(3.2) and Table 3-1,

$$\psi_s = (\pi a^{*3})^{-1/2}\exp(-r/a^*), \tag{6.3}$$

the energy $\Delta E''$ is calculated as

$$\Delta E'' = (e^2 a^{*2}/4mc^2)\, H^2 \equiv qH^2. \tag{6.4}$$

The coefficient q is calculated for p-Ge as

$$q = 0.68 \times 10^{-4}\ \mathrm{K/kG^2}. \tag{6.5}$$

This value is of the same order of q_2 and q_3 as shown in Table 5-2.

Now we consider the quadratic Zeeman effect in p-Si and p-GaP by taking the above simple model. Using the quadratic Zeeman energy expressed by Eq.(6.4), the coefficient q is calculated as 0.11×10^{-4} K/kG^2 and 0.08×10^{-4} K/kG^2 for p-Si and p-GaP, respectively. These values are small compared with one for p-Ge. This indicates that the quadratic Zeeman effect is more probable for the acceptor holes with large orbits as in Ge ($a^* = 37.8$ Å) than in Si ($a^* = 13$ Å) or GaP ($a^* = 11$ Å).

C. Initial splitting of the acceptor ground-state

By comparing the ultrasonic measurements with the theory in the effective mass approximation, it is found that the ground state of the shallow acceptors in the cubic semiconductors is split due to the initial local fields. The splittings are induced by the static fields which break the tetrahedral symmetry at the acceptor site. In the absence of the external fields, the splitting may be caused by the initial local stresses which is brought about by the randomly distributed crystal imperfections and the dislocations as well as weak correlations among the acceptor impurities.[24] We have characterized the feature of these splittings by the Gaussian distribution function in order to make the calculation tractable. Consequently, the average splitting Δ_0 does not vary appreciably with the acceptor concentration in our samples. The values of σ vary slightly. It should be noted, however, these values of Δ_0 and σ were obtained by the comparison of the MARA line-shape under the strong magnetic field with the theory as described in Sec. V-B. Thus, this may not necessarily represent the splittings in the absence of the magnetic field. Anyhow, we will discuss the origin of the initial splittings.

The origins of the local fields ascribed to the following mechanisms: (1) the presence of point defects such as vacancy, oxgen, hydragen, or carbon impurities; (2) the presence of dislocations; (3) interactions among the acceptor impurities; (4) the Jahn-Teller effect for the acceptor state; (5) others. We discuss these mechanisms.

(1) It is known that there are considerable amounts of electrically inactive elements in germanium, which act as the point defects. The presence of the point defects modifies the acceptor states through causing the local mechanical stresses. We estimate the strain fields due to the point defects under the following assumptions: (a) The point defects are randomly distributed in an elastically isotropic media with a large but finite radius. (b) The strain fields at the point of observation mainly come from its nearest neighbor.

Under these assumptions, the probability of finding the nearest neighbor at a distance r is obtained as, after Sonder and Schweinler,[63]

$$dP = 4\pi N r^2 \exp(-\frac{4}{3}\pi N r^3) dr, \tag{6. 6}$$

where N is the concentration of the point defects. A strain field ε at large distance r is expressed by[64,65]

$$\varepsilon = A/r^3. \tag{6. 7}$$

Under the assumption (a), the proportional factor A is related to the volume dilation ΔV by[65]

$$A = \frac{1+\nu}{12\pi(1-\nu)} \Delta V, \tag{6. 8}$$

where ν is the Poisson's ratio of the media.

Using Eqs.(6.6) and (6.7), we obtain the distribution of the strain fields as

$$\begin{aligned}(dP/d\varepsilon) &= (dP/dr)(dr/d\varepsilon)\\ &= -\frac{4\pi NA}{3}\varepsilon^{-2}\exp(-\frac{4}{3}\pi NA/\varepsilon).\end{aligned} \tag{6. 9}$$

Here we take the values of $N = 10^{16}\ \text{cm}^{-3}$, $\nu = 0.27$, and $\Delta V = 8.14 \times 10^{-23} \text{cm}^3$ for the oxygen impurity in germanium tentatively. From the graphical evaluation, the distribution (6.9) has a width 2.2×10^{-8} centered on -8.0×10^{-9}. These values correspond to our average splitting Δ_0 and the variance σ as

$$\Delta_0 = -0.00021\ \text{K} \quad \text{and} \quad \sigma = 0.00055\ \text{K}. \tag{6. 10}$$

These values are very small compared with the results in Table 5-2. Therefore, the presence of the point defects does not play a dominant role to form the initial splittings.

(2) The dislocations modify the acceptor states by introducing mechanical stresses which break the tetrahedral symmetry at the acceptor site. Since the stress field around the dislocation is very complicated, we make the following assumptions and simplifications: (a) The dislocations are randomly distributed in an elastically isotropic media. (b) All the dislocations are parallel and straight. This assumption enables us to regard the system as the two dimensional one. (c) The strain fields at the point of observation mainly come from its nearest neighbor. Under these assumptions and simplifications, the probability of finding the nearest neighbor at r is obtained as

$$dP = 2\pi D r \exp(-\pi D r^2), \tag{6. 11}$$

where D is the dislocation density. A strain field ε at large distance r is expressed by[66]

$$\varepsilon = B/r. \tag{6. 12}$$

In order to estimate the strain field, the proportional factor B is assumed as

$$B \simeq b/2\pi, \tag{6. 13}$$

where b is the magnitude of the Burgers vector.

Using Eqs.(6.11) and (6.12), we obtain the distribution of the strain field as

$$(dP/d\varepsilon) = (dP/dr)(dr/d\varepsilon) = -\pi D^2 B^2 \varepsilon^{-3} \exp(-\pi D B^2/\varepsilon^2). \tag{6. 14}$$

When we evaluate the distribution graphically by using the values of $D = 10^3$ cm^{-2} and $b = 5.66 \times 10^{-8}$ cm, it turns out that the distribution has a width 1.1×10^{-6} centered on -4.1×10^{-7}. With these results and $D_u^a = 3.32$ eV, we obtain the average splitting Δ_0 and the variance σ as

$$\Delta_0 = -0.011 \text{ K} \quad \text{and} \quad \sigma = 0.028 \text{ K}. \tag{6. 15}$$

These values are in good agreement with the results in Table 5-2. Thus, we can take the presence of the dislocations of the order of 10^3 cm^{-2} as one of the origins for the initial splittings.

(3) As one of the interactions among the acceptor impurities, the possibility of the preferential aggregation or clustering of the impurity atom is considered first. However, the possibility of clustering is low in this kind of dilute concentrations. The second is the splitting by the formation of the molecular-ion-type combination of the gallium acceptors, which is probable in the presence of the compensated impurities.[10] This effect can be ruled out since our samples are not compensated artificially. The third is the overlap of the wave functions of the acceptor ground-state. This effect is discussed later in relation to the other experimantal results for the initial splittings.

(4) Bir has discussed the existence of the Jahn-Teller effect for the shallow acceptors in cubic semiconductors.[64] Since the stability criteria given by Bir are not satisfied for the gallium acceptors in germanium, the static Jahn-Teller effect is not stable in this case. Thus, the possibility is ruled out for these shallow acceptors.

Challis and Halbo[29] pointed out the possibility of the dynamic Jahn-Teller effect[30] generating additional low-lying acceptor levels through the magneto-thermal conductivity measurement. Since we have no tractable theory of this effect, we cannot evaluate the possibility quantitatively.

(5) The electric field or the electric field-gradient effects by the point-

defect charges, etc. may be other possibilities for the origins of the initial splittings.

Several values for the initial splittings of the Ga-acceptor ground-state in Ge have been reported, which are shown in Table 6-1. We have characterized the distribution of the initial splittings by the Gaussian distribution. On the other hand, Challis *et al.*[31] and Ortlieb *et al.*[51] assumed that the distribution is constant up to a maximum whose value is given in Table 6-1. The values of the initial splittings are widely distributed regardless the similar acceptor concentrations and dislocation densities. Ultrasonic measurements give the small values in spite of the different assumptions for the distribution of the initial splittings. Heat-pulse propagation[28] and thermal conductivity[31] give the larger values than the former ones. In addition to this fact, our results are the smallest ones in the four experimental results. The cause of this discrepancy is not clear at the present stage. However, we notice the following facts.

(a) As pointed out in Sec. V-C, the level broadening determined from the MARA line-shapes is too small in the absence of the magnetic field. Then we suggested the presence of the relaxation mechanism due to the interaction among the acceptor impurities, which causes the initial splitting effectively in the absence of the magnetic field. At this point, we consider the shrinkage effect on the wave functions of the acceptor ground-state. By variational method, the shrinkage of the effective Bohr radius is given by[62]

$$a^*(H) = a^*[1 - (\kappa a^{*3}/2m^*c^2)\, H^2],$$

where $a^*(H)$ and a^* are the effective Bohr radii in the presence and the absence of the magnetic field, respectively. κ and m^* are the dielectric constant and the effective mass of the Ga-acceptor holes, respectively. Using the values listed in Table 5-1, we find that the shrinkage of the effective Bohr radius

Table 6-1. Initial splittings of the Ga-acceptor ground-state in Ge and the assumptions for the distribution.

	Sample characteristics		Initial splittings	Assumptions for the distribution
	Concentration (cm^{-3})	Dislocation density (cm^{-2})	(K)	
Fjeldly *et al.*[a] (Heat-pulse propagation)	5×10^{14} 1.7×10^{16}	unknown	4.2 5.9	(A)
Challis *et al.*[b] (Thermal conductivity)	1×10^{14} 1.3×10^{16}	$\sim 10^4$	10.0	(B)
Ortlieb *et al.*[c] (Ultrasonic attenuation at H = 0 kG)	3.0×10^{16}	∿700	0.09	(B)
Present (Ultrasonic attenuation at H = 100 kG)	3.5×10^{15} 7.0×10^{15} 2.5×10^{16}	∿700 ∿900 ∿400	-0.02 (0.03) -0.02 (0.03) -0.02 (0.05)	(C)

[a] See Ref. 28. [b] See Ref. 31. [c] See Ref. 51.

(A) The distribution is characterized by a force per unit area of average magnitude given in the Table and random direction.

(B) The distribution is constant up to a maximum value, whose value is given in the Table.

(C) The distribution is represented by the Gaussian distribution function, Eq.(3.31) in the text, with the average values Δ_0 and the variance σ (paranthesis). These values are given in the Table.

is 2.6 % at 100 kG. The shrinkage of the wave functions at large distances from the impurity atoms is larger than that of the effective Bohr radius.[62] The interaction among the acceptor impurities can be reduced by this effect under strong magnetic field. Then, the relaxation mechanism is quenched at the strong magnetic field where the MARA was observed.

(b) When we take the large values of the initial splittings, e.g., the values derived from heat-pulse propagation[28] or thermal conductivity,[31] as the parameters for the Gaussian distribution, the temperature dependence of the ultrasonic attenuation cannot be explained; The calculated attenuation decreases with decreasing the temperature below 4 K, which conflicts with the observations described in Sec. IV-A.

D. Relation to other experimental results

1. *Magnetooptical measurements by SF*[34]

We discuss the way to derive a new assignment for SF's magnetooptical spectra, which resolves the difference between the g-values obtained from the MARA and the SF's results as described in Sec. VI-A.

We will discuss the D-line spectra in B-doped Ge for $\vec{H}$ // [001] identical to that of SF.[34] When the magnetic field is applied, the components of the D-line are assigned in thirty-two ways. We take up four cases, where the relative intensities of the Zeeman components agree well with the theoretical ones[43, 44] for the D-line. These four assignments are illustrated in Fig. 6-1. These are divided into two cases, viz., either $v_D > 0$ or $v_D < 0$, where v_D is the parameter of the transition probability for the D-components introduced by BR.[44] Since the sign of v_D is undetermined at this point, it is necessary to consider two cases. In Fig. 6-1, (a) and (b) are two assignments for $v_D > 0$, and (c) and (d) are for $v_D < 0$. The assignment (a) is the same one adopted by SF (Fig. 23 in Ref. 34). Corresponding to these four assignments, the g-values of B-acceptor ground-state can be calculated by using the SF's data as follows:

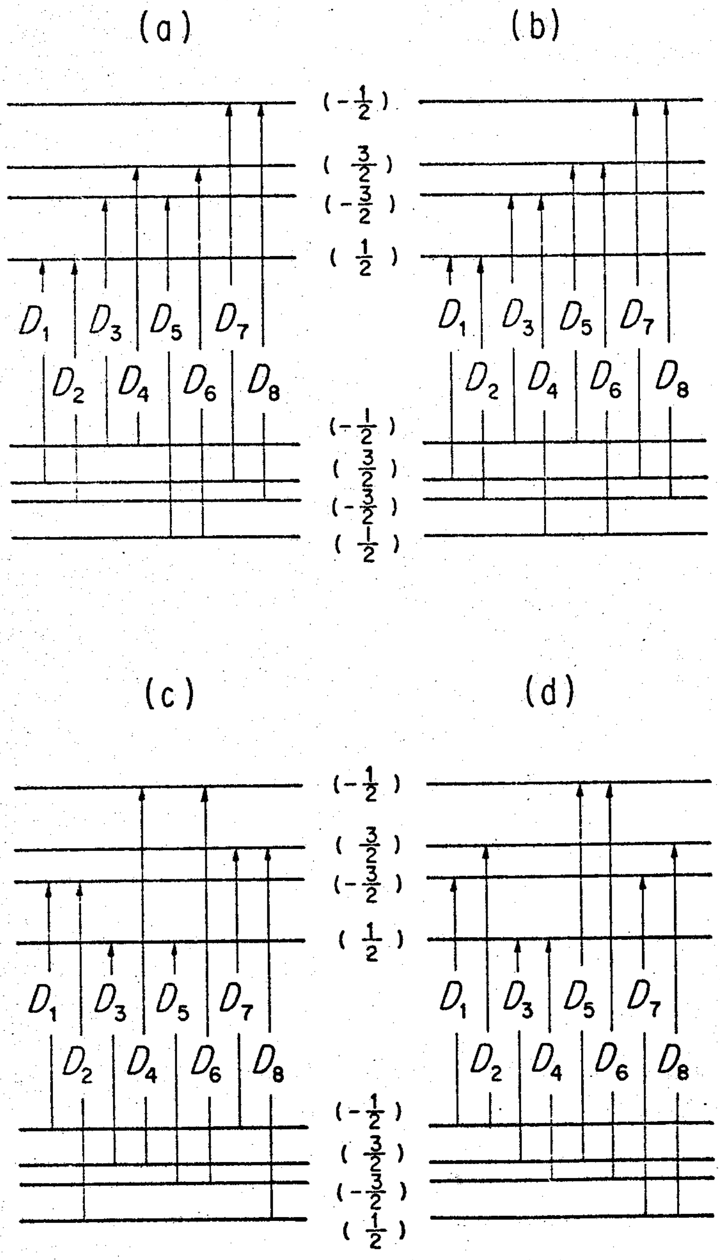

FIG. 6-1. Four possible assignments of the electric-dipole transition for the *D*-components from the magnetooptical spectra of boron in germanium under $\vec{H}$ // [001] given by SF.[34]

$$
\begin{aligned}
&\text{(a)}\quad g_{1/2}{}' = -1.53 \pm 0.09 \quad \text{and} \quad g_{3/2}{}' = 0.03 \pm 0.04;\\
&\text{(b)}\quad g_{1/2}{}' = -0.22 \pm 0.09 \quad \text{and} \quad g_{3/2}{}' = 0.03 \pm 0.04;\\
&\text{(c)}\quad g_{1/2}{}' = -0.10 \pm 0.08 \quad \text{and} \quad g_{3/2}{}' = 0.51 \pm 0.03;\\
&\text{(d)}\quad g_{1/2}{}' = -6.12 \pm 0.08 \quad \text{and} \quad g_{3/2}{}' = 0.07 \pm 0.03.
\end{aligned}
\tag{6. 16}
$$

A further reduction in the number of the above four is accomplished when we compare the calculated magnetic field dependences of the energy differences $E_{n'n}$, as the same way described in Sec. V-B-2, with the observed behavior of the MARA. After this, it turns out that the g-values for three cases, (a), (c), and (d), are not adequate to explain the observed MARA consistently. Then only one case (b) remains. Using the new g-values for the case (b), we can explain the results of the other spectra and the spectra for the other magnetic field direction[34] consistently. In particular, the G-line spectra, which is not explained by the SF's assignment, can be interpreted by the new g-values in agreement with the SF's remark: The small splitting of the G-line is related to the small g-values of the acceptor ground-state.[34]

2. *Magnetothermal conductivity measurement by Challis et al.*[29,31]

We consider the magnetothermal conductivity in lightly Ga-doped Ge by Challis *et al.*[29,31] The experimental results for $\vec{H}$ // [110] are characterized as follows: In the magnetic field below 80 kG, the conductivity shows a slight increase and then has a maximum. The maximum change is less than 1 % compared with the value in the absence of the magnetic field. This behavior is similar to the other magnetic field directions. As the magnetic field increases above 80 kG, the conductivity decreases up to 130 kG at temperatures between 1.8

and 2.5 K, or has a minimum at temperatures between 1.14 and 1.35 K. This minimum shifts toward the lower magnetic field with decreasing the temperature.

The magnetothermal conductivity in *p*-Si has been explained by the SM-model modified by considering the linear Zeeman effect.[13] However, the magnetothermal conductivity in *p*-Ge could not be explained by this model. Challis *et al.*[29,31] ascribed the anomalous behavior in *p*-Ge to the existence of the low-lying excited states by the dynamic Jahn-Teller effect[30] for the acceptor state. The energy spacing between the ground state and the low-lying excited states are smaller for Ga in Ge than for B in Si, provided the values of the deformation-potential constants are similar in these materials.[32] Therefore, if the anomalous behavior in the magnetothermal conductivity in *p*-Ge is caused by the excited states, a similar anomaly should be observed in *p*-Si, in contradiction to the experiment.

We consider that the reported anomalous behavior of the magnetothermal conductivity in *p*-Ge stems from the use of the inadequate Zeeman-splitting parameters and the neglect of the quadratic Zeeman effect. Now we calculate the magnetothermal conductivity in *p*-Ge at low temperatures by using the new *g*-values and taking account of the quadratic Zeeman effect. We use the usual semi-phenomenological formula for the lattice thermal-conductivity:[27]

$$K(H,T) = \frac{k^4T^3}{6\pi^2\hbar^3} \sum_{t=1}^{3} \frac{1}{v_t} \int_0^\infty \frac{x^4 e^x}{(e^x - 1)^2} \tau \, dx, \tag{6. 17}$$

with

$$\tau^{-1} = \tau_{Bt}^{-1} + \tau_I^{-1} + \tau_{h\text{-}p}^{-1}, \tag{6. 18}$$

where $x \equiv \hbar\omega/kT$ and τ_{Bt}, τ_I, and $\tau_{h\text{-}p}$ are the phonon relaxation times due to the boundary, the isotopic, and the acceptor-hole scatterings, respectively. The subscript *t* denotes the phonon branch as described in Sec. III-C.

We calculate the phonon relaxation-rate τ_{h-p}^{-1} in the light of the theory described in Sec. III by taking account of the following three processes; the resonance scattering, the second-order elastic scattering, and the second-order inelastic scattering. The expressions of the relaxation rates for these three processes are given in Appendices B, C, and D. In the present calculation, we consider the case of $\vec{H}$ // [001] since the formulas become too complicated for $\vec{H}$ // [110] and the experimental results are similar for these two cases.

We consider first the thermal conductivity assuming that the initial splittings are homogeneous for simplicity. Figures 6-2 and 6-3 show the calculated magnetic field dependences of the thermal conductivity at 1.10 and 2.50 K, respectively, in the sample of Challis and Halbo.[29] The numerical values of the parameters used are listed in Tables 5-1 and 5-2. The conductivity is normalized at 30 kG, above which the present theory can be applied rather well. In these figures, the data by Challis *et al.*[31] are also shown by broken lines. At 1.10 K, the conductivity decreases with increasing the magnetic field and then has a minimum at some strength of the magnetic field. The minimum shifts toward the higher magnetic field with decreasing Δ as shown in Fig. 6-2. With further increase of the magnetic field, the conductivity increases. On the other hand, the conductivity decreases with increasing both the magnetic field up to 130 kG and Δ at 2.50 K as shown in Fig. 6-3.

In the above calculation, we assumed the homogeneous initial splittings. When we take account of the distribution of the initial splittings, the calculated may agree the observed magnetic field dependence. Further, the adopted splitting is of the order of 1 K, which is much larger than one obtained from the MARA. This may be ascribed to the fact that, for the study of the thermal conductivity, the intimate contact between the heater and the sample is required to reduce the contact resistance. We cannot rule out the posibility of the introduction of the external stresses and further the distribution

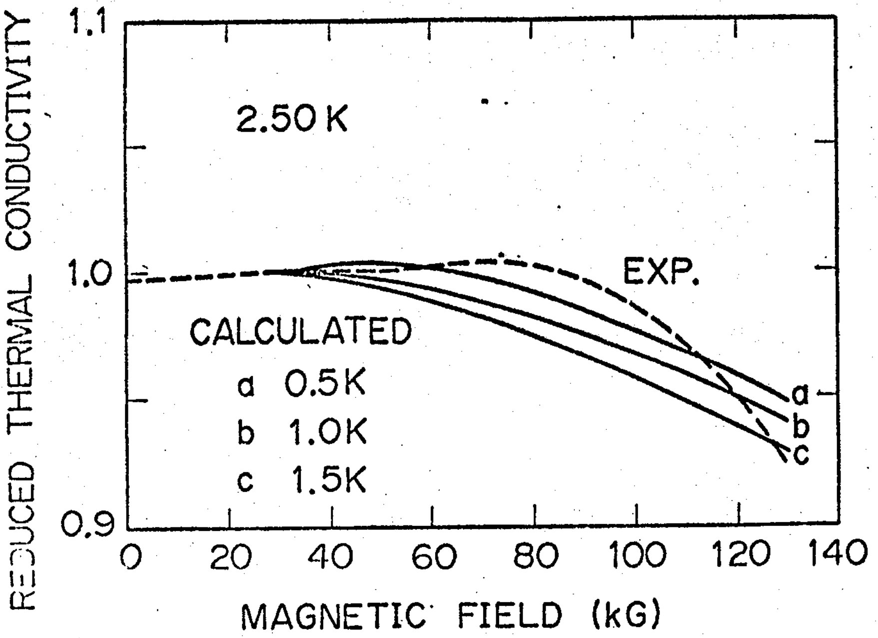

FIG. 6-3. Calculated magnetic field dependences of the thermal conductivity in p-Ge at 2.50 K under $\vec{H}$ // [001]. Solid lines denoted by a, b, and c indicate the reduced thermal conductivities under uniform splittings Δ = 0.5, 1.0, and 1.5 K, respectively. Broken line represents the data by Challis *et al.*[31] under $\vec{H}$ // [110] at 2.50 K.

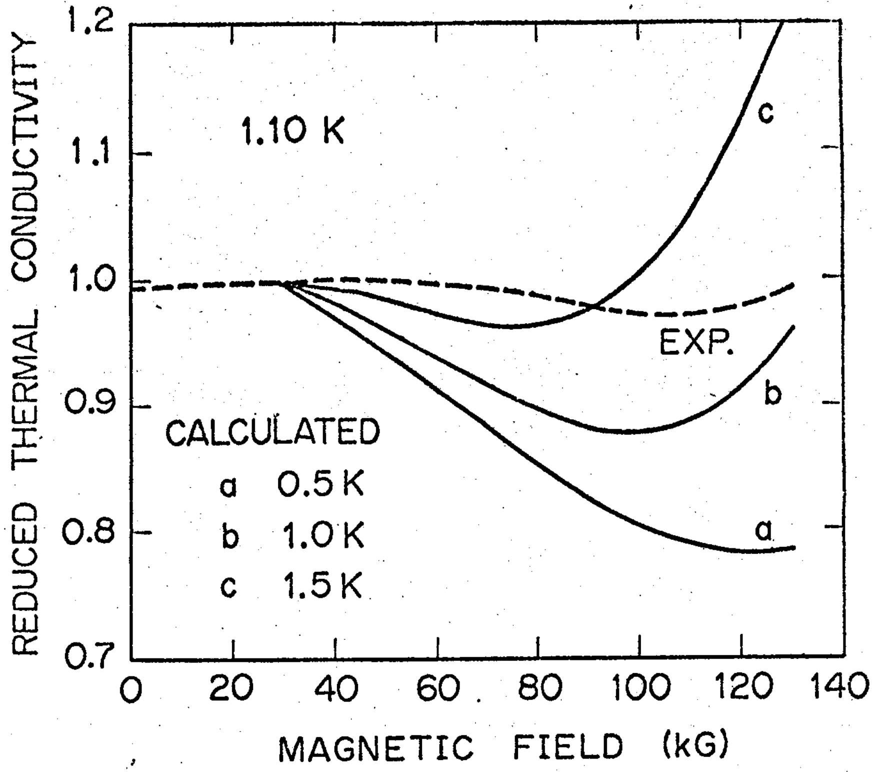

FIG. 6-2. Calculated magnetic field dependences of the thermal conductivity in p-Ge at 1.10 K under $\vec{H}$ // [001]. Solid lines denoted by a, b, and c indicate the reduced thermal conductiviti under uniform splittings Δ = 0.5, 1.0, and 1.5 K, respectively. Broken line represents the data by Challis *et al.*[31] under $\vec{H}$ // [110] at 1.14 K.

seems to us to be rather complicated.

Below 30 kG, we cannot make the quantitative discussion on the thermal conductivity as well as the ultrasonic attenuation because of the limit of the present theory. However, we can say that, in the low magnetic field, the movements of the Zeeman sublevels by applying the magnetic field are very slow as shown in Fig. 5-5 reflecting the small g-values. This may explain the fact that the change of the conductivity was slight.

VII. SUMMARY AND CONCLUDING REMARKS

We have shown that the observed MARA, as functions of the acoustic frequency, the temperature, the magnetic field direction, the acceptor concentration, the acoustic power, the acoustic mode, the propagation direction, and the uniaxial stress, are explained consistently in terms of the interaction of the ultrasonic waves with the gallium-acceptor holes in the effective mass approximation. Consequently, we could determine the Zeeman-splitting parameters. We have shown that the g-values reported by SF cannot explain the MARA. However, by re-examining the assignment of SF's data, we have shown that the g-values which are close to the present results are derived. The present g-values seems to be useful to explain the magnetothermal conductivity and to be consistent with the fact that the ESR signals have not been detected in the region corresponding to $g > 0.48$. We have shown that the quadratic Zeeman effect is appreciable in p-Ge, whose effect becomes comparable with the ordinary linear Zeeman effect near 100 kG.

From the analysis of the MARA line-shape near 100 kG, we have estimated the initial splitting of the acceptor ground-state. By using the estimated splittings, we have calculated the level widths and we have shown that the level widths become too narrow if we consider the direct and the Raman processes associated with the thermal phonons under the assumption that the impurities are isolated. The transverse relaxation via the interaction among the impurities may be an additional mechanism to the level broadening.

Finally, it is worthwhile to point out some limitations of the theory described in Sec. III, which have been noticed during the study. First, the present formulas of the ultrasonic attenuation does not take account of the local equilibrium of the acceptor holes and therefore seems to be valid except for $\omega\tau \ll 1$, where ω is the angular frequency of the phonons and τ is the relaxation time of the acceptor holes. This means that the theory is useful in the low temperature range, e.g., below 4.2 K.[68] Secondly, the present theory stands when the Zeeman splittings of the acceptor ground-state are larger than the initial splittings due to internal local stresses, i.e.,

$$|E_{14}| \text{ or } |E_{23}| > |\Delta_0|.$$

On the other hand, the present formulas for the Zeeman splittings are valid when γ is small compared with unity as described in Sec. VI-A.

In stead of the present procedure, the existence of the dynamic Jahn-Teller effect for the acceptor state in germanium has been proposed to explain the magnetothermal conductivity. We cannot rule out the posibility of the effect. However, we have explained the MARA and other phenomena in terms of the acceptor-hole-lattice interaction in the effective mass approximation.

ACKNOWLEDGMENTS

The auther wishes to express his sincere gratitude to Dr. T. Ishiguro for valuable discussion and generous support during all phases of this work. Heartful thanks are due to Professor K. Suzuki of University of Waseda and Professor N. Mikoshiba of University of Tohoku for their useful comments and discussions on the present work. It is his pleasure to express appreciation to Professor H. Kawamura of University of Osaka for his interest in this work. He is much obliged to Professor L. J. Challis of University of Nottingham for his comment by which this detailed study was motivated and for communicating his results prior to publication. He is grateful Drs. K. Kajimura and R. Inaba for their supports in the course of this work. Thanks are due to Messrs. S. Morita and K. Mitsugi for the support to supply with liquid helium.

APPENDIX A

Comparison of the resonance conditions (5.1) and (5.2) with the observations

The left-hand sides of the resonance conditions (5.1) and (5.2) are rewritten by the following parabola,

$$f_{\pm}(X,H) \equiv 2(q_2 + q_3)(H - H_0)^2 + \Delta_0 + \zeta X - 2(q_2 + q_3)H_0^2, \qquad \text{(A. 1)}$$

where

$$H_0 \equiv \mp\mu_B(g_1' + \tfrac{13}{4}g_2')/4(q_2 + q_3). \qquad \text{(A. 2)}$$

When double signs appear in the expressions, the upper and the lower signs correspond to the conditions (5.1) and (5.2), respectively. Each parabola of $f_{\pm}(X,H)$ is classified into four cases according to the coefficients as (5.5). We find that the parabolas $f_+(X,H)$ for the cases (a), (b), (c), and (d) in (5.5) have the same properties as the parabolas $f_-(X,H)$ for the cases (b), (a), (d), and (c), respectively.

First, we consider the case (b) for $f_+(X,H)$ or the case (a) for $f_-(X,H)$. The parabola in these cases is shown in Fig. A-1 schematically. When the relation $\Delta_0 - 2(q_2 + q_3)H_0^2 < -\hbar\omega$ is satisfied at $X = 0$, $|f_{\pm}(X,H)| = \hbar\omega$ gives four roots H_A, H_B, H_C, and H_D as shown in Fig. A-1, where the resonance condition is satisfied. When the uniaxial stress is applied, the parabola is raised. Then H_A, H_B, H_C, and H_D shift as shown in Fig. A-1. With further increase of X, the roots become two (H_A and H_D) and, when $X > [2(q_2 + q_3)H_0^2 - \Delta_0]/\zeta$, no roots are found.

Next, we consider the case (a) for $f_+(X,H)$ or the case (b) for $f_-(X,H)$. When we calculate H_0 according to Eq.(A.2), we find that H_0 has a negative value for these two cases. Lastly, we consider the remaining cases. Since $(q_2 + q_3)$ is negative, the roots (or the resonance fields) shift in opposite directions to ones shown in Fig. A-1.

Now let us compare the observed resonance-peak positions under $\vec{H}$ // [001] and $\vec{X}$ // [001] shown in Fig. 4-24 with the above resonance condition. The observed resonance-peak positions of the peaks A and B were shifted toward the lower magnetic fields with increasing the uniaxial stress. On the other hand, the resonance-peak positions of the peaks C and D were shifted toward the higher magnetic fields with increasing the uniaxial stress.
These peaks disappeared at H_0 = 45 kG, which is positive. This behavior is explained if we regard the resonance fields of the peaks A, B, C, and D as H_A, H_B, H_C, and H_D, respectively, in the case (b) for $f_+(X,H)$ or the case (a) for $f_-(X,H)$.

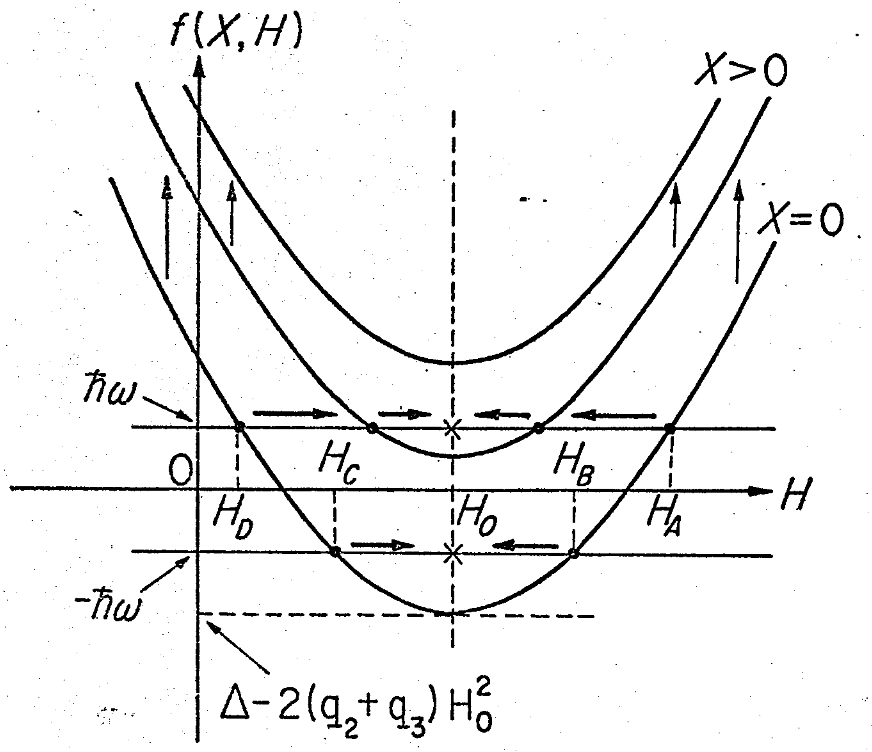

FIG. A-1. Schematic representation of the function $f(X,H)$. The vertical arrows indicate the increasing direction of the uniaxial stress $\vec{X}$, and the corresponding shifts of the resonance fields denoted by H_A, H_B, H_C, and H_D are indicated by the horizontal arrows.

APPENDIX B

Expression for the phonon relaxation-rate due to the resonance scattering by acceptor holes

The expression for the phonon relaxation-rate due to the resonance scattering is derived by using first-order perturbation theory (Golden Rule), with all higher-order terms represented by the introduction of the level broadening after Kwok.[14] Then the relaxation rate becomes[27,28]

$$\tau_R^{-1}(qt) = \frac{\pi\omega_{qt}}{\rho v_t^2}\left[1 - \exp\left(-\frac{\hbar\omega_{qt}}{kT}\right)\right]\left(\frac{2}{3}D_{u'}{}^{a}\right)^2 f^2(q) \sum_n N_n$$

$$\times \sum_{n'} \sum_{q',t'} |C_{q't'}{}^{nn'}|^2\, \delta(E_{n'n} - \hbar\omega_{qt}), \qquad \text{(B. 1)}$$

where notations used are the same in the text. At this point, the finite level widths are taken into account by simply replacing the δ-function with a Lorentzian, i.e.,[27,28]

$$\delta(E_{n'n} - \hbar\omega_{qt}) \rightarrow \frac{1}{\pi}\frac{\Gamma_n + \Gamma_{n'}}{(E_{n'n} - \hbar\omega_{qt})^2 + (\Gamma_n + \Gamma_{n'})^2}\,. \qquad \text{(B. 2)}$$

The relaxation rate is evaluated in the quasi-isotropic approximation for an axis of quantization along the [001] direction. The relaxation rate is derived for all three acoustic modes; The results are enumerated below with the index $t = 1$ denoting the longitudinal, $t = 2$ the fast-transverse, and $t = 3$ the slow-transverse phonons. From Table 3-4, the average relaxation rate,[27]

$$\bar{\tau}_R^{-1}(qt) = (1/4\pi)\iint \sin\theta\, d\theta\, d\phi\, \tau_R^{-1}(qt), \qquad \text{(B. 3)}$$

can be calculated as

$$\bar{\tau}_R^{-1}(qt) = \frac{\omega}{\rho v_t^2}\left[1 - \exp\left(-\frac{\hbar\omega}{kT}\right)\right]\left(\frac{2}{3}D_{u'}{}^{a}\right)^2 f^2(q) \times B_t, \qquad \text{(B. 4)}$$

where $\omega \equiv \omega_{qt}$ and B_t is given by, for $t = 1$,

$$\begin{aligned} B_1 = {} & N_1\Big[\frac{2}{5}\,\frac{\Gamma_1 + \Gamma_2}{(E_{21} - \hbar\omega)^2 + (\Gamma_1 + \Gamma_2)^2} + \frac{D^2 + 1}{5}\,\frac{\Gamma_1 + \Gamma_3}{(E_{31} - \hbar\omega)^2 + (\Gamma_1 + \Gamma_3)^2}\Big] \\ & + N_2\Big[\frac{2}{5}\,\frac{\Gamma_1 + \Gamma_2}{(E_{12} - \hbar\omega)^2 + (\Gamma_1 + \Gamma_2)^2} + \frac{D^2 + 1}{5}\,\frac{\Gamma_2 + \Gamma_4}{(E_{42} - \hbar\omega)^2 + (\Gamma_2 + \Gamma_4)^2}\Big] \\ & + N_3\Big[\frac{2}{5}\,\frac{\Gamma_3 + \Gamma_4}{(E_{43} - \hbar\omega)^2 + (\Gamma_3 + \Gamma_4)^2} + \frac{D^2 + 1}{5}\,\frac{\Gamma_1 + \Gamma_3}{(E_{13} - \hbar\omega)^2 + (\Gamma_1 + \Gamma_3)^2}\Big] \\ & + N_4\Big[\frac{2}{5}\,\frac{\Gamma_3 + \Gamma_4}{(E_{34} - \hbar\omega)^2 + (\Gamma_3 + \Gamma_4)^2} + \frac{D^2 + 1}{5}\,\frac{\Gamma_2 + \Gamma_4}{(E_{24} - \hbar\omega)^2 + (\Gamma_2 + \Gamma_4)^2}\Big], \end{aligned} \tag{B. 5}$$

For $t = 2$ and $t = 3$, B_2 and B_3 are obtained by the following substitutions for the numerical coefficients in the square brackets in the above expression.

$$\frac{2}{5} \rightarrow \frac{7}{20} \quad \text{and} \quad \frac{D^2 + 1}{5} \rightarrow \frac{D^2 + 1}{20} \quad \text{for } B_2 \ (t = 2); \tag{B. 6}$$

$$\frac{2}{5} \rightarrow \frac{1}{4} \quad \text{and} \quad \frac{D^2 + 1}{5} \rightarrow \frac{D^2 + 1}{4} \quad \text{for } B_3 \ (t = 3). \tag{B. 7}$$

APPENDIX C

Expression for the phonon relaxation-rate due to the second-order elastic scattering by acceptor holes

The first term in the perturbation series for the elastic scattering is of second order. It arises from two-step processes in which the acceptor holes make the transitions from the initial state to any possible intermediate states, and succeeding transitions to the final state. The expression for the phonon relaxation-rate due to these second-order elastic scattering by acceptor holes is derived by using the second Born approximation. Then the relaxation rate becomes[27,28]

$$\tau_e^{-1}(qt) = \frac{\pi\omega_{qt}}{\rho v_t^2}\left(\frac{2}{3}D_{u'}{}^{a}\right)^4 f^2(q)\sum_n N_n \sum_{n'}\sum_{q',t'}\frac{\hbar\omega_{q't'}}{2\rho v_{t'}^2} f^2(q')\,\delta(\hbar\omega_{q't'}-\hbar\omega_{qt})$$

$$\times\left|\sum_m\left(\frac{C_{q't'}^{n'm}\,C_{qt}^{mn}}{E_{mn}-\hbar\omega_{qt}}+\frac{C_{qt}^{n'm}\,C_{q't'}^{mn}}{E_{mn}+\hbar\omega_{q't'}}\right)\right|^2_{(E_n=E_{n'})},$$

(C. 1)

where n, m, and n' denote the initial, the intermediate, and the final states, respectively. Notations used are the same in the text.

For an axis of quantization along the [001] direction, the average relaxation rate in the quasi-isotropic approximation can be calculated by the same procedure as Appendix B. The result is given by

$$\bar{\tau}_e^{-1}(qt) = \frac{\omega^4}{100\pi\rho^2 v_t^2} f^2(q)\left(\frac{2}{3}D_{u'}{}^{a}\right)^4 Q(\hbar\omega)\times C_t, \qquad (C.\ 2)$$

where $Q(h\omega)$ is expressed by Eq.(3.34) and C_t is given by, for $t = 1$,

$$C_1 = N_1\left[\frac{8\{E_{21}^2+(\hbar\omega)^2\}}{\{E_{21}^2-(\hbar\omega)^2\}^2}+\frac{4\{(D^4+1)E_{31}^2+2D^2(\hbar\omega)^2\}}{\{E_{31}^2-(\hbar\omega)^2\}^2}\right]$$

$$+ N_2\left[\frac{8\{E_{12}{}^2 + (\hbar\omega)^2\}}{\{E_{12}{}^2 - (\hbar\omega)^2\}^2} + \frac{4\{(D^4 + 1)E_{42}{}^2 + 2D^2(\hbar\omega)^2\}}{\{E_{42}{}^2 - (\hbar\omega)^2\}^2}\right]$$

$$+ N_3\left[\frac{8\{E_{43}{}^2 + (\hbar\omega)^2\}}{\{E_{43}{}^2 - (\hbar\omega)^2\}^2} + \frac{4\{(D^4 + 1)E_{13}{}^2 + 2D^2(\hbar\omega)^2\}}{\{E_{13}{}^2 - (\hbar\omega)^2\}^2}\right]$$

$$+ N_4\left[\frac{8\{E_{34}{}^2 + (\hbar\omega)^2\}}{\{E_{34}{}^2 - (\hbar\omega)^2\}^2} + \frac{4\{(D^4 + 1)E_{24}{}^2 + 2D^2(\hbar\omega)^2\}}{\{E_{24}{}^2 - (\hbar\omega)^2\}^2}\right]. \qquad \text{(C. 3)}$$

For $t = 2$ and $t = 3$, C_2 and C_3 are obtained by the following substitutions for the numerical coefficients in the square brackets in the above expression.

$$8 \rightarrow 7 \text{ and } 4 \rightarrow 1 \text{ for } C_2 \ (t = 2); \qquad \text{(C. 4)}$$

$$8 \rightarrow 5 \text{ and } 4 \rightarrow 5 \text{ for } C_3 \ (t = 3). \qquad \text{(C. 5)}$$

The unphysical divergencies in these expressions can be removed by taking account of the finite level widths of the acceptor state. This just corresponds to making the substitution[27,28]

$$\{E_{nn'}{}^2 - (\hbar\omega)^2\}^{-2} \rightarrow [\{E_{nn'}{}^2 - (\hbar\omega)^2\}^2 + E_{nn'}{}^2(\Gamma_n + \Gamma_{n'})^2]^{-1}. \qquad \text{(C. 6)}$$

APPENDIX D

Expression for the phonon relaxation-rate due to the second-order inelastic scattering by acceptor holes

The inelastic scattering in the second-order perturbation falls into two categories. The first, $\tau_1^{-1}(qt)$, is associated with the hole transition from the upper level (n) to the lower level (n'). The relaxation rate for this process is readily obtained from the second Born approximation. Taking account of the direct and the inverse processes, we introduce the various statistical factors for the phonons. This inelastic process gives the relaxation rate[27,28]

$$\tau_1^{-1}(qt) = \frac{\pi\omega_{qt}}{\rho v_t^2}\left[1 - \exp\left(-\frac{\hbar\omega_{qt}}{kT}\right)\right]\left(\frac{2}{3} D_{u'}{}^{a}\right)^4 f^2(q) \sum_n N_n \sum_{n'} \sum_{q',t'} \frac{\hbar\omega_{q't'}}{2\rho v_{t'}^2} f^2(q')$$

$$\times\ (n_{q't'} + 1)\left|\sum_m\left(\frac{C_{q't'}{}^{n'm} C_{qt}{}^{mn}}{E_{mn} - \hbar\omega_{qt}} + \frac{C_{qt}{}^{n'm} C_{q't'}{}^{mn}}{E_{mn'} + \hbar\omega_{q't'}}\right)\right|^2$$

$$\times\ \delta(\hbar\omega_{q't'} - \hbar\omega_{qt} - E_{n'm}). \qquad \text{(D. 1)}$$

Another inelastic process involves the hole transition from the lower level (n) to the upper level (n') by either thermally assisted phonon absorption ($\hbar\omega_{phonon} < E_{n'n}$) or inelastic scattering ($\hbar\omega_{phonon} > E_{n'n}$). The relaxation rate for these processes is also obtained in the second Born approximation as[27,28]

$$\tau_2^{-1}(qt) = \frac{\pi\omega_{qt}}{\rho v_t^2}\left[1 - \exp\left(-\frac{\hbar\omega_{qt}}{kT}\right)\right]\left(\frac{2}{3} D_{u'}{}^{a}\right)^4 f^2(q) \sum_n N_n \sum_{n'} \sum_{q',t'} \frac{\hbar\omega_{q't'}}{2\rho v_{t'}^2} f^2(q')$$

$$\times\ \left|\sum_m\left(\frac{C_{q't'}{}^{n'm} C_{qt}{}^{mn}}{E_{mn} - \hbar\omega_{qt}} + \frac{C_{qt}{}^{n'm} C_{q't'}{}^{mn}}{E_{mn'} + \hbar\omega_{q't'}}\right)\right|^2 [\varepsilon n_{q't'}\delta(\hbar\omega_{q't'} + \hbar\omega_{qt} - E_{n'n}) +$$

$$+ (1 - \varepsilon)(n_{q't'} + 1)\delta(\hbar\omega_{q't'} - \hbar\omega_{qt} + E_{n'n})], \qquad \text{(D. 2)}$$

where ε is the step function

$$\varepsilon = \begin{cases} 1 & \text{for} \quad \hbar\omega_{qt} < E_{n'n} \\ 0 & \text{for} \quad \hbar\omega_{qt} > E_{n'n}, \end{cases} \qquad \text{(D. 3)}$$

and n_{qt} is the distribution function of the phonons

$$n_{qt} = [\exp(\hbar\omega_{qt}/kT) - 1], \qquad \text{(D. 4)}$$

and other notations are the same in the text.

For an axis of quantization along the [001] direction, the average relaxation rate in the quasi-isotropic approximation can be calculated by the same procedure as Appendix B. It should be noted that the final expressions for $\bar{\tau}_1^{-1}(qt)$ and $\bar{\tau}_2^{-1}(qt)$ are similar. They will, therefore, be written together as $\bar{\tau}_{\substack{1\\2}}^{-1}(qt)$ where the upper and the lower subscripts are associated with the upper and the lower signs or equations, respectively, when double signs or double equations appear in the expressions. Then,

$$\bar{\tau}_{\substack{1\\2}}^{-1}(qt) = \frac{\omega}{100\pi\rho^2 v_t^2} f^2(q)(\tfrac{2}{3} D_{u'}{}^{a})^4[1 - \exp(-\tfrac{\hbar\omega}{kT})] \times [D_{t1} + D_{t2} + D_{t3} + D_{t4}], \qquad \text{(D. 5)}$$

where D_{ti} $(i = 1, 2, 3, 4)$ are given as follows: for $t = 1$,

$$D_{11} = N_1[D^2(\frac{t_{12}}{\hbar})^3 n(12)Q(t_{12})\begin{pmatrix} \Theta(E_{12}) \\ \Theta(E_{21})\{1 - \delta(t_{12})\} \end{pmatrix}\{\frac{8}{t_0^{\,2}} + \frac{8}{t_{12}^{\,2}}\}$$

$$+ D^2(D^2 + 1)(\frac{t_{13}}{\hbar})^3 n(13)Q(t_{13})\begin{pmatrix} \Theta(E_{13}) \\ \Theta(E_{31})\{1 - \delta(t_{13})\} \end{pmatrix}\{\frac{4}{t_0^{\,2}} + \frac{4}{t_{13}^{\,2}}\} +$$

$$+ (D^2 + 1)\left(\frac{t_{14}}{\hbar}\right)^3 n(14)Q(t_{14})\begin{pmatrix}\Theta(E_{14})\\ \Theta(E_{41})\{1 - \delta(t_{14})\}\end{pmatrix}\times$$

$$\times \left\{2\left(\frac{1}{t_{12}} + \frac{1}{t_{34}}\right)^2 + 2\left(\frac{1}{t_{13}} + \frac{1}{t_{24}}\right)^2\right\}], \qquad (\mathrm{D.}\ 6)$$

$$D_{12} = N_2[D^2\left(\frac{t_{21}}{\hbar}\right)^3 n(21)Q(t_{21})\begin{pmatrix}\Theta(E_{21})\\ \Theta(E_{12})\{1 - \delta(t_{21})\}\end{pmatrix}\left\{\frac{8}{t_0^{\,2}} + \frac{8}{t_{21}^{\,2}}\right\}$$

$$+ (D^2 + 1)\left(\frac{t_{23}}{\hbar}\right)^3 n(23)Q(t_{23})\begin{pmatrix}\Theta(E_{23})\\ \Theta(E_{32})\{1 - \delta(t_{23})\}\end{pmatrix}\times$$

$$\times \left\{2\left(\frac{1}{t_{21}} + \frac{1}{t_{43}}\right)^2 + 2\left(\frac{1}{t_{13}} + \frac{1}{t_{24}}\right)^2\right\}$$

$$+ D^2(D^2 + 1)\left(\frac{t_{24}}{\hbar}\right)^3 n(24)Q(t_{24})\begin{pmatrix}\Theta(E_{24})\\ \Theta(E_{42})\{1 - \delta(t_{24})\}\end{pmatrix}\left\{\frac{4}{t_0^{\,2}} + \frac{4}{t_{24}^{\,2}}\right\}],$$

$$(\mathrm{D.}\ 7)$$

$$D_{13} = N_3[D^2(D^2 + 1)\left(\frac{t_{31}}{\hbar}\right)^3 n(31)Q(t_{31})\begin{pmatrix}\Theta(E_{31})\\ \Theta(E_{13})\{1 - \delta(t_{31})\}\end{pmatrix}\left\{\frac{4}{t_0^{\,2}} + \frac{4}{t_{31}^{\,2}}\right\}$$

$$+ (D^2 + 1)\left(\frac{t_{32}}{\hbar}\right)^3 n(32)Q(t_{32})\begin{pmatrix}\Theta(E_{32})\\ \Theta(E_{23})\{1 - \delta(t_{32})\}\end{pmatrix}\times$$

$$\times \left\{2\left(\frac{1}{t_{12}} + \frac{1}{t_{34}}\right)^2 + 2\left(\frac{1}{t_{31}} + \frac{1}{t_{42}}\right)^2\right\}$$

$$+ D^2\left(\frac{t_{34}}{\hbar}\right)^3 n(34)Q(t_{34})\begin{pmatrix}\Theta(E_{34})\\ \Theta(E_{43})\{1 - \delta(t_{34})\}\end{pmatrix}\left\{\frac{8}{t_0^{\,2}} + \frac{8}{t_{34}^{\,2}}\right\}], \qquad (\mathrm{D.}\ 8)$$

$$D_{14} = N_4[(D^2 + 1)(\frac{t_{41}}{\hbar})^3 n(41)Q(t_{41})\begin{pmatrix}\Theta(E_{41}) \\ \Theta(E_{14})\{1 - \delta(t_{41})\}\end{pmatrix} \times$$

$$\times \{2(\frac{1}{t_{21}} + \frac{1}{t_{43}})^2 + 2(\frac{1}{t_{31}} + \frac{1}{t_{42}})^2\}$$

$$+ D^2(D^2 + 1)(\frac{t_{42}}{\hbar})^3 n(42)Q(t_{42})\begin{pmatrix}\Theta(E_{42}) \\ \Theta(E_{24})\{1 - \delta(t_{42})\}\end{pmatrix}\{\frac{4}{t_0{}^2} + \frac{4}{t_{42}{}^2}\}$$

$$+ D^2(\frac{t_{43}}{\hbar})^3 n(43)Q(t_{43})\begin{pmatrix}\Theta(E_{43}) \\ \Theta(E_{34})\{1 - \delta(t_{43})\}\end{pmatrix}\{\frac{8}{t_0{}^2} + \frac{8}{t_{43}{}^2}\}]. \qquad \text{(D. 9)}$$

For $t = 2$, D_{2i} ($i = 1, 2, 3, 4$) are obtained by the following substitutions for the pairs of the numerical coefficients in the curly brackets in the above expressions, i.e.,

$$\begin{aligned} \{ 8 , 8 \} &\rightarrow \{ 12 , 7 \}, \\ \{ 4 , 4 \} &\rightarrow \{ 6 , 1 \}, \qquad \text{(D. 10)} \\ \{ 2 , 2 \} &\rightarrow \{ \tfrac{7}{4} , \tfrac{1}{2} \}. \end{aligned}$$

For $t = 3$, D_{3i} ($i = 1, 2, 3, 4$) are also obtained by the similar substitutions, i.e.,

$$\begin{aligned} \{ 8 , 8 \} &\rightarrow \{ 0 , 5 \}, \\ \{ 4 , 4 \} &\rightarrow \{ 0 , 5 \}, \qquad \text{(D. 11)} \\ \{ 2 , 2 \} &\rightarrow \{ \tfrac{5}{4} , \tfrac{5}{2} \}. \end{aligned}$$

In these expressions,

$$t_0 = \hbar\omega, \qquad \text{(D. 12)}$$

$$t_{ij} = E_{ij} + \hbar\omega, \qquad \text{(D. 13)}$$

$$n(ij) = [1 - \exp(-\frac{t_{ij}}{kT})]^{-1}, \qquad \text{(D. 14)}$$

$$\Theta(E) = \begin{cases} 1 & \text{for } E > 0 \\ 0 & \text{for } E \leq 0, \end{cases} \qquad \text{(D. 15)}$$

and $\delta(E)$ is the delta function and $Q(E)$ is defined by Eq.(3.34).

REGERENCES

1 R. W. Keyes, Phys. Rev. 122, 1171 (1961).

2 A. Griffin and P. Carruthers, Phys. Rev. 131, 1976 (1963).

3 J. Goff and N. Pearlman, Phys. Rev. 140, A2151 (1965); M. P. Mathur and N. Pearlman, Phys. Rev. 180, 833 (1969).

4 K. Suzuki and N. Mikoshiba, J. Phys. Soc. Japan 31, 186 (1971).

5 J. A. Carruthers, T. H. Geballe, H. M. Rosenberg, and J. M. Ziman, Proc. Roy. Soc. (London) A238, 502 (1957); J. A. Carruthers, J. F. Cochran, and K. Mendelssohn, Cryogenics 2, 160 (1962).

6 L. J. Challis, J. D. N. Cheeke, and D. J. Williams, in *Proceedings of the International Conference on the Low Temperature Physics, Columbus, 1965*, p. 1145; L. J. Challis, J. D. N. Cheeke, and J. B. Harness, Phil. Mag. 7, 1941 (1962).

7 A. M. Poujade and H. J. Albany, Phys. Rev. 182, 802 (1969).

8 J. C. Thompson and B. A. Younglove, J. Phys. Chem. Solids 20, 146 (1961).

9 M. G. Holland and L. S. Neuringer, in *Proceedings of the International Conference on the Physics of the Semiconductors, Exeter, 1962*, p. 474; M. G. Holland, in *Semiconductors and Semimetals*, edited by R. K. Willardson and A. C. Beer (Academic Press, New York, 1966), Vol. 2, p. 3.

10 K. Suzuki and N. Mikoshiba, in *Proceedings of the International Conference on Phonon Scattering in Solids, Paris, 1972* (Commissariat a l'Energie Atomique Service de Documentation, Saclay, 1972), p. 125.

11 R. W. Keyes, IBM J. Res. Dev. 5, 266 (1961); in *Solid State Physics*, edited by F. Seitz and D. Turnbull (Academic Press, New York, 1967), Vol. 20, p. 37.

12 M. Pomerantz, Proc. IEEE 53, 1438 (1965); Phys. Rev. B1, 4029 (1970).

13 K. Suzuki and N. Mikoshiba, Phys. Lett. 23, 44 (1966); J. Phys. Soc. Japan 28, 1248 (1970).

14 P. C. Kwok, Phys. Rev. 149, 666 (1966).

15 T. Ishiguro and N. Mikoshiba, J. Phys. Chem. Solids 31, 1729 (1970).

16 T. Miyasato, F. Akao, and M. Ishiguro, J. Phys. Soc. Japan 35, 1668 (1973).

17 W. P. Mason and T. Bateman, Phys. Rev. 134, A1386 (1964).

18 M. Pomerantz, in *Proceedings of the Symposium on Acoustoelectronics, Sendai, 1968* (unpublished), p. 39.

19 K. Suzuki and N. Mikoshiba, Phys. Rev. Lett. 28, 94 (1972).

20 H. Hasegawa, Phys. Rev. 129, 1029 (1963).

21 K. Suzuki, M. Okazaki, and H. Hasegawa, J. Phys. Soc. Japan 19, 930 (1964).

22 W. Kohn, in *Solid State Physics*, edited by F. Seitz and D. Turnbull (Academic Press, New York, 1957), Vol. 5, p. 257.

23 T. Ishiguro and H. Tokumoto, J. Phys. Soc. Japan 37, 1716 (1974).

24 T. Ishiguro, Phys. Rev. B8, 629 (1973).

25 T. Ishiguro, T. A. Fjeldly, and C. Elbaum, Solid State Commun. 10, 1309 (1972).

26 T. Ishiguro and S. Waki, Phys. Lett. A39, 85 (1972); T. Ishiguro, K. Suzuki, and N. Mikoshiba, in *Proceedings of the International Conference on the Physics of Semiconductors, Warsaw, 1972* (PWN-polish Scientific Publishers, Warsaw, 1972), p. 1239.

27 K. Suzuki and N. Mikoshiba, Phys. Rev. B3, 2550 (1971); J. Phys. Soc. Japan 31, 44 (1971).

28 T. Fjeldly, T. Ishiguro, and C. Elbaum, Phys. Rev. B7, 1392 (1973); T. Ishiguro, T. A. Fjeldly, and C. Elbaum, Phys. Rev. Lett. 27, 667 (1971).

29 L. J. Challis and L. Halbo, Phys. Rev. Lett. 28, 816 (1972); L. Halbo and L. J. Challis, in *Proceedings of the International Conference on Phonon Scattering in Solids, Paris, 1972* (Commissariat a l'Energie Atomique Service de Documentation, Saclay, 1972), p. 139.

30 T. N. Morgan, Phys. Rev. Lett. 24, 887 (1970).

31 L. J. Challis, S. C. Haseler, M. W. S. Parsons, and J. Rivallin, in *Phonon Scattering in Solids*, edited by L. J. Challis, V. W. Rampton, and A. F. G. Wyatt (Plenum Press, New York and London, 1976), p. 328.

32 H. Tokumoto, T. Ishiguro, R. Inaba, K. Kajimura, K. Suzuki, and N. Mikoshiba, Phys. Rev. Lett. 32, 717 (1974).

33 H. Tokumoto and T. Ishiguro, Bussei 8, 17 (1974) (in Japanese).

34 H. P. Sopangkat and P. Fisher, Phys. Rev. B8, 870 (1973).

35 R. Inaba, T. Ishiguro, and N. Mikoshiba, Japan J. Appl. Phys. 10, 1493 (1971).

36 F. H. Pollak, Phys. Rev. 138, A618 (1965).

37 K. Kajimura, S. Morita, and K. Mitsugi, in *Bulletin of the Electrotechnical Laboratory*, 39, 69 (1975).

38 G. K. White, *Experimental Techniques in Low-Temperature Physics* (Oxford University Press, 1968), 2nd edition, p. 167.

39 K. S. Mendelson and D. R. Schultz, Phys. Status Solidi 31, 59 (1969).

40 K. S. Mendelson and H. M. James, J. Phys. Chem. Solids 25, 729 (1964).

41 W. Kohn and D. Schechter, Phys. Rev. 99, 1903 (1955); D. Schechter, J. Phys. Chem. Solids 23, 237 (1962).

42 G. L. Bir, E. I. Butikov, and G. E. Pikus, J. Phys. Chem. Solids 24, 1467 (1963).

43 P. J. Lin-Chung and R. F. Wallis, J. Phys. Chem. Solids 30, 1453 (1969).

44 A. K. Bhattacharjee and S. Rodriguez, Phys. Rev. B6, 3836 (1972).

45 for example, L. I. Schiff, *Quantum Mechanics* (McGraw-Hill, New York, 1955), 2nd edition, p. 292.

46 J. M. Luttinger and W. Kohn, Phys. Rev. 97, 869 (1955); W. H. Kleiner and L. M. Roth, Phys. Rev. Lett. 2, 334 (1959); J. M. Luttinger, Phys. Rev. 102, 1030 (1956).

47 J. C. Hensel and G. Feher, Phys. Rev. 129, 1041 (1963).

48 H. Hasegawa, Phys. Rev. 118, 1523 (1960).

49 F. I. Fedrov, *Theory of Elastic Waves in Crystals* (Plenum Press, New York, 1968).

50 L. M. Roth, Phys. Rev. 118, 67 (1960).

51 E. Ortlieb, Hp. Schad, and K. Lassmann, Solid State Commun. 19, 599 (1976).

52 T. Ishiguro and H. Tokumoto, in *Phonon Scattering in Solids*, edited by L. J. Challis, V. W. Rampton, and A. F. G. Wyatt (Plenum Press, New York and London, 1976), p. 323.

53 J. C. Hensel and K. Suzuki, Phys. Rev. B9, 4219 (1974).

54 We take the average values for D_u and $D_{u'}$ from Table III in Ref. 28, since the concentration of our samples are in the midst of the samples in Ref. 28.

55 One of the static deformation-potential constants, $D_{u'}^{a}$, is almost the same as one determined by the heat-pulse experiment in Ref. 28. The values of the deformation-potential constants from the other experiments are tabulated in Table II in Ref. 53.

56 C. P. Slichter, *Principles of Magnetic Resonance* (Harper and Row Publishers, New York, 1963), p. 4.

57 J. Joffrin and A. Levelut, J. de Phys. 36, 811 (1975) and references therein.

58 Y. Yafet, R. W. Keyes, and E. N. Adams, J. Phys. Chem. Solids 1, 137 (1956).

59 R. L. Jones and P. Fisher, J. Phys. Chem. Solids 26, 1125 (1965).

60 P. Csavinsky, Phys. Rev. 119, 1605 (1960).

61 T. Mitsuma and K. Morigaki, private communication. We thank to Professor K. Morigaki for helpful conversation.

62 N. Mikoshiba and S. Gonda, Phys. Rev. 127, 1954 (1962).

63 E. Sonder and H. C. Schweinler, Phys. Rev. 117, 1216 (1960).

64 H. G. Van Bueuren, *Imperfections in Crystals* (North-Holland, Amsterdam, 1960), p. 31 and p. 599.

65 A. M. Stoneham, Rev. Mod. Phys. 41, 82 (1969).

66 W. T. Read, *Dislocations in Crystals* (McGraw-Hill, New York, 1953), p. 114.

67 G. L. Bir, Sov. Phys. JETP 24, 372 (1967).

68 K. Suzuki, private communication.